
Electronic Thesis and Dissertation Repository

7-27-2022 2:00 PM

Quantitative MRI and 3D-Printing for Monitoring Periprosthetic Joint Infection

Greg Hong, *The University of Western Ontario*

Supervisor: Drangova, Maria, *The University of Western Ontario*

Joint Supervisor: Holdsworth, David W., *The University of Western Ontario*

A thesis submitted in partial fulfillment of the requirements for the Doctor of Philosophy degree in Medical Biophysics

© Greg Hong 2022

Follow this and additional works at: <https://ir.lib.uwo.ca/etd>



Part of the [Medical Biophysics Commons](#), [Orthopedics Commons](#), and the [Radiology Commons](#)

Recommended Citation

Hong, Greg, "Quantitative MRI and 3D-Printing for Monitoring Periprosthetic Joint Infection" (2022). *Electronic Thesis and Dissertation Repository*. 8712.
<https://ir.lib.uwo.ca/etd/8712>

This Dissertation/Thesis is brought to you for free and open access by Scholarship@Western. It has been accepted for inclusion in Electronic Thesis and Dissertation Repository by an authorized administrator of Scholarship@Western. For more information, please contact wlsadmin@uwo.ca.

Abstract

Joint replacements are becoming increasingly commonplace with over 130,000 joint arthroplasties being performed annually in Canada. Although joint replacement surgery is highly successful, implants do occasionally fail and need to be replaced via costly and difficult revision surgery. Periprosthetic joint infection (PJI) has recently become the leading reason for revision of both hip and knee replacements, which is unfortunate because PJI is difficult to diagnose and treat effectively; diagnosis is made particularly difficult by the lack of established non-invasive (imaging) means of evaluating PJI. This thesis aims to demonstrate that magnetic resonance imaging (MRI) has potential for diagnosing and monitoring PJI through advances in implant design and novel application of quantitative imaging.

The recent proliferation of metal 3D-printing has already inspired the clinical use of 3D-printed porous metal devices due to their favorable osseointegration and mechanical properties. This thesis explores an important MRI benefit to porous implants: their decreased effective magnetic susceptibility and proportional decrease in imaging artifacts. This is relevant to PJI because MRI is already well-established in diagnosing musculoskeletal infections, but metals cause image obscuring signal loss. This work shows that 3D-printed porous metal structures are likely to avoid this limitation, as their effective magnetic susceptibility is linearly proportional to porosity; if true, MRI will be able to diagnose PJI as easily as non-prosthetic joint infections.

This thesis describes a novel use for two important parameters measured by quantitative MRI: effective relaxation rate ($R2^*$) and magnetic susceptibility (QSM; quantitative susceptibility mapping). This work seeks to address an important unmet need in PJI treatment – the ability to monitor drug release during localized antibiotic delivery – by exploiting these parameters' proportionality to gadolinium concentration. This idea is centered around using gadolinium-based MRI contrast agents as a surrogate small-molecule that acts as a proxy for drugs to study diffusion-controlled release. An initial implementation of this concept showed promising results, including the ability to fit the data to a mathematical model of drug

release. This shows the potential of MRI as a non-invasive means of monitoring localized antibiotic treatment of PJI post-revision.

Keywords

Periprosthetic joint infection, Magnetic resonance imaging, Quantitative susceptibility mapping, Metal artifacts, 3D-printed porous implants, Geometric distortion phantoms.

Summary for Lay Audience

Joint replacements are becoming increasingly commonplace with over 130,000 joint arthroplasties being performed annually in Canada. Although joint replacement surgery is highly successful, implants do occasionally fail and need to be replaced via costly and difficult revision surgery. Unfortunately, the top reason for implant failure is now periprosthetic joint infection (PJI), which is a devastating form of infection that is attached to the implanted joint. PJI is difficult to treat systemically and usually requires targeted drug delivery to eradicate. Furthermore, imaging-based diagnosis of PJI remains outside of standard practice as many types of imaging perform poorly around metal. The ability to use magnetic resonance imaging (MRI) is a particularly unfortunate loss, as it is well-established that MRI is highly useful for looking at musculoskeletal infection (without implants) and has many technical advances that remain unused in orthopedics. These capabilities motivate the objective of this thesis: to demonstrate that MRI has potential for diagnosing and monitoring PJI through both advances in implant design and novel application of quantitative imaging.

One of the most exciting recent advances in orthopedics is the adoption of metal 3D-printing, which has led to a variety of porous implants that are proving to be highly compatible with bone. In this thesis, I demonstrate that these porous implants have an unexplored benefit: they drastically improve MRI image quality relative to solid metal, particularly at higher porosities, which should enable MRI-based diagnosis of PJI in a manner similar to other musculoskeletal infections.

Quantitative MRI techniques, which provide measurements of tissue properties instead of just signal, remain largely unused in orthopedic imaging. Here I describe a novel use for the fact that some of these measurements are directly proportional to contrast agent

concentration, which are routinely used for signal enhancement: tracking antibiotic release from localized drug delivery systems by using a contrast agent as a proxy. As there is currently no way to measure antibiotic release during PJI treatment, this could be an impactful clinical tool.

Co-Authorship Statement

This thesis is presented in an integrated article format, of which the experimental chapters are based on the following publications:

Chapter 2: Greg Hong, Matthew G. Teeter, Jaques S. Milner, Steven I. Pollmann, Maria Drangova, and David W. Holdsworth – Centroid-Based Analysis of Customizable 3D-Printed MRI Distortion Phantoms (In preparation for submission)

My contribution to this work includes phantom preparation, MR imaging and data collection, all aspects (conception, design, fabrication, data acquisition, and analysis) pertaining to the custom insert phantom, field mapping, and manuscript preparation. Study conception and design is credited to Dr. David W. Holdsworth along with phantom fabrication, design, and analysis algorithm (US patent 10557911). Jaques S. Milner coded the automated analysis software. Drs. Maria Drangova and David Holdsworth contributed to data analysis and manuscript preparation.

Chapter 3: Greg Hong, Junmin Liu, Santiago F. Cobos, Tina Khazaei, Maria Drangova, David W. Holdsworth – Effective Magnetic Susceptibility of 3D-Printed Porous Metal Scaffolds (Published: *Magnetic Resonance in Medicine* 2022; DOI: 10.1002/mrm.29136)

My contribution to this work includes study conception and design, phantom design, fabrication and preparation, MR imaging and data collection, generating simulated field maps, co-registration between simulated and scanned images, data analysis, and manuscript preparation. Dr. Santiago F. Cobos and Tina Khazaei conceived the use of sheet-gyroid unit cells for porous metal implants and assisted in designing the porous scaffolds in this study. Tom Chmiel was responsible for fabricating the porous metal cylinders. Drs. Junmin Liu, Maria Drangova and David W. Holdsworth contributed to data analysis and manuscript preparation.

Chapter 4: Greg Hong, Tina Khazaei, Junmin Liu, Spencer D. Christiansen, Santiago F. Cobos, Maria Drangova, and David W. Holdsworth – Characterizing Diffusion-Controlled Release of Small-Molecules Using Quantitative MRI: Application to Orthopedic Infection (In preparation for submission)

My contribution to this work includes phantom design, fabrication and preparation, sample preparation, MR imaging and data collection, generating simulated field maps, co-registration between simulated and scanned images, data analysis, and manuscript preparation. Study conception and design was adapted for MRI from Tina Khazae's work in CT. Dr. Spencer D. Christiansen assisted in adapting the MRI sequence and data processing created by Dr. Junmin Liu for this project. Dr. Santiago F Cobos and Tina Khazae conceived the use of sheet-gyroid unit cells for porous metal scaffolds. Tom Chmiel was responsible for fabricating the porous metal scaffold. Drs. Junmin Liu, Maria Drangova and David W. Holdsworth contributed to data analysis and manuscript preparation.

Table of Contents

Abstract	ii
Summary for Lay Audience	iii
Co-Authorship Statement.....	v
Table of Contents	vii
List of Tables	xii
List of Figures	xiii
List of Appendices (where applicable)	xix
List of Abbreviations, Symbols, Nomenclature.....	xx
Chapter 1	1
1 General Introduction	1
1.1 Clinical Motivation	1
1.1.1 Background.....	1
1.1.2 Diagnosis of PJI	1
1.1.3 Revision Procedure	2
1.1.4 Antibiotic Carriers	3
1.2 Imaging of PJI.....	5
1.2.1 Radiography and Computed Tomography	5
1.2.2 Nuclear Medicine.....	6
1.2.3 Magnetic Resonance Imaging.....	6
1.3 MRI Metal Artifacts.....	7
1.3.1 Susceptibility Artifacts.....	7
1.3.2 Artifact Reduction in MRI	10
1.3.3 Field Map Simulation	12
1.4 Quantitative Imaging	12

1.4.1	Transverse Relaxation Rate ($R2^*$)	13
1.4.2	Quantitative Susceptibility Mapping	14
1.5	3D-printed orthopedic implants	14
1.5.1	Overview of 3D-printing techniques	15
1.5.2	Existing orthopedic applications of 3D-printing.....	16
1.5.3	Relevance for PJI	16
1.6	Thesis objectives.....	17
1.7	References.....	20
Chapter 2	27
2	Centroid-Based Analysis of Customizable 3D-Printed MRI Distortion Phantoms	27
2.1	Introduction.....	27
2.2	Materials & Methods	30
2.2.1	Concept	30
2.2.2	Design and 3D-Printing	31
2.2.3	Automated Analysis Software	33
2.2.4	Fabrication Accuracy	34
2.2.5	Imaging	34
2.2.6	Custom Insert Phantom.....	35
2.2.7	Statistical Analysis.....	37
2.3	Results.....	37
2.3.1	Fabrication Accuracy	37
2.3.2	Automated Distortion Analysis.....	39
2.3.3	Susceptibility-Induced Distortion	42
2.4	Discussion.....	45
2.5	References.....	50
Chapter 3	54

3	Effective Magnetic Susceptibility of 3D-Printed Porous Metal Scaffolds	54
3.1	Introduction.....	54
3.2	Methods.....	55
3.2.1	Gyroid-Based Porous Metal Scaffold Samples.....	55
3.2.2	Alignment Phantom	57
3.2.3	Imaging	58
3.2.4	Bead identification and Volume of Interest (VOI)	58
3.2.5	Estimation of Signal Void Volume.....	58
3.2.6	Estimation of Effective Magnetic Susceptibility	59
3.2.7	Analysis.....	62
3.3	Results.....	62
3.3.1	Gyroid-Based Porous Metal Scaffolds.....	62
3.3.2	Phantom Alignment	63
3.3.3	Signal-void Volume	64
3.3.4	Effective Susceptibility.....	65
3.3.5	Simulation of Porous Geometry.....	67
3.4	Discussion and Conclusion.....	68
3.4.1	Effective Susceptibility.....	69
3.4.2	Signal-void Volume	69
3.4.3	Limitations	70
3.4.4	Conclusions.....	71
3.5	References.....	72
	Chapter 4.....	75
4	Characterizing Diffusion-Controlled Release of Small-Molecules Using Quantitative MRI: Application to Orthopedic Infection.....	75
4.1	Introduction.....	75

4.2	Methods.....	77
4.2.1	Experimental Setup.....	77
4.2.2	Sample Preparation.....	78
4.2.3	Phantom Design.....	79
4.2.4	Gyroid-Based Porous Metal Core.....	81
4.2.5	Imaging.....	82
4.2.6	Quantitative Mapping.....	83
4.2.7	Phantom Co-Registration.....	83
4.2.8	Data Analysis.....	84
4.3	Results.....	87
4.3.1	Images of the Calcium Sulfate Core.....	87
4.3.2	Images of Calcium Sulfate in a Porous Metal Scaffold.....	90
4.3.3	Relationship Between Concentration, Magnitude, $R2^*$ and QSM.....	93
4.3.4	Total Release and Diffusion Coefficient.....	93
4.4	Discussion.....	95
4.4.1	Calcium Sulfate Core.....	96
4.4.2	Calcium Sulfate Contained in a Porous Metal Scaffold.....	97
4.4.3	Limitations.....	98
4.4.4	Conclusions.....	98
4.5	References.....	99
	Chapter 5.....	103
5	Conclusions and Future Directions.....	103
5.1	Summary and Conclusions.....	103
5.2	Limitations.....	105
5.2.1	Centroid-Based Analysis of Geometric Distortion.....	105
5.2.2	Effective Susceptibility of Porous Metal Scaffolds.....	106

5.2.3	Characterizing Diffusion-Controlled Release with MRI	106
5.3	Future Work	106
5.3.1	Quantitative MRI of Antibiotic-Loaded Calcium Sulfate Beads.....	107
5.3.2	Geometric Distortion Surrounding Porous Titanium Implants.....	108
5.3.3	MR Thermometry of Gyroid-Based Porous Metal Scaffolds.....	109
5.4	References.....	110
	Curriculum Vitae	116

List of Tables

Table 2.1: Measurements of phantom fabrication accuracy from measuring microscope and automated analysis of CT images	39
Table 3.1: Calculation of the actual porosities based on measured vs. expected mass	63
Table 3.2: Measured rotations (degrees) and translations (mm) based on alignment phantom. Rotations are used to find orientation of cylinder to B0 to generate simulations; translations are used to create matching VOIs between scan and simulation for analysis.	63
Table 3.3: Average absolute frequency difference (Hz) in Figure 3-5C. The values represent the volume average of a 10 mm long cylindrical shell centered on the simulated cylinder with inner and outer diameter matching the reported distance to cylinder wall.	67

List of Figures

Figure 1.1: First stage of a two-stage revision. A. Preoperative radiograph of the left knee. B. The prefabricated articulated knee antibiotic-loaded cement (poly methyl methacrylate) spacer will be implanted after removal of the infected prostheses and extensive debridement and irrigation of the joint space. C. Intraoperative photograph after implantation of the spacer. D. Anteroposterior radiograph of the left knee after spacer implantation. Figure reproduced from Samelis et al. ¹⁷ under the terms of the Creative Commons Attribution License CC-BY 4.0.	3
Figure 1.2: Two-stage revision for PJI after total replacement of the right hip using a prefabricated spacer. Breakage (yellow arrow) and dislocation (blue arrow) of the spacer out of the acetabulum (asterisk). Figure reproduced from Samelis et al. ¹⁷ under the terms of the Creative Commons Attribution License CC-BY 4.0.	4
Figure 1.3: Simulated field maps surrounding a cylinder of varying magnetic susceptibility representing materials relevant to this thesis. Negative susceptibilities are diamagnetic and positive susceptibilities are paramagnetic.	8
Figure 1.5: Magnitude image and corresponding simulated field map of a titanium cylinder, used to demonstrate various sources of signal loss and artifacts. A) Magnitude and frequency shifts through the center of the cylinder, showing signal loss from unexcited protons and signal pileup. B) Magnitude and frequency shift 10 mm off-center, showing a region without metal but still affected by signal loss where there are steep field gradients.	10
Figure 1.6: Schematic illustration of the different printing techniques. Left: fused deposition modeling; Center: 3D inkjet; Right: selective laser sintering/selective laser melting. Figure adapted and modified from Domsta & Seidlitz ⁵⁵ under the terms of the Creative Commons Attribution License CC-BY 4.0.	15
Figure 2.1: Renderings of the phantom design. A) 4.5 mm diameter spherical marker attached to 1.5 mm diameter strut-based supports. B) Strut-based phantom composed of 5x5x10 markers. C) 4.5 mm diameter spherical marker attached to 0.8 mm thick wall-based supports. D) Wall-based phantom cut to cylindrical profile (580 markers).	32

Figure 2.2: Strut- and wall-based phantoms submerged in CuSO₄ saline solution within 11.4 cm diameter cylinder. Strut-based phantom is centered with a 3D-printed PLA holder. 33

Figure 2.3: Custom insert phantom holding a hip implant. A) Custom press-fit clips that link the three modules together. B) Photo of the modules and hip implant prior to assembly. C) Assembled phantom submerged in CuSO₄ saline solution within 11.4 cm diameter cylinder 36

Figure 2.4: Marker deviations in CT. The strut-based phantom markers have a mean deviation magnitude of 0.122 ± 0.08 mm and the wall-based phantom have a mean deviation magnitude of 0.130 ± 0.06 mm. 38

Figure 2.5: MRI compatibility analysis through field shift mapping. A) Marker beads chosen from strut-based phantom. Yellow: detected marker centroids overlaid on slice. B) Marker beads chosen from wall-based phantom. C) Line profiles centered on detected marker centroids; lines are diagonal and in the axial plane to avoid crossing supporting structures. Only 5 of the 20 beads used in averaging from each phantom is shown. D) Average frequency shift surrounding marker beads in the strut-based phantom; the three central voxels are within the marker, thus having low signal and noisy phase measurements. E) Average frequency shift surrounding marker beads in the wall-based phantom. 40

Figure 2.6: 3D magnitude images analyzed for MR image distortion..... 41

Figure 2.7: Marker deviations in MRI at isocenter and 10 cm off-center. Both phantoms are cropped to a matching set of 5x5x8 marker beads. Warping from the holder contribute to the abnormal deviations in the central column of the strut-based deviation maps. 42

Figure 2.8: Large image distortions in axial 2D fast spin echo images surrounding a hip implant. Slices are 3 mm thick with 3.5 mm spacing; through-plane distortions are observed through the presence or absence of markers and in-plane distortion is evident by irregular spacing of markers. 44

Figure 2.9: Quantitative analysis of susceptibility induced distortion in a 3D acquisition surrounding a titanium hip stem. A) Detected marker beads; spherical markers are differentiated from other signal voids based on size and roundness. B) Deviation map from

detected marker beads; white ball shows expected location and red ball indicates location in image..... 45

Figure 3.1: Gyroid-based scaffold and alignment phantom design. (A) Example of a gyroid surface unit cell and cylinder model. (B) Renderings of the set of cylindrical samples of varying nominal porosity (%) generated by varying wall thickness (C) Marker bead and supporting wall structure. (D) Rendering of the alignment phantom, cut to demonstrate the position of a 3D-printed cylinder within the custom holder (red). A grid of uniformly spaced marker beads is incorporated to enable reproducible alignment of acquired images to simulated field maps. The transparent grey box identifies the volume of interest used in the study. (E) Rendering of the whole phantom 57

Figure 3.2: Histogram (bin width = 50, range = 0 to 1800) used to determine the binary threshold (271) used for signal void analysis. As the voxel intensities exhibit a multimodal distribution, the full histogram was truncated at 650 (as this cut-off value maximizes the effectiveness metric of the resulting threshold) prior to using Otsu’s method. 59

Figure 3.3: Flowchart used to estimate the effective susceptibility of the porous metal samples..... 61

Figure 3.4: Magnitude images of central coronal slices. Axial images (sliced at LC and LE) show artifact size at the center of the cylinder (LC) and through the bottom edge (LE). Observed hyperintensity artifact is shown by ★. Bisected marker beads used for creating the VOI are visible in the axial center slices; grid intersections (spaced 13 mm apart) provide structural support and can be used as geometric landmarks. 64

Figure 3.5: (A) Signal void volume, determined from the first echo 3D magnitude images, as a function of measured porosity. Data and quadratic fit are plotted; the extrapolated 100% porosity value is 9511 mm³, which compares well with the physical cylinder volume (9080 mm³). (B) Linear relationship between effective susceptibility estimates and porosity (slope = -1.846 ppm/% porosity, Y-intercept = 174.7 ppm). Extrapolated susceptibility at 100% porosity (no metal) is -9.9 ppm (expected: -9 ppm) and estimated susceptibility of solid cylinder is 174 ppm (expected: 176 ppm)..... 65

Figure 3.6: (A) Central coronal slice of the measured field maps of each porous cylinder. (B) Derivation of the effective susceptibility estimate from the 80% porosity cylinder using a central 65 mm line profile from the scanned field map compared to matching line profiles from simulations of solid cylinders of varying susceptibility. (C) Central line profiles of all measured (scanned) field maps (solid) and their matching simulation (dashed) determined by minimizing root mean square error. 66

Figure 3.7 : (A) Field map simulations of homogeneous cylinders assigned porosity-dependent effective susceptibility (B) Simulated field maps of the gyroid-based porous cylinders, using the 3D geometry used for 3D-printing (0.1 mm³ resolution, 174 ppm susceptibility). (C) Difference map comparing (A) and (B); difference maps are magnified to emphasize differences near the cylinder wall. The coronal and axial maps are from the corresponding central planes. Small inhomogeneities adjacent to the walls of the scaffold (mostly contained within 2 mm of the perimeter of the cylinder) are the likely source of signal loss seen in the scanned axial magnitude images. 68

Figure 4.1: A) Silicone mold made from 3D-printed PLA negatives B) Enclosures to hold central core (top: blocked diffusion, bottom: free diffusion) C) Assembled sample (top: core surrounded by agar, bottom: core placed into inset prior to pouring agar)..... 78

Figure 4.2: A) Configuration of calibration vials and spherical markers used in registration B) Assembled phantom with calibration vials set in agar..... 80

Figure 4.3: A) Sheet-based gyroid unit cell B) Array of unit cells with 0.2 mm wall thickness truncated into cylinder D) Titanium 3D-printed scaffold filled with calcium sulfate 82

Figure 4.4: Time-series of magnitude, R2* and QSM images at time points ranging from 3 hours to 4 weeks. Slice shown is the plane of radial symmetry that bisects all three spherical markers. A) Magnitude images of calcium sulfate (Stimulan) loaded with gadolinium contrast agent (Gadovist) B) R2* images calculated from signal decay over 10 echoes. C) QSM map showing the core susceptibility decreasing as gadolinium is released 88

Figure 4.5: Radially averaged line profiles. Each data point averages 600 total samples, spanning 5 slices of 120 points spaced 3 degrees apart. Standard deviations (dotted lines of matching colors) are calculated for each point as a measure of the data's reliability. A)

Average intensity of magnitude images (B) R2* line profiles. The lack of signal within the core resulted in a noisy fitting and was thus discarded. C) QSM line profiles. While the concentration of gadolinium is not detectable within the agar, QSM is sensitive to the change in susceptibility of the core as gadolinium is released..... 89

Figure 4.6: Time-series of magnitude, R2* and QSM images at time points ranging from 3 hours to 4 weeks of gadolinium-loaded calcium sulfate in a porous metal scaffold. Slice shown is the plane of radial symmetry that bisects all three spherical markers. A) Magnitude images of calcium sulfate (Stimulan) loaded with gadolinium contrast agent (Gadovist) in a 3D-printed titanium-alloy porous scaffold B) R2* images calculated from signal decay over 10 echoes. R2* values near the core are heavily affected by field inhomogeneity. C) QSM map showing the core susceptibility decreasing as gadolinium is released. The higher susceptibility metal scaffold results in poor susceptibility estimates. 91

Figure 4.7: Radially averaged line profiles when a metal scaffold is added to the core. Each data point averages 600 total samples, spanning 5 slices of 120 points spaced 3 degrees apart. Standard deviations (dotted lines of matching colors) are calculated for each point as a measure of the data's reliability. A) Average intensity of magnitude images (B) R2* line profiles. The lack of signal within the core resulted in a noisy fitting and was thus discarded. C) QSM line profiles. The addition of metal to the calcium sulfate core increased susceptibility as expected but resulted in poor overall data quality. Notably, the week 2 QSM image had artifacts that are reflected by a high standard deviation 92

Figure 4.8: Volume average of 3 slices of each calibration vial (8 mm ROI). A) Magnitude; no correlation. B) R2*; linear fit: water vials R2 = 0.956, slope = 125 s-1/M; agar vials R2 = 0.995, slope = 148 s-1/M. C) QSM; linear fit: water vials R2 = 0.938, slope = 6.16 ppm/M; agar vials R2 = 0.993, slope = 4.48 ppm/M..... 93

Figure 4.9: Diffusion curves measuring released contrast agent. A) The ratio $R2^*_{avg}(t)/R2^*_{avg}(final)$ is used as a measurement of $concentration(t)/concentration(\infty)$, representing cumulative amounts of contrast agent in the agar. An outlier (metal, 2nd week) was excluded due to poor image quality. The non-metal release curve yields a diffusion constant of $4.59 \times 10^{-11} \text{ m}^2/\text{s}$. B) The susceptibility of the calcium sulfate core measured through QSM.

The addition of metal to the calcium sulfate core increased susceptibility as expected but resulted in poor overall data quality..... 95

Figure 5.1: Representative image of the Zones of Inhibition (ZOI) observed with (A,B) *S. epidermidis* ATCC 35984 and (C,D) *S. aureus* NCTC 13143 EMRSA-16 at day 20 of rifampicin and vancomycin in combination, showing no evidence of resistant colonies (B,D) and rifampicin alone (A,C) showing potential resistant mutant colonies growing within the ZOI (black arrows). Figure reproduced from Laycock et al.¹¹ under the terms of the Creative Commons Attribution License CC-BY 4.0..... 108

List of Appendices (where applicable)

Appendix A: Creative Commons license CC BY 4.0 (https://creativecommons.org/licenses/by/4.0/)	112
Appendix B: Creative Commons licensing statements.....	113
Appendix C: Wiley policy regarding permission to use own work as dissertation	115

List of Abbreviations, Symbols, Nomenclature

2D	two-dimensional
3D	three-dimensional
CT	computed tomography
FDM	fused deposition modelling
FSE	fast spin echo
GRE	gradient echo
MEDI	morphology enabled dipole inversion
MRI	magnetic resonance imaging
PJI	periprosthetic joint infection
PLA	polylactic acid
PMMA	poly methyl methacrylate
PPM	parts per million
QSM	quantitative susceptibility mapping
R2*	effective transverse relaxation rate; $1/T2^*$
SI	signal intensity
STL	stereolithography file format
T1	longitudinal relaxation time
T2	transverse relaxation time
TR	repetition time

TE echo time
VOI volume of interest

Chapter 1

1 General Introduction

1.1 Clinical Motivation

1.1.1 Background

Joint replacements, particularly of the hip and knee, are ubiquitous, with the number of hip and knee arthroplasties in Canada rising by 38% in the past decade, with more than 138,000 surgeries costing over \$1.4 billion annually.¹ Unfortunately, the procedures are not perfect and the implants do sometimes fail, requiring surgical revision, with the most cited reasons being instability from aseptic loosening, fracture, and infection.¹ Improvements in orthopedic implant design and materials have reduced the risk of mechanical failure and thus decreased incidences of loosening; however, relatively little progress has been made in improving infection rates.² As a result, periprosthetic joint infection (PJI) is the top cited reason for joint revision in Canada in 2020-2021, comprising 25% and 33% of all hip and knee revisions, respectively.¹

The lack of progress in this area is particularly problematic because revision is generally more difficult and costly than the initial implantation;³ worse still, revision for PJI results in even higher burden than aseptic revision.^{4,5} The problem is even further exacerbated by the fact that the presence of an implant promotes infection – animal studies have shown that in the presence of a foreign body, the bacterial concentration needed to start an infection is reduced by a factor of 100 000.⁶ Orthopedic implants also suffer from the development of bacterial biofilms that protects bacteria from the host immune system,⁷ which makes PJI particularly tenacious and difficult to control with only systemic antibiotics.

1.1.2 Diagnosis of PJI

In 2018, an international consensus meeting of the Musculoskeletal Infection Society decided that there are two major diagnostic criteria for PJI: 1. Sinus tract (i.e. an

abnormal channel visible from the skin) with evidence of communication to the joint (i.e. extending to the implant) or visualization of the prosthesis; and 2. Two positive growths of the same organism (i.e. the same bacterium is found in two separate tests) using standard culture methods.⁵ While these two major criteria are well accepted, various groups differ greatly in their definitions of minor criteria, mainly concerning different biomarkers and their concentrations.⁸ A patient fulfilling either major criterion is definitively diagnosed with PJI; multiple minor criteria must be combined to form a diagnosis but how these minor criteria are weighted remains up for debate.⁵

1.1.3 Revision Procedure

Following diagnosis, the current gold standard for treating PJI is a two-stage revision (Figure 1.1), where there is a surgery to eradicate infection, which is followed by a separate surgery to replace the implant.⁹ In the first stage, the implant is removed followed by debridement (removal of necrotic and infected tissue) of the joint space. Antibiotics are mixed into poly methyl methacrylate (PMMA, bone cement) and formed into a temporary joint replacement, often called a spacer (Figure 1.1B), that is implanted in the infected site (Figure 1.1C). The infection is monitored for 6-8 weeks and, once cleared, the PMMA spacer is removed and replaced with a permanent implant. The alternative is a one-stage revision, where, as in the first stage of the two-stage procedure, the infected implant is removed followed by debridement of the joint space.¹⁰ As there will be no temporary spacer to deliver antibiotics over time, the joint is thoroughly cleaned prior to insertion of a new implant. Local antibiotic delivery can still be achieved, albeit less effectively, by cementing the implant with antibiotic-loaded bone cement¹⁰ or packing the site with antibiotic-loaded beads.¹¹ However, the costs associated with a two-stage revision are, as expected, more than double a one-stage revision.¹² The value of two-stage vs. one-stage revision is a current topic of debate among clinicians^{13,14} and a comprehensive clinical trial is underway.¹⁵ It was previously thought that the single-stage procedure would not be as effective as the two-stage treatment; however, a recent meta-analysis¹⁶ has demonstrated that reinfection rates are similar for one-stage (5.7%) and two-stage (8.4%) hip revisions and two-stage knee revisions (16.2%) may be more likely

to be reinfected than one-stage (12.7%) surgery, albeit with a limited amount of one-stage studies.

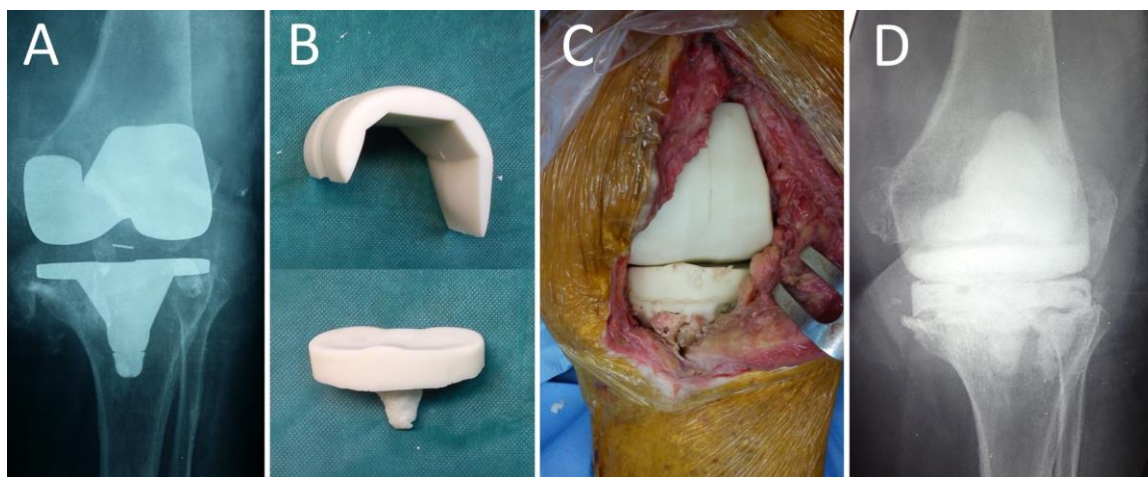


Figure 1.1: First stage of a two-stage revision. A. Preoperative radiograph of the left knee. B. The prefabricated articulated knee antibiotic-loaded cement (poly methyl methacrylate) spacer will be implanted after removal of the infected prostheses and extensive debridement and irrigation of the joint space. C. Intraoperative photograph after implantation of the spacer. D. Anteroposterior radiograph of the left knee after spacer implantation. Figure reproduced from Samelis et al.¹⁷ under the terms of the Creative Commons Attribution License CC-BY 4.0.

1.1.4 Antibiotic Carriers

A key advantage of two-stage revision is the use of an antibiotic-loaded spacer for localized drug delivery; the temporary spacer has the ability to deliver drugs directly to the periprosthetic space over an extended period of time, which results in higher effective dosage compared to systemic antibiotics.⁹ PMMA is used because it has the strength to maintain the joint space during the weeks-long treatment; however, PMMA does have limitations both mechanically and as an antibiotic carrier. Mechanically, PMMA spacers are known to suffer from dislocation and fracture¹⁷ (Figure 1.2) and as a carrier for drug delivery, PMMA is less than ideal – critically, the antibiotic concentration negatively

affects the mechanical properties^{17,18} and has relatively poor elution kinetics for two of the most important antibiotics (releasing only 6.4% and 10.17% of the loaded tobramycin and gentamycin, respectively).¹⁹ The poor elution kinetics are exacerbated by the exponentially slowing drug release,¹⁹ resulting in a burst of antibiotic activity that may be followed by an extended period where antibiotic concentration falls below minimum inhibitory concentration,²⁰ potentially even leading to bacterial growth.²¹

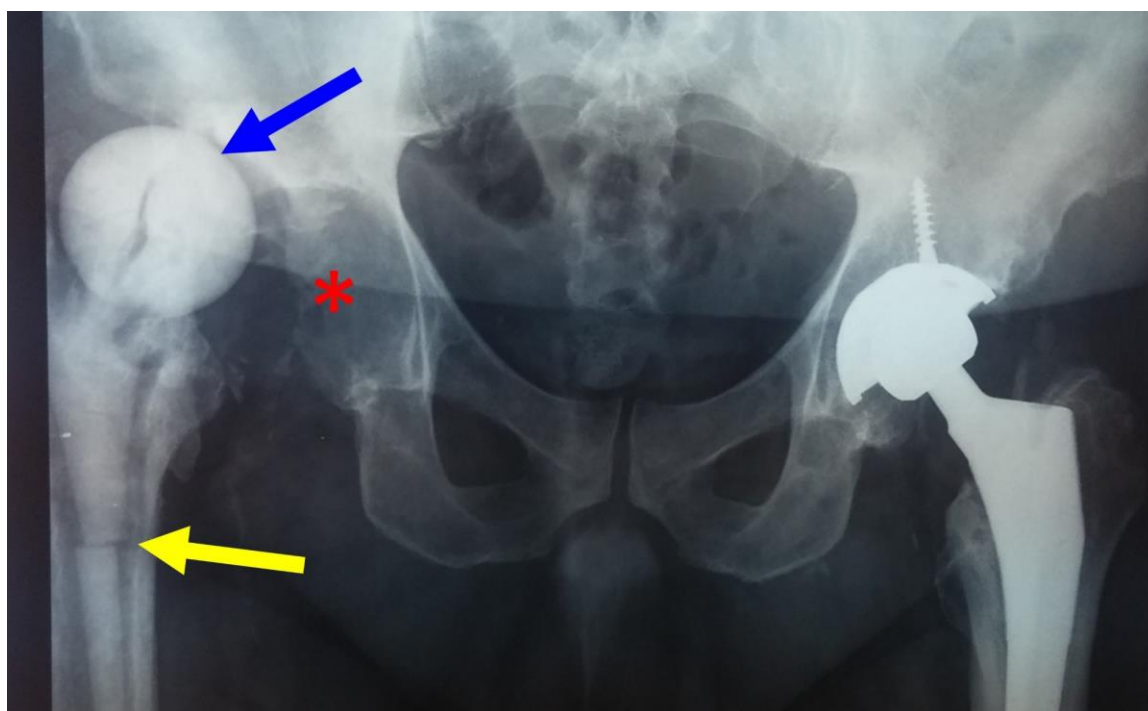


Figure 1.2: Two-stage revision for PJI after total replacement of the right hip using a prefabricated spacer. Breakage (yellow arrow) and dislocation (blue arrow) of the spacer out of the acetabulum (asterisk). Figure reproduced from Samelis et al.¹⁷ under the terms of the Creative Commons Attribution License CC-BY 4.0.

A solution to many of the problems inherent to PMMA is calcium sulfate. Calcium sulfate has been used in orthopedics for decades as a bone filler²² and bone graft substitute.²³ Calcium sulfate is also commonly used as a carrier for drug delivery in a variety of applications, including bioactive agents,²⁴ cancer related drugs,²⁵ and antibiotics.^{26,27} When loaded with antibiotics, calcium sulfate is commonly formed into

beads and packed into an infected surgical site; it is particularly well suited for treatment of PJI.^{11,28} Calcium sulfate is well known to be bio-resorbable which helps increase drug release over time, resulting in potentially maintaining sufficient drug concentrations to stay above minimum inhibitory concentration for as long as 40 days.²⁸ Unfortunately, in spite of its excellent drug delivery properties, calcium sulfate cannot directly replace PMMA due to mechanical unsuitability,²⁹ preventing the use of calcium sulfate directly in the periprosthetic space; thus, currently calcium sulfate is only deployed in the periphery to the joint, limiting its effectiveness. There is currently no means of non-invasive monitoring of drug release; quantitative analysis of antibiotic concentration in a patient is done through serum samples. Within this dissertation I will propose solutions for both problems; a method for quantitative imaging of antibiotic release from calcium sulfate, as well as a means of alleviating mechanical concerns surrounding calcium sulfate by placing it into a load-bearing scaffold.

1.2 Imaging of PJI

As previously discussed, a positive diagnosis of PJI consists of either one of two major criteria or a combination of minor criteria. Notably, imaging is not part of the standardized diagnostic process, even as a minor criterion, nor part of routine monitoring of the infection post-surgery.⁸ Although not yet routinely adopted, the use of conventional radiography (2D x-ray), computed tomography (CT), nuclear medicine, and magnetic resonance imaging (MRI) have been explored as possible avenues for improving both diagnosis and monitoring of PJI.

1.2.1 Radiography and Computed Tomography

Conventional radiography is generally the first imaging modality to be used as part of a standard exam post-arthroplasty, however diagnostic performance of 2D x-ray is low.⁸ Computed tomography has been shown to be an improvement vs. conventional radiography but is not considered reliable due to an inability to differentiate between infection and aseptic implant failure.⁸ Relative to other modalities, however, CT is faster, less expensive and more widely available. Unfortunately, periprosthetic bone

abnormalities are not useful for diagnosis of painful infection and while it is possible to find some periprosthetic soft-tissue abnormalities with CT, soft tissue contrast is not a strength of radiography.³⁰ Furthermore, CT still suffers from metal artifacts³¹ and ionizing radiation; thus, it is worthwhile to explore other options for imaging of PJI.

1.2.2 Nuclear Medicine

Nuclear medicine is routinely used for diagnosis of osteomyelitis (bone inflammation) and numerous forms of infection but remains outside the standard routine for diagnosis of PJI.⁸ Although not yet incorporated into standard use, single-photon emission computerized tomography (commonly known as SPECT) has been shown to be valuable for PJI diagnosis.³²⁻³⁴ For diagnosis of PJI, three separate scans are required: 1. bone scan, which detects increased osteoblastic activity associated with both osteomyelitis and infection by labelling with ^{99m}Tc-methylene diphosphonate; 2. leukocyte or white blood cell labelling, which consists of extracting, isolating and labelling white blood cells from venous blood plasma with either ^{99m}Tc-hexamethylpropylene amine oxime (HMPAO; quicker, more practical, and widely available) or ¹¹¹In (more accurate but more time consuming to prepare and scan) which is then reinjected, at which point the cells migrate to both infection sites and bone marrow; and 3. bone marrow scan using ^{99m}Tc- sulfur colloid, which measures bone marrow activity and thus, in combination with the previous scans, isolates infection. This procedure is highly sensitive to infection; thus, a negative test is useful in ruling out PJI.³⁵ Unfortunately, these scans are expensive and time-consuming while also lacking the specificity needed for use as a definitive test for PJI,³⁵ which prevents nuclear medicine from being the ultimate solution for imaging-based diagnosis of PJI.

1.2.3 Magnetic Resonance Imaging

MRI is well established in diagnosing many symptoms of musculoskeletal infection³⁶ however metal artifacts have historically been too severe to extend the utility of MRI to PJI. This is unfortunate because MRI is highly suited for looking at soft tissue, which is known to be relevant to PJI.³⁰ The soft tissue contrast generated by MRI has motivated

the recent development of metal artifact reduction schemes^{37,38} that have proved to be able to generate diagnostically useful images with MRI around failing implants, including in diagnosing PJI.³⁹⁻⁴¹ Unfortunately, these dedicated artifact reduction sequences do come with a prolonged scan time, which has made them difficult to justify for routine use.⁴² In this work, I will demonstrate that, although traditional solid joint replacements likely require dedicated artifact reduction, porous implants may not; this is due to a reduction in effective magnetic susceptibility proportional to the porosity of an implant.

1.3 MRI Metal Artifacts

MRI would be a valuable tool for diagnosing PJI for many of the same reasons that it is relied on for non-implant related musculoskeletal infection. MRI is established for evaluating sinus tracts surrounding infected joints (without implants),³⁶ which, if found to extend to an implant, are a major criterion for establishing a PJI diagnosis. Unfortunately, MRI suffers from artifacts when scanning around anything with a susceptibility that is different from water (resulting in a dimensionless field shift typically stated in ppm); artifacts of this nature are routinely encountered in the form of fat (3.5 ppm shift) and air (9 ppm shift).⁴³ The metals commonly used in orthopedics, such as titanium (182 ppm shift) and cobalt-chrome (1300 ppm shift),⁴⁴ have susceptibilities that are orders of magnitude higher than fat and air; this results in proportionally worse artifacts that affect large volumes surrounding many orthopedic implants. Metal artifacts are specifically addressed in chapter 3 of this thesis, where the potential for porous implants to exhibit lower artifacts is explored.

1.3.1 Susceptibility Artifacts

MRI uses a number of well calibrated magnetic fields (B_0 , B_1 , gradients) to induce a measurable signal from tissue. Generating an image from these measurements assumes that these fields are homogenous in order to localize the signal to voxels. There are a variety of factors that affect the calibration of the magnetic fields that generate an inherent field inhomogeneity, most of which are corrected by shimming. However, field inhomogeneity is also produced by the object in the scanner due to magnetic

susceptibility effects. Magnetic susceptibility is a dimensionless material property typically expressed as

$$\vec{M} = \chi \vec{H} \quad (1.1)$$

where χ is the magnetic susceptibility of the material, \vec{M} is the magnetization of the material, and \vec{H} is the magnetic field strength.⁴⁵ Magnetic susceptibility effectively generates a small magnetic field wherever there are two materials of differing susceptibility. Materials are classified depending on the direction of their induced field relative to the applied field; they can either be diamagnetic (opposite) or paramagnetic (aligned). Figure 1.3 demonstrates this effect through simulations of cylinders made of three materials relevant to this thesis; calcium sulfate is slightly diamagnetic relative to water and titanium alloy and cobalt-chrome are highly paramagnetic.

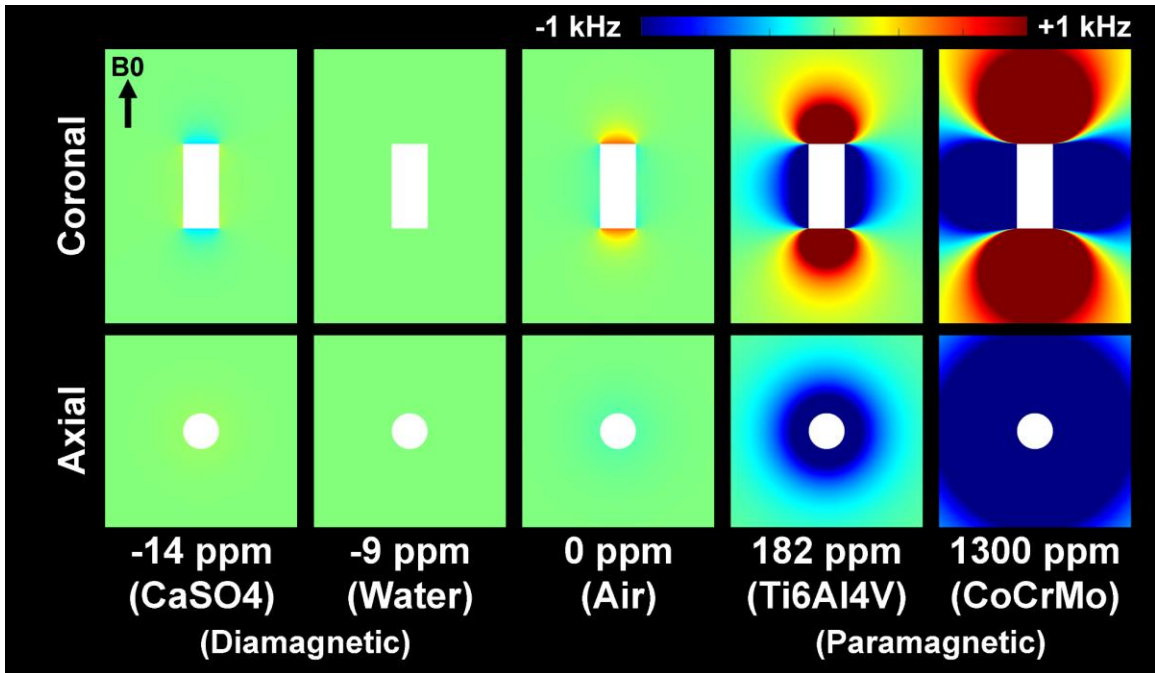


Figure 1.3: Simulated field maps surrounding a cylinder of varying magnetic susceptibility representing materials relevant to this thesis. Negative susceptibilities are diamagnetic and positive susceptibilities are paramagnetic.

Susceptibility-induced field inhomogeneity is detrimental to both localization and signal quality, and orthopedic implants are often made of high susceptibility metals.⁴⁴ These implants will often generate field inhomogeneities substantial enough to bring local frequency shifts outside the excitation bandwidth (Figure 1.4A, top; ~12 mm on either end of the cylinder), resulting in a signal void. The susceptibility induced field also generates steep gradients in the volume adjacent to the metal (Figure 1.4B, blue), which introduces intravoxel dephasing and thus faster signal decay (Figure 1.4B, circled). Furthermore, signal localization is typically accomplished through a combination of frequency and phase encoding. Phase encoding is mostly impervious to frequency shift-related artifacts, but the susceptibility induced field can cause inaccuracies in frequency encoding that result in geometric distortion.⁴⁶ Frequency encoding assigns signal to a location based on resonance frequency through applying a linear gradient field. This linear relationship is violated by the susceptibility-induced local fields generated by metal (i.e. the non-flat regions of the field map in Figure 1.5), which can be of similar strength to the gradient field, resulting in signal pileup (Figure 1.5A, circled; signal from multiple locations assigned to the same spot), and signal loss.⁴⁷

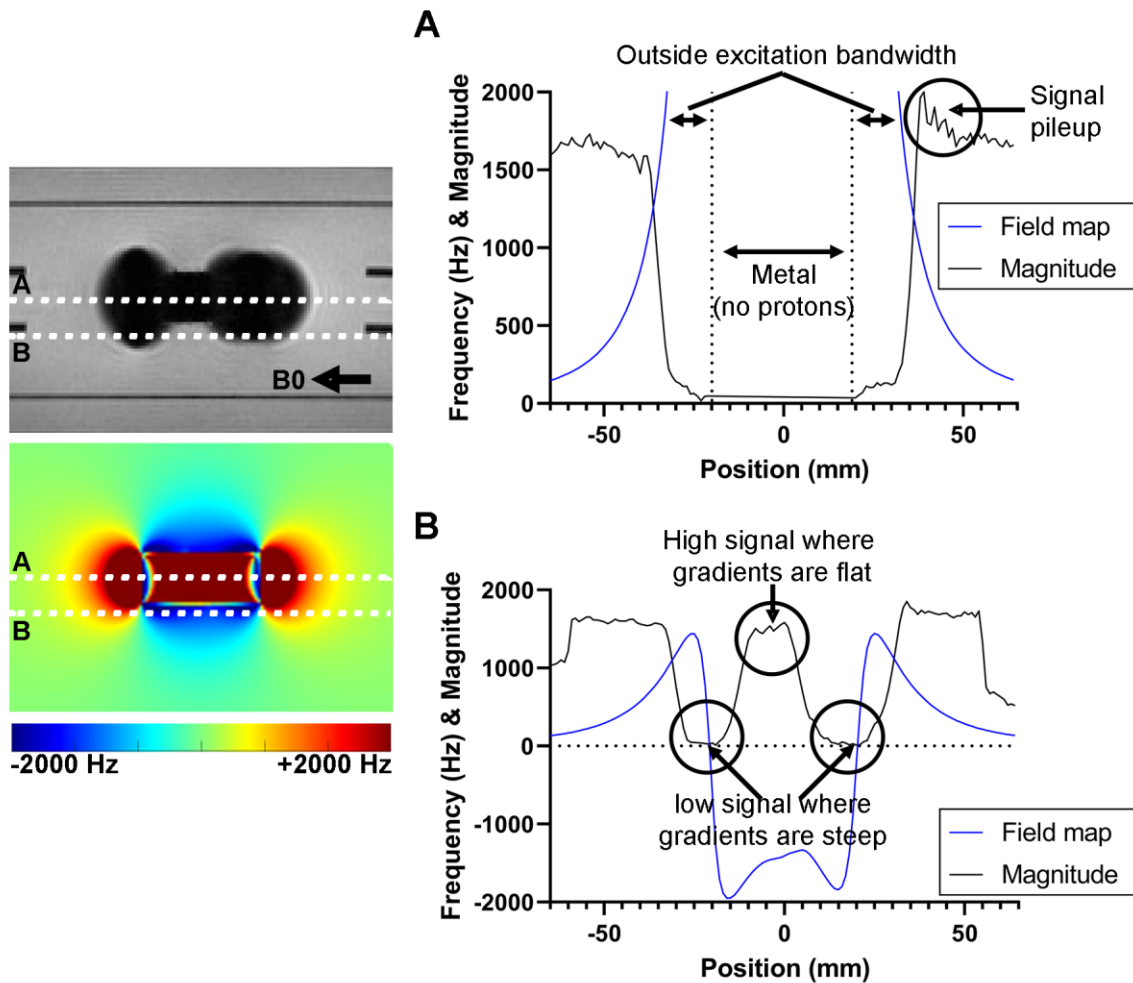


Figure 1.4: Magnitude image and corresponding simulated field map of a titanium cylinder, used to demonstrate various sources of signal loss and artifacts. A) Magnitude and frequency shifts through the center of the cylinder, showing signal loss from unexcited protons and signal pileup. B) Magnitude and frequency shift 10 mm off-center, showing a region without metal but still affected by signal loss where there are steep field gradients.

1.3.2 Artifact Reduction in MRI

Although they typically involve significant tradeoffs, there are a few commonly used ways to mitigate susceptibility artifacts. In the presence of metal, sequences with high readout bandwidth, short echo time, and spin-echo (rather than gradient-echo) should be

used in a lower-field scanner.⁴² Increasing readout bandwidth is the key parameter for reducing signal misplacement, as a higher bandwidth per voxel results in a smaller spatial displacement due to off-resonance signal, but also results in capturing more noise, decreasing signal-to-noise ratio. Short echo times also reduce artifact by acquiring data before the rapidly decaying signal (due to inhomogeneity-induced dephasing) gets too small to measure. Spin-echo sequences are preferred over gradient-echo sequences as the refocusing pulse will generate an echo out of spins whose magnetic field remains static between excitation and echo formation – a condition generally met by metal implant-induced fields as they are governed only by implant orientation (relative to B₀) and magnetization (which encompasses both field strength and material susceptibility). This is not the case for gradient-echoes as the recalled echo will not refocus spins that have been affected by fields other than the gradient itself, so any inhomogeneity proves to be problematic. It is also often preferable to use a 3D acquisition, as the two phase-encoded dimensions limit distortion to only one frequency-encoded dimension. Lastly, as seen in equation 1.1, magnetization is proportional to field strength; thus, it is wise to avoid imaging metal implants in a high-field scanner.

Unfortunately, many orthopedic metal implants are very large and thus create proportionally large field distortions.⁴⁴ These large distortions create substantial volumes of protons that are entirely outside the excitation bandwidth and are thus lost prior to acquisition. Techniques have recently been developed to try and capture some of this off-resonance signal by effectively doing multiple overlapping scans with varying center frequency. The details of their implementation are outside the scope of this thesis; however, their basic mechanism involves shifting the center frequency of the excitation pulse of a 3D spin-echo sequence over a predetermined range and using the off-resonance information to fill in signal voids (MAVRIC)³⁷ or resolve through-plane distortion (SEMAC).³⁸ Although these multispectral acquisitions have been optimized sufficiently to be used clinically, the acquisition of multiple volumes will always carry a scan-time penalty. Large off-resonance volumes also complicates many forms of quantitative imaging due to the unpredictable gradients and local frequency shifts generated by the magnetization of metal, as well as the poor performance of gradient-echo in this inhomogeneous environment.

1.3.3 Field Map Simulation

An important tool for understanding and investigating off-resonance artifacts are field map simulations. As a consequence of equation 1.1, only the z-component (aligned with B_0) of the magnetic field is affected by susceptibility-induced field perturbation, thus the relative field shift induced ($\delta(\vec{r})$) within a susceptibility distribution is defined as:

$$\delta(\vec{r}) = \frac{B_z(\vec{r}) - B_0(1 + \chi_e(\vec{r}))}{B_0} \quad (1.2)$$

where $B_z(\vec{r})$ is the magnetic field induced within a susceptibility distribution $\chi(\vec{r})$ embedded within external medium with susceptibility $\chi_e(\vec{r})$.⁴⁸ The induced field within the external medium can be well approximated by the superposition of the fields induced by each member of $\chi(\vec{r})$, which forms the basis of field map simulations. The most general method to simulate phenomena related to field inhomogeneity are Bloch simulations, where the Bloch equations, which describe signal evolution, are discretized, calculated and summed. However, this process can be done quickly and accurately using a Fourier-based method, as described by Bouwman et. al.,⁴⁸ and has been shown to be effective in simulating metal artifacts arising in gradient echo MRI.⁴⁹ Chapter 3 of this thesis relies on this simulation to accurately estimate the effective susceptibility of porous metal structures and demonstrate the relationship between porosity and susceptibility.

1.4 Quantitative Imaging

Conventional MRI relies on qualitative analysis of images whose contrast is weighted for longitudinal (T1) or transverse (T2) relaxation times. MRI of the musculoskeletal system has traditionally relied mostly on these conventional imaging techniques; recently, however, quantitative imaging has been explored for musculoskeletal applications.⁵⁰ Quantitative MRI provides measurements of tissue composition and structure by gathering additional data, usually by acquiring multiple datasets with some varying parameter (such as changing echo times), that can be fit or manipulated to extract information about underlying MR properties from the relationships between the acquired images. This process can also be used to calculate concentrations of gadolinium-based

solutions as both transverse relaxation rates ($R2^*$) and magnetic susceptibility are known to be proportional to concentration.⁵¹ This ability proves to be useful for studying contrast agent activity beyond just signal enhancement – this work exploits this capability to measure small-molecule (contrast agent) release from a carrier material (calcium sulfate) in a manner that could act as a surrogate for tracking antibiotic release, which is an important capability for treatment of PJI.

1.4.1 Transverse Relaxation Rate ($R2^*$)

The natural decay of transverse magnetization ($T2$) is governed primarily by the interaction of spins with their atomic and molecular environment. However, due to $B0$ inhomogeneity, observed signal decays faster than would be predicted by natural causes; quantification of this observed decay is expressed either as $T2^*$ (time) or $R2^*$ (rate = $1/T2^*$). A very high $R2^*$ (rapid signal loss) is the cause of signal loss artifact surrounding metal where the induced frequency shift gradients are very steep, causing high intravoxel inhomogeneity. $R2^*$ can be measured through fitting an exponential relationship between signal intensity (SI) and echo time (TE):

$$SI = ke^{-TE \cdot R_2^*} \quad (1.3)$$

with the data required for fitting typically acquired through a multi-echo GRE. One key application of $R2^*$ is to measure concentration, typically of iron⁵² (in red blood cells), as $R2^*$ is known to be linearly correlated to concentration. For this work, we exploit the fact that $R2^*$ is proportional to gadolinium concentration⁵¹ to quantify contrast agent diffusing out of a carrier material.

1.4.2 Quantitative Susceptibility Mapping

Using phase data, multi-echo images are able to calculate local frequency shifts and generate a field map. The frequency of a voxel is calculated by the phase accumulation (difference) between echo times (TE_1 , TE_2) through the Hermitian product:

$$\Delta\omega = \frac{\angle[I_{TE_2}I_{TE_1}^*]}{2\pi(TE_2 - TE_1)} \quad (1.4)$$

With this field map, it is possible to do a forward estimate of the susceptibility of the objects generating the local frequency shifts, a technique dubbed quantitative susceptibility mapping (QSM). After removing background field contributions, QSM aims to generate a susceptibility map through dipole inversion, a process that involves deconvolution of a dipole kernel to calculate a source susceptibility value. This inversion is an ill-posed problem in that some regions of the kernel are undefined, leading to an indeterminate solution. One widely used QSM algorithm, Morphology Enabled Dipole Inversion (MEDI)⁵³, overcomes this problem using information gleaned from magnitude images to localize the edges of the object whose susceptibility is being estimated. Although MEDI was designed and tested for use in brain imaging, the algorithm was studied using gadolinium-based phantoms; thus, in chapter 4 I have used it to estimate the susceptibility change of the calcium sulfate carrier to quantify the release of gadolinium from its matrix.

1.5 3D-printed orthopedic implants

3D-printing, also referred to as additive manufacturing, refers to fabrication techniques that generate 3-dimensional objects layer-by-layer, usually based on computer-aided designs. This layer-by-layer process is in contrast to traditional manufacturing methods, which fall into two broad categories: subtractive manufacturing, such as milling, or formative manufacturing, such as casting and forging. 3D-printing is attractive because it is capable of fabricating highly complex shapes and finely detailed geometry without significant impact on cost or time, opening the door for creative and novel designs. 3D-printing is also well established for rapid prototyping and custom builds because

manufacturing costs do not decrease with scale; thus, it is affordable to fabricate one-off versions of designs. This ability is having an impact on medical research and practice, especially for patient specific tools and implants.⁵⁴ 3D-printing is used extensively throughout this thesis as a means of fabricating both 3D-printed porous metal implants and customized plastic phantoms.

1.5.1 Overview of 3D-printing techniques

3D-printing employs many different techniques for layer generation to build with a wide variety of materials.⁵⁵ The majority of 3D-printers are based on extrusion of plastic, typically in filament form; this process, called fused deposition modelling (FDM), typically involves feeding plastic into a moving hot-end that melts and extrudes a thin (100s of microns) stream onto a bed (Figure 1.5A). Resin-based 3D-printers are also very popular; these operate using a liquid photopolymer that solidifies when exposed to a curing light. One technique (PolyJet; Stratasys, Rehovot, Israel) for printing with photopolymers is to deposit liquid photopolymer onto a print-bed in a manner similar to an inkjet printer (Figure 1.5B) and cured with a UV light. Metal objects can also be 3D-printed through selective laser sintering/melting; this process uses a high-powered laser to sinter/melt a thin layer of fine metal powder (Figure 1.5C) and is also often called powder bed fusion.

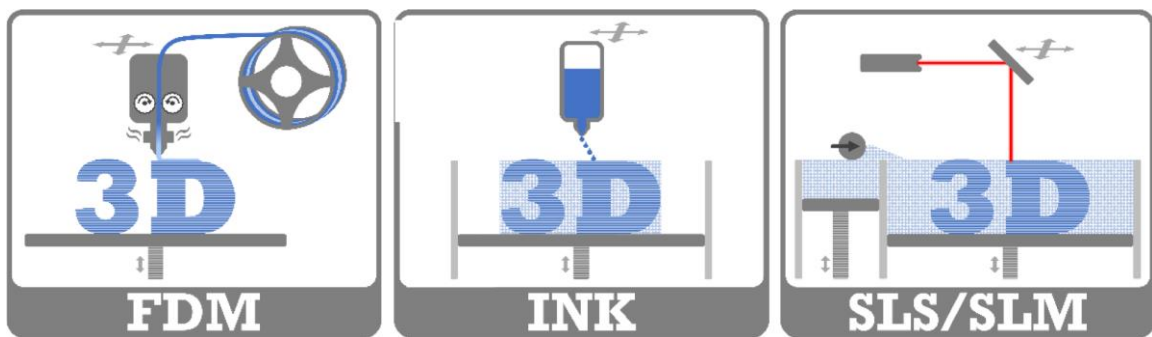


Figure 1.5: Schematic illustration of the different printing techniques. Left: fused deposition modeling; Center: 3D inkjet; Right: selective laser sintering/selective laser melting. Figure adapted and modified from Domsta & Seidlitz⁵⁵ under the terms of the Creative Commons Attribution License CC-BY 4.0.

1.5.2 Existing orthopedic applications of 3D-printing

Most of the early application for 3D-printing in orthopedics, particularly prior to the widespread availability of metal 3D-printing, was for surgical guides and creating models for surgical planning.⁵⁶ Metal 3D-printing has only recently developed into a widespread commercial technology; this newfound accessibility has already prompted the development of clinically relevant 3D-printed components. Of particular interest in orthopedics is the ability to 3D-print with well-established biocompatible metals, such as stainless steel, Ti6Al4V titanium alloy, and CoCrMo cobalt-chrome alloy, that are commonly used in implants.⁴⁴ A major attraction of metal 3D-printed implants is the ability to create porous implants, which have been shown to have a number of useful properties, including excellent osseointegration⁵⁷⁻⁵⁹ and the potential to reduce stress shielding, thus reducing bone loss.⁶⁰⁻⁶² Porous implants are difficult or impossible to manufacture using traditional fabrication methods, hence the quick clinical adoption of metal 3D-printing for a few key applications.

Two major applications for 3D-printed porous implants are spinal implants and acetabular cups. One of the most exciting applications of porous metal implants is for lumbar interbody fusion, which is a procedure designed to fuse two vertebral segments by inserting a fusion cage into the disc space and letting bone growth fuse the joined vertebral bodies. 3D-printed titanium spinal cages are quickly gaining clinical traction and early returns are proving promising.⁶³ 3D-printed porous acetabular cups are also commercially available; studies comparing traditionally made and 3D-printed titanium porous cups have shown little difference between them, but additive manufacturing reduces production costs and material use.^{64,65} These early clinical applications are promising and show that 3D-printed titanium components are safe, which is an encouraging sign for future development of 3D-printed implants.

1.5.3 Relevance for PJI

Although spinal cages and acetabular cups have not shown increased rate of infection,⁶³⁻⁶⁵ infection of 3D-printed implants, mainly due to the rougher surface created by 3D-

printing, remains a concern.⁶⁶ This concern has motivated research into surface coatings for porous implants, some of which offer both antibacterial and osseointegration benefits.⁶⁷ Another growing approach to this problem is incorporating an antibiotic carrier, such as gelatin⁶⁸ or hydrogels,⁶⁹ into the pores of a porous structure. This approach has the benefit of being able to hold a sufficient reservoir of drugs to act as a drug delivery system, which allows antibiotics to diffuse directly into the joint space surrounding a porous implant.

Clinically implemented porous titanium implants have already shown excellent mechanical suitability with relatively primitive designs. There are many studies looking into the mechanical properties of various potential geometries for porous structures which may prove better than what is used in current implant designs.⁷⁰ For this thesis, I have chosen the sheet-based gyroid⁷¹ as the basic cell-type for designing the porous metal structures used in my studies. The sheet-based gyroid has been shown to be mechanically suited for orthopedic use, particularly with regards to fatigue due to a lack of stress concentrations,⁷² and has been successfully implemented in a rat femur fixation plate, where the gyroid-based implant demonstrated excellent bone ingrowth and mechanical properties similar to an intact control.⁷³ The interconnected pores are also helpful for filling with carrier material, in this case calcium sulfate, and the porosity is easily controllable through wall thickness or cell size.

1.6 Thesis objectives

The ultimate goal of this thesis is to fill the unmet need for non-invasive diagnosis and routine monitoring of PJI through MRI. In the following chapters I will describe the work done in order to achieve this objective; this includes developing the tools needed to evaluate geometric distortion and artifacts, demonstrating that porous metal implants have magnetic susceptibility proportional to porosity, and studying the ability of quantitative MRI to track small molecule diffusion from a drug carrier intended for local delivery of antibiotics.

Chapter 2: Centroid-Based Analysis of Customizable 3D-Printed MRI Distortion Phantoms – describes the design, fabrication and analysis of a phantom to quantify image distortion through spherical markers. This phantom is also highly customizable, which is demonstrated by embedding a hip implant and examining the resulting in-plane and through-plane distortion. The centroid-based analysis of marker locations described in this study is also important for the following chapters as a means of identifying co-registration points for determining phantom orientation. Paper in preparation for submission.

Chapter 3: Effective Magnetic Susceptibility of 3D-Printed Porous Metal Scaffolds – studies the effective magnetic susceptibility and associated artifacts induced by gyroid-based porous metal scaffolds. The objective of this study was to quantify, through comparison of simulated and acquired field maps, the effective susceptibility of porous metal scaffolds of varying porosity. This proved that porosity and susceptibility are linearly correlated and also demonstrated the feasibility of MRI around highly porous implants. The low susceptibility (and resulting minimization of artifacts) will be useful for imaging porous implants and also justified the inclusion of a highly porous scaffold in the next chapter. Paper published in *Magnetic Resonance in Medicine*⁷⁴ (MRM, 2022 Jun; DOI: 10.1002/mrm.29136).

Chapter 4: Characterizing Diffusion-Controlled Release of Small-Molecules Using Quantitative MRI: Application to Orthopedic Infection – aims to fulfill an important unmet need for tracking small molecule diffusion during treatment of PJI. This study proposes the use of a gadolinium-based contrast agent as a surrogate small-molecule for the antibiotics typically loaded into a calcium sulfate carrier. The gadolinium is then tracked using quantitative imaging, which enabled concentration measurements that are used to characterize diffusion-controlled release by fitting to an established drug-release model. The study is done both with calcium sulfate alone and placed within a highly porous metal scaffold using R2* and QSM as analogs for gadolinium concentration. Paper in preparation for submission.

The thesis concludes with a brief summary of accomplishments and limitations of the previous chapters, followed by an overview of potential future work.

1.7 References

1. Canadian Institute for Health Information. Canadian joint replacement registry: 2020–2021 full annual report. Ottawa, ON: CIHI; 2022.
2. Premkumar A, Kolin DA, Farley KX, Wilson JM, McLawhorn AS, Cross MB, Sculco PK. Projected economic burden of periprosthetic joint infection of the hip and knee in the united states. *J Arthroplasty* 2021;36(5):1484-1489.e1483.
3. Fang CJ, Shaker JM, Ward DM, Jawa A, Mattingly DA, Smith EL. Financial burden of revision hip and knee arthroplasty at an orthopedic specialty hospital: Higher costs and unequal reimbursements. *J Arthroplasty* 2021;36(8):2680-2684.
4. Parvizi J, Gehrke T, Chen AF. Proceedings of the international consensus on periprosthetic joint infection. *Bone Joint J* 2013;95-b(11):1450-1452.
5. Parvizi J, Tan TL, Goswami K, Higuera C, Della Valle C, Chen AF, Shohat N. The 2018 definition of periprosthetic hip and knee infection: An evidence-based and validated criteria. *J Arthroplasty* 2018;33(5):1309-1314.e1302.
6. Kapadia BH, Berg RA, Daley JA, Fritz J, Bhave A, Mont MA. Periprosthetic joint infection. *Lancet* 2016;387(10016):386-394.
7. McConoughey SJ, Howlin R, Granger JF, Manning MM, Calhoun JH, Shirtliff M, Kathju S, Stoodley P. Biofilms in periprosthetic orthopedic infections. *Future Microbiol* 2014;9(8):987-1007.
8. Romanò CL, Petrosillo N, Argento G, Sconfienza LM, Treglia G, Alavi A, Glaudemans AWJM, Gheysens O, Maes A, Lauri C, Palestro CJ, Signore A. The role of imaging techniques to define a peri-prosthetic hip and knee joint infection: Multidisciplinary consensus statements. *Journal of clinical medicine* 2020;9(8):2548.
9. Charette RS, Melnic CM. Two-stage revision arthroplasty for the treatment of prosthetic joint infection. *Curr Rev Musculoskelet Med* 2018;11(3):332-340.
10. Nguyen M, Sukeik M, Zahar A, Nizam I, Haddad FS. One-stage exchange arthroplasty for periprosthetic hip and knee joint infections. *Open Orthop J* 2016;10:646-653.
11. Abosala A, Ali M. The use of calcium sulphate beads in periprosthetic joint infection, a systematic review. *J Bone Jt Infect* 2020;5(1):43-49.
12. Mponponsuo K, Leal J, Puloski S, Chew D, Chavda S, Au F, Rennert-May E. Economic burden of surgical management of surgical site infections following hip and knee replacements in calgary, alberta, canada. *Infect Control Hosp Epidemiol* 2021:1-8.

13. Sotiriou D, Stigbrand H, Ullmark G. Is two-stage revision surgery for infected hip arthroplasty worth the suffering, resources and results compared to one-stage? *Hip Int* 2020;1120700020949162.
14. van den Kieboom J, Tirumala V, Box H, Oganessian R, Klemt C, Kwon YM. One-stage revision is as effective as two-stage revision for chronic culture-negative periprosthetic joint infection after total hip and knee arthroplasty. *Bone Joint J* 2021;103-b(3):515-521.
15. Strange S, Whitehouse MR, Beswick AD, Board T, Burston A, Burston B, Carroll FE, Dieppe P, Garfield K, Goberman-Hill R, Jones S, Kunutsor S, Lane A, Lenguerrand E, MacGowan A, Moore A, Noble S, Simon J, Stockley I, Taylor AH, Toms A, Webb J, Whittaker JP, Wilson M, Wylde V, Blom AW. One-stage or two-stage revision surgery for prosthetic hip joint infection--the inform trial: A study protocol for a randomised controlled trial. *Trials* 2016;17:90.
16. Goud AL, Harlianto NI, Ezzafzafi S, Veltman ES, Bekkers JEJ, van der Wal BCH. Reinfection rates after one- and two-stage revision surgery for hip and knee arthroplasty: A systematic review and meta-analysis. *Arch Orthop Trauma Surg* 2021.
17. Samelis PV, Papagrigorakis E, Sameli E, Mavrogenis A, Savvidou O, Koulouvaris P. Current concepts on the application, pharmacokinetics and complications of antibiotic-loaded cement spacers in the treatment of prosthetic joint infections. *Cureus* 2022;14(1):e20968.
18. Lilikakis A, Sutcliffe MP. The effect of vancomycin addition to the compression strength of antibiotic-loaded bone cements. *Int Orthop* 2009;33(3):815-819.
19. DiCicco M, Duong T, Chu A, Jansen SA. Tobramycin and gentamycin elution analysis between two in situ polymerizable orthopedic composites. *J Biomed Mater Res B Appl Biomater* 2003;65(1):137-149.
20. Neut D, van de Belt H, van Horn JR, van der Mei HC, Busscher HJ. Residual gentamicin-release from antibiotic-loaded polymethylmethacrylate beads after 5 years of implantation. *Biomaterials* 2003;24(10):1829-1831.
21. Anagnostakos K, Hitzler P, Pape D, Kohn D, Kelm J. Persistence of bacterial growth on antibiotic-loaded beads: Is it actually a problem? *Acta Orthop* 2008;79(2):302-307.
22. Thomas MV, Puleo DA. Calcium sulfate: Properties and clinical applications. *J Biomed Mater Res B Appl Biomater* 2009;88(2):597-610.
23. Moore WR, Graves SE, Bain GI. Synthetic bone graft substitutes. *ANZ J Surg* 2001;71(6):354-361.

24. Orellana BR, Hilt JZ, Puleo DA. Drug release from calcium sulfate-based composites. *J Biomed Mater Res B Appl Biomater* 2015;103(1):135-142.
25. Phillips H, Maxwell EA, Schaeffer DJ, Fan TM. Simulation of spatial diffusion of platinum from carboplatin-impregnated calcium sulfate hemihydrate beads by use of an agarose gelatin tissue phantom. *Am J Vet Res* 2018;79(6):592-599.
26. Maale GE, Eager JJ, Mohammadi DK, Calderon FA, 2nd. Elution profiles of synthetic caso(4) hemihydrate beads loaded with vancomycin and tobramycin. *Eur J Drug Metab Pharmacokinet* 2020;45(4):547-555.
27. Laycock PA, Cooper JJ, Howlin RP, Delury C, Aiken S, Stoodley P. In vitro efficacy of antibiotics released from calcium sulfate bone void filler beads. *Materials (Basel)* 2018;11(11).
28. Lum ZC, Pereira GC. Local bio-absorbable antibiotic delivery in calcium sulfate beads in hip and knee arthroplasty. *J Orthop* 2018;15(2):676-678.
29. Cavelier S, Tanzer M, Barthelat F. Maximizing the strength of calcium sulfate for structural bone grafts. *J Biomed Mater Res A* 2020;108(4):963-971.
30. Cyteval C, Hamm V, Sarrabère MP, Lopez FM, Maury P, Taourel P. Painful infection at the site of hip prosthesis: CT imaging. *Radiology* 2002;224(2):477-483.
31. Wellenberg RHH, Hakvoort ET, Slump CH, Boomsma MF, Maas M, Streekstra GJ. Metal artifact reduction techniques in musculoskeletal CT-imaging. *Eur J Radiol* 2018;107:60-69.
32. Teiler J, Ahl M, Åkerlund B, Brismar H, Holstensson M, Gabrielson S, Hedlund H, Axelsson R. 99mtc-hmpao-wbc spect/CT versus 18f-fdg-wbc PET/CT in chronic prosthetic joint infection: A pilot study. *Nucl Med Commun* 2022;43(2):193-200.
33. Kim HO, Na SJ, Oh SJ, Jung BS, Lee SH, Chang JS, Bin SI, Ryu JS. Usefulness of adding spect/CT to 99mtc-hexamethylpropylene amine oxime (hmpao)-labeled leukocyte imaging for diagnosing prosthetic joint infections. *J Comput Assist Tomogr* 2014;38(2):313-319.
34. van der Bruggen W, Bleeker-Rovers CP, Boerman OC, Gotthardt M, Oyen WJ. Pet and spect in osteomyelitis and prosthetic bone and joint infections: A systematic review. *Semin Nucl Med* 2010;40(1):3-15.
35. Sconfienza LM, Signore A, Cassar-Pullicino V, Cataldo MA, Gheysens O, Borens O, Trampuz A, Wörtler K, Petrosillo N, Winkler H, Vanhoenacker F, Jutte PC, Glaudemans A. Diagnosis of peripheral bone and prosthetic joint infections: Overview on the consensus documents by the eanm, ebjis, and esr (with escmid endorsement). *Eur Radiol* 2019;29(12):6425-6438.

36. Alaia EF, Chhabra A, Simpfendorfer CS, Cohen M, Mintz DN, Vossen JA, Zoga AC, Fritz J, Spritzer CE, Armstrong DG, Morrison WB. MRI nomenclature for musculoskeletal infection. *Skeletal Radiol* 2021;50(12):2319-2347.
37. Koch KM, Brau AC, Chen W, Gold GE, Hargreaves BA, Koff M, McKinnon GC, Potter HG, King KF. Imaging near metal with a mavric-semac hybrid. *Magn Reson Med* 2011;65(1):71-82.
38. Lu W, Pauly KB, Gold GE, Pauly JM, Hargreaves BA. Slice encoding for metal artifact correction with noise reduction. *Magn Reson Med* 2011;65(5):1352-1357.
39. Filli L, Jungmann PM, Zingg PO, Rüdiger HA, Galley J, Sutter R, Pfirrmann CWA. MRI with state-of-the-art metal artifact reduction after total hip arthroplasty: Periprosthetic findings in asymptomatic and symptomatic patients. *Eur Radiol* 2020;30(4):2241-2252.
40. Galley J, Sutter R, Stern C, Filli L, Rahm S, Pfirrmann CWA. Diagnosis of periprosthetic hip joint infection using MRI with metal artifact reduction at 1.5 T. *Radiology* 2020;296(1):98-108.
41. Schwaiger BJ, Gassert FT, Suren C, Gersing AS, Haller B, Pfeiffer D, Dangelmaier-Dawirs J, Roski F, von Eisenhart-Rothe R, Prodinger PM, Woertler K. Diagnostic accuracy of MRI with metal artifact reduction for the detection of periprosthetic joint infection and aseptic loosening of total hip arthroplasty. *Eur J Radiol* 2020;131:109253.
42. Peschke E, Ulloa P, Jansen O, Hoenner JB. Metallic implants in MRI - hazards and imaging artifacts. *Rofo* 2021;193(11):1285-1293.
43. Schenck JF. The role of magnetic susceptibility in magnetic resonance imaging: MRI magnetic compatibility of the first and second kinds. *Med Phys* 1996;23(6):815-850.
44. Smith MR, Artz NS, Wiens C, Hernando D, Reeder SB. Characterizing the limits of MRI near metallic prostheses. *Magn Reson Med* 2015;74(6):1564-1573.
45. Brown RW, Cheng Y-CN, Haacke EM, Thompson MR, Venkatesan R. Magnetic resonance imaging: Physical principles and sequence design: John Wiley & Sons; 2014.
46. Artz NS, Hernando D, Taviani V, Samsonov A, Brittain JH, Reeder SB. Spectrally resolved fully phase-encoded three-dimensional fast spin-echo imaging. *Magn Reson Med* 2014;71(2):681-690.
47. Dillenseger JP, Moliere S, Choquet P, Goetz C, Ehlinger M, Bierry G. An illustrative review to understand and manage metal-induced artifacts in musculoskeletal MRI: A primer and updates. *Skeletal Radiol* 2016.

48. Bouwman JG, Bakker CJ. Alias subtraction more efficient than conventional zero-padding in the fourier-based calculation of the susceptibility induced perturbation of the magnetic field in MR. *Magn Reson Med* 2012;68(2):621-630.
49. Zijlstra F, Bouwman JG, Braskute I, Viergever MA, Seevinck PR. Fast fourier-based simulation of off-resonance artifacts in steady-state gradient echo MRI applied to metal object localization. *Magn Reson Med* 2016.
50. de Mello R, Ma Y, Ji Y, Du J, Chang EY. Quantitative MRI musculoskeletal techniques: An update. *AJR Am J Roentgenol* 2019;213(3):524-533.
51. Olsson E, Wirestam R, Lind E. MRI-based quantification of magnetic susceptibility in gel phantoms: Assessment of measurement and calculation accuracy. *Radiol Res Pract* 2018;2018:6709525.
52. Christiansen SD, Liu J, Boffa MB, Drangova M. Simultaneous $r(2^*)$ and quantitative susceptibility mapping measurement enables differentiation of thrombus hematocrit and age: An in vitro study at 3 T. *J Neurointerv Surg* 2019;11(11):1155-1161.
53. Liu J, Liu T, de Rochefort L, Ledoux J, Khalidov I, Chen W, Tsiouris AJ, Wisnieff C, Spincemaille P, Prince MR, Wang Y. Morphology enabled dipole inversion for quantitative susceptibility mapping using structural consistency between the magnitude image and the susceptibility map. *Neuroimage* 2012;59(3):2560-2568.
54. Aimar A, Palermo A, Innocenti B. The role of 3D printing in medical applications: A state of the art. *J Healthc Eng* 2019;2019:5340616.
55. Domsta V, Seidlitz A. 3D-printing of drug-eluting implants: An overview of the current developments described in the literature. *Molecules* 2021;26(13).
56. Tack P, Victor J, Gemmel P, Annemans L. 3D-printing techniques in a medical setting: A systematic literature review. *Biomed Eng Online* 2016;15(1):115.
57. Cheong VS, Fromme P, Coathup MJ, Mumith A, Blunn GW. Partial bone formation in additive manufactured porous implants reduces predicted stress and danger of fatigue failure. *Ann Biomed Eng* 2020;48(1):502-514.
58. Cheong VS, Fromme P, Mumith A, Coathup MJ, Blunn GW. Novel adaptive finite element algorithms to predict bone ingrowth in additive manufactured porous implants. *J Mech Behav Biomed Mater* 2018;87:230-239.
59. Mumith A, Cheong VS, Fromme P, Coathup MJ, Blunn GW. The effect of strontium and silicon substituted hydroxyapatite electrochemical coatings on bone ingrowth and osseointegration of selective laser sintered porous metal implants. *PLoS One* 2020;15(1):e0227232.

60. Arabnejad S, Johnston B, Tanzer M, Pasini D. Fully porous 3D printed titanium femoral stem to reduce stress-shielding following total hip arthroplasty. *J Orthop Res* 2017;35(8):1774-1783.
61. Carpenter RD, Klosterhoff BS, Torstrick FB, Foley KT, Burkus JK, Lee CSD, Gall K, Guldberg RE, Safranski DL. Effect of porous orthopaedic implant material and structure on load sharing with simulated bone ingrowth: A finite element analysis comparing titanium and peek. *J Mech Behav Biomed Mater* 2018;80:68-76.
62. Zaharin HA, Abdul Rani AM, Azam FI, Ginta TL, Sallih N, Ahmad A, Yunus NA, Zulkifli TZA. Effect of unit cell type and pore size on porosity and mechanical behavior of additively manufactured ti6al4v scaffolds. *Materials (Basel)* 2018;11(12).
63. Corso KA, Kothari P, Corrado K, Michielli A, Ruppenkamp J, Bowden D. Early revision events among patients with a three dimensional (3D) printed cellular titanium or peek (polyetheretherketone) spinal cage for single-level lumbar spinal fusion. *Expert Rev Med Devices* 2021:1-7.
64. Wyatt MC, Kieser DC, Frampton CMA, Woodfield T, Hooper GJ. How do 3D-printed primary uncemented acetabular components compare with established uncemented acetabular cups? The experience of the new zealand national joint registry. *Hip Int* 2022;32(1):73-79.
65. Castagnini F, Caternicchia F, Biondi F, Masetti C, Faldini C, Traina F. Off-the-shelf 3D printed titanium cups in primary total hip arthroplasty. *World J Orthop* 2021;12(6):376-385.
66. Jing Z, Zhang T, Xiu P, Cai H, Wei Q, Fan D, Lin X, Song C, Liu Z. Functionalization of 3D-printed titanium alloy orthopedic implants: A literature review. *Biomed Mater* 2020;15(5):052003.
67. Suchý T, Vištejnová L, Šupová M, Klein P, Bartoš M, Kolinko Y, Blassová T, Tonar Z, Pokorný M, Sucharda Z, Žaloudková M, Denk F, Ballay R, Juhás Š, Juhásová J, Klapková E, Horný L, Sedláček R, Grus T, Čejka Z, Jr., Čejka Z, Chudějová K, Hrabák J. Vancomycin-loaded collagen/hydroxyapatite layers electrospun on 3D printed titanium implants prevent bone destruction associated with s. Epidermidis infection and enhance osseointegration. *Biomedicines* 2021;9(5).
68. Cai B, Huang L, Wang J, Sun D, Zhu C, Huang Y, Li S, Guo Z, Liu L, Feng G, Li Y, Zhang L. 3D printed multifunctional ti(6)al(4)v-based hybrid scaffold for the management of osteosarcoma. *Bioconjug Chem* 2021;32(10):2184-2194.
69. Qiao S, Wu D, Li Z, Zhu Y, Zhan F, Lai H, Gu Y. The combination of multifunctional ingredients-loaded hydrogels and three-dimensional printed porous

titanium alloys for infective bone defect treatment. *J Tissue Eng* 2020;11:2041731420965797.

70. Tan XP, Tan YJ, Chow CSL, Tor SB, Yeong WY. Metallic powder-bed based 3D printing of cellular scaffolds for orthopaedic implants: A state-of-the-art review on manufacturing, topological design, mechanical properties and biocompatibility. *Mater Sci Eng C Mater Biol Appl* 2017;76:1328-1343.
71. Schoen AH. Reflections concerning triply-periodic minimal surfaces. *Interface Focus* 2012;2(5):658-668.
72. Kelly CN, Francovich J, Julmi S, Safranski D, Guldberg RE, Maier HJ, Gall K. Fatigue behavior of as-built selective laser melted titanium scaffolds with sheet-based gyroid microarchitecture for bone tissue engineering. *Acta Biomater* 2019;94:610-626.
73. Kelly CN, Lin AS, Leguineche KE, Shekhar S, Walsh WR, Guldberg RE, Gall K. Functional repair of critically sized femoral defects treated with bioinspired titanium gyroid-sheet scaffolds. *J Mech Behav Biomed Mater* 2021;116:104380.
74. Hong G, Liu J, Cobos SF, Khazaei T, Drangova M, Holdsworth DW. Effective magnetic susceptibility of 3D-printed porous metal scaffolds. *Magn Reson Med* 2022;87(6):2947-2956.

Chapter 2

2 Centroid-Based Analysis of Customizable 3D-Printed MRI Distortion Phantoms

2.1 Introduction

The capability for routine and accurate characterization of geometric distortion is becoming increasingly important for MRI applications, including image-guided radiotherapy,¹⁻³ quantitative brain imaging,⁴ repeatability of quantitative imaging for osteoarthritis across sites^{5,6} and for the preparation of patient-specific positioning guides in orthopedic surgery.^{7,8} The importance of this type of quality assurance is well established by a standard set by the American College of Radiology, detailing a standardized image quality measurement protocol and phantom.^{9,10} However, this currently employs time consuming manual analysis in spite of evidence showing potential for automation.¹¹ Furthermore, it is a standard set prior to the rise of now prevalent high-field magnets, which brings to question the field-strength dependent factors that affect geometric distortions in MRI, including main-field inhomogeneity, gradient-field non-linearity and susceptibility-induced field perturbations.^{12,13} There are clear and substantial improvements to be made upon these standards, particularly in creating a phantom that can be easily analyzed automatically.

A variety of geometric distortion phantoms containing fiducial structures with well-known geometry providing reference control points to determine distortion have been proposed and used. Early phantoms achieved robust and automated 2D in-plane distortion analysis with fluid filled tubes by measuring the center of mass of signal in a 2D slice perpendicular to the tubes.¹⁴ The first 3D distortion phantoms relied on stacked regular grids submerged in signal generating fluid whose intersections were used as the reference control points. The analysis of these grid phantoms can be done either manually¹⁵ or through a semi-automated analysis of corner points.¹⁶ Phantoms consisting of commercial interlocking plastic bricks, which are customizable and have the benefit of being easily

and precisely reproduced across multiple sites with low cost, have been described; these phantoms require sophisticated analysis based on spherical harmonic expansion.¹⁷ Recent developments in distortion phantoms have trended towards a 3D distribution of signal-generating markers, aimed towards simplifying analysis. One such phantom consists of a direct 3-dimensional adaptation of the earlier tube-based phantom, consisting of layered and orthogonally arranged sheets with holes submerged in fluid.¹⁸ However, the markers in this type of phantom were not distributed over the entire volume, thus lacking true 3D analysis. Phantoms amenable to 3D distortion analysis include fluid-filled cavities sandwiched between plates¹⁹ analyzed through template matching, or high-contrast markers embedded within a supporting solid structure,²⁰ analyzed through straightforward center-of-mass calculations. Ideally, there would be a means to combine the positives of each design type: the simple design of the repeating grid intersections, the reproducibility of commercial interlocking bricks and the ease of 3D analysis provided by the embedded high contrast markers.

One application for a phantom amenable to automated analysis of geometric distortion is related to artifacts surrounding metal implants. Susceptibility-induced field perturbations arise from the magnetic field generated by differences in magnetic susceptibility, most commonly encountered with fat and air. The distortion is proportional to susceptibility difference, and thus seriously hampers MRI around metal implants. Reduction of these severe artifacts is difficult but not impossible, as recent advancements in metal artifact correction²¹⁻²⁵ in orthopedic imaging have shown. These artifact-reduction techniques have relied on phantoms to aid development and evaluation, but the phantoms used were simple, and these distortions have proven difficult to analyze quantitatively. Distortion phantoms for the evaluation of artifact-correction techniques have typically consisted of qualitative analysis of the artifact originating from a metal test object, sometimes embedded within a cutout planar grid, suspended in agar. A more complex 3D phantom, consisting of stacks of 2D plates surrounding an embedded metal rod²⁶ has been developed, but has not been adapted for more complex shapes. Susceptibility-induced distortions around more complicated metal objects, such as orthopedic implants, adds new challenges as there is often a large signal void surrounding the implant. Furthermore, the distortions are dependent on both the shape and orientation of the object, resulting in

less predictable effects. These factors work together to complicate the use of template-matching analysis schemes used in quantifying other forms of geometric distortion. Lastly, phantoms analyzing real implants (as opposed to a simple metal rod) must be able to both hold the implant and surround it with markers, necessitating implant-specific customizability in the phantom's design.

3D-printing has made it possible to create accurate plastic structures of any desired 3-dimensional shape, providing a new platform for designing and building geometric distortion phantoms. 3D-printed adaptations of grid intersections,²⁷ fluid filled cavities,²⁸ and contrast markers²⁹ have been developed and analyzed using similar methods to their traditionally fabricated counterparts. There have also been recent advances in highly sophisticated analysis methods to better localize control points at cylindrical grid intersections³⁰ that are applied to a custom-built 3D-printed construct. 3D-printing also provides a platform to create new designs that are not limited to the restrictions of traditional fabrication methods; we seek to take advantage of this flexibility to combine elements of previous designs into a new design that is only feasible through 3D-printing.

One particular advantage of 3D-printing we seek to employ is the ability to seamlessly manufacture an array of spherical beads on a supporting structure, which is difficult to accomplish through machining. This approach allows for a customizable 3D construct whose fiducial markers are readily differentiable from the supporting structure, based on size. This differentiability allows for morphological erosion of the supporting structure, leaving an array of unattached marker beads whose centroids can be calculated to quantitatively determine marker locations. 3D-printing also allows for highly customizable designs which can be used to encapsulate a test object, even those with complicated geometry such as implants, with marker beads in three dimensions to measure susceptibility-induced effects. The purpose of this study is to design, fabricate and validate a scalable 3D-printed fiducial grid phantom design that combines centroid-based marker bead analysis with simple and robust grid-based fabrication. This work explores the phantom's amenability to automated generation of volumetric distortion maps, and the ability to evaluate large susceptibility-induced distortions surrounding an embedded object.

2.2 Materials & Methods

An effective distortion phantom must fulfill a number of requirements. Fundamentally, the phantom must contain known geometry, typically in the form of markers, identifiable in MR images. Current designs achieve this by employing either solid grid intersections surrounded by signal generating fluid, or high contrast markers embedded into a solid construct. Clinical viability requires the distortion analysis to be both volumetric and automated, which is accomplished with a 3D distribution of markers that provide quantifiable control points for software analysis. Fabrication of the phantom should be as simple and repeatable as possible, allowing for scalability to any size and reproducibility across sites. For use in susceptibility-induced distortion analysis, the design must be customizable to hold and surround an embedded test object. We aim to achieve this with a new type of distortion phantom that takes full advantage of 3D-printing to build a design that is not feasible to create with traditional fabrication methods.

2.2.1 Concept

The goal of the proposed phantom design is to locate and identify markers with centroid-based center of mass calculations in a submerged grid design. The idea that makes this possible is the attachment of an array of spherical marker beads at the intersections of a grid, supported by a structure that is thin – relative to the marker beads – allowing it to be removed through morphological erosion in post-processing.³¹ 3D-images are acquired and, to improve the accuracy of image segmentation, corrected for signal-intensity drop-off in the axial and trans-axial directions, using fitted parabolic functions. The resulting image of a dark grid (plastic) on a bright background (fluid) is segmented based on grey-scale threshold. As the sphere's radius is larger than the supporting structures, application of morphological erosion with an appropriately sized kernel can be used to remove the supports from the image, as described in a patent assigned to Holdsworth et al.³² This processing leaves a cloud of spherical markers of smaller diameter without moving each fiducial's center of mass, which are then identified and centroided to create a 3D point-cloud of observed grid locations. These measured locations are compared to the best-fit locations of a synthesized grid, based on the physical spacing of the grid. This process

generates a 3D vector map of sub-voxel geometric distortion throughout the image volume.

2.2.2 Design and 3D-Printing

Two versions of the proposed phantom were designed, each tailored to the capabilities of two 3D-printing technologies: photopolymerization (PolyJet) and fused deposition modeling (FDM). The phantoms consist of an isotropic grid of solid spherical fiducial markers (4.5 mm diameter beads) placed at 13 mm intervals (large spacing chosen to avoid partial-volume and susceptibility-related artifacts) with support structures suited for each 3D-printing process. The design for photopolymer fabrication consisted of markers placed on the intersections of a cubic lattice formed of cylindrical struts, which we will refer to as the “strut-based phantom”. Optimization for FDM, which is best suited for building structures vertically, led to a design consisting of spheres attached to a grid of vertical supporting walls, which will be referred to as the “wall-based phantom”. Phantom design was performed using AutoDesk Fusion 360 (Autodesk, San Rafael, CA) solid-modelling computer-aided design.

The strut-based phantom’s cubic lattice system consists of repeating unit cells featuring a spherical marker integrated onto the intersection of three orthogonal cylinders, whose diameter is chosen to be small enough to be removed in processing but thick enough to support the phantom without flexing (Figure 2.1A). The unit cells were arranged to form a 5x5x10 distribution of markers (Figure 2.1B) and 3D printed using a Stratasys Objet 30 Pro (Stratasys, Eden Prairie, MN) with VeroClear RGD810 transparent photopolymer resin. The wall-based phantom also consists of a repeating unit cell, but with the spherical marker integrated into orthogonal walls that are two layers thick (0.8 mm for this 3D-printer; Figure 2.1C). For this study, a grid of 580 fiducial markers conforming to a 11.4 cm diameter, 14 cm long cylinder (Figure 2.1D) was 3D-printed (with solid infill) on a commercial FDM printer (Dremel® 3D-20 Idea Builder, Dremel, Mount Prospect, IL) using white polylactic acid (PLA) filament (Dremel DF01-01). The walls were designed to be perpendicular to the printer’s bed and aligned with its X and Y directions, facilitating accurate printing by minimizing simultaneous actuation of both directional

motors, and the wall thickness was specifically chosen to be twice the extrusion width of the 3D printer to further optimize the tool path of the extruder. In order to prevent trapping of air bubbles on the phantom surface when submerged for imaging, 5x5 mm square perforations were introduced within the walls between markers.

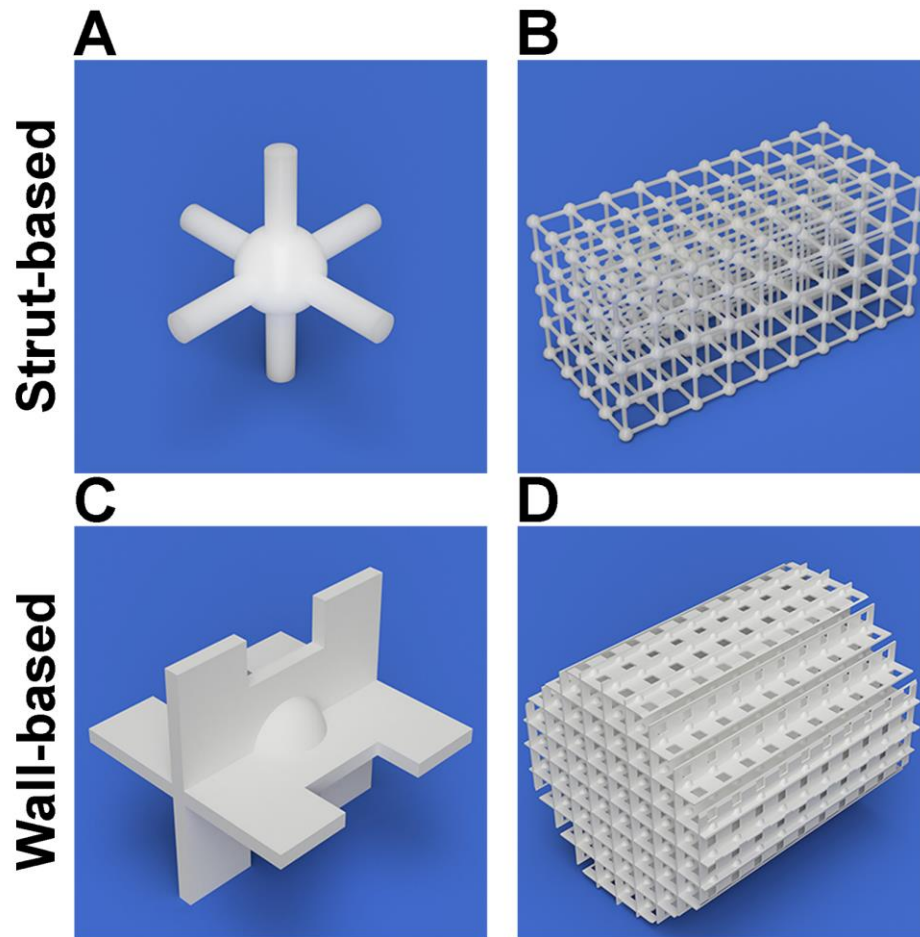


Figure 2.1: Renderings of the phantom design. A) 4.5 mm diameter spherical marker attached to 1.5 mm diameter strut-based supports. B) Strut-based phantom composed of 5x5x10 markers. C) 4.5 mm diameter spherical marker attached to 0.8 mm thick wall-based supports. D) Wall-based phantom cut to cylindrical profile (580 markers).

The phantoms are submerged within an acrylic cylinder (114 mm inner diameter, 300 mm long) known to have susceptibility similar to water³³ and filled with 7.8 mmol copper sulphate (CuSO_4) saline solution for radiofrequency-coil loading (Figure 2.2).³⁴ Air

bubbles, which aggregate on the phantom surface, were removed by adding surfactant to the saline solution followed by evacuation in a vacuum chamber for 24 hours.

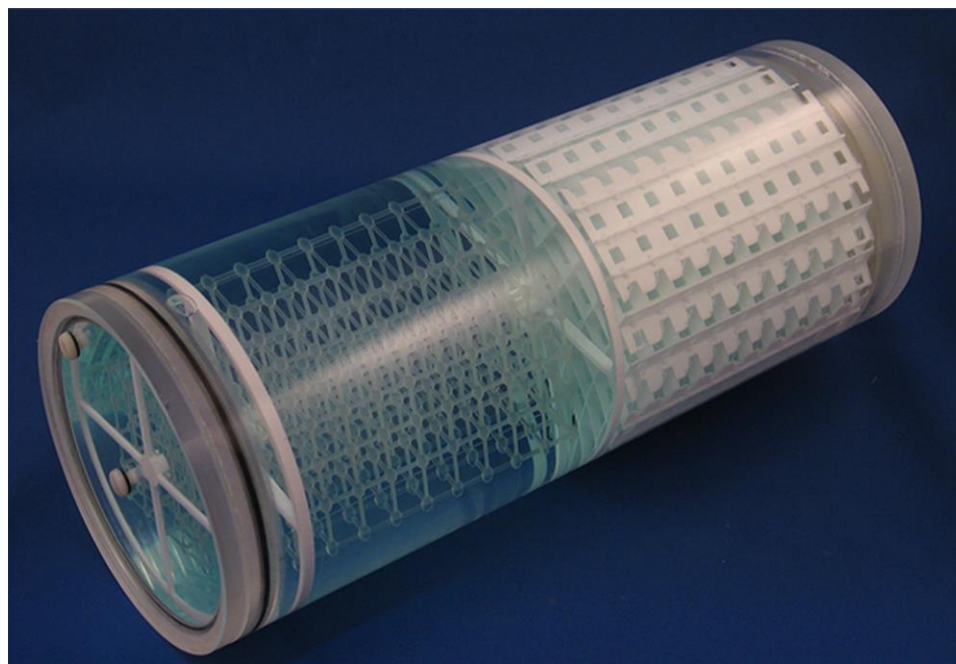


Figure 2.2: Strut- and wall-based phantoms submerged in CuSO₄ saline solution within 11.4 cm diameter cylinder. Strut-based phantom is centered with a 3D-printed PLA holder.

2.2.3 Automated Analysis Software

Automated analysis aims to isolate the fiducial markers within a 3D image, calculate their sub-voxel locations and find the deviation of image markers from their physical location. To generate a binary image, intensity inhomogeneities are first removed using parametric bias field correction³⁵ followed by thresholding to distinguish the plastic (no signal) from the surrounding solution. Isolation of the markers is achieved through morphological erosion of this binary image using a kernel (structuring element) of radius greater than the support size, but smaller than the 4.5 mm diameter markers; this is achieved with kernel sizes of 1.7 mm and 1.3 mm to remove the 1.5 mm diameter struts and 0.8 mm walls, respectively. Once the cloud of markers has been isolated, individual marker centroids are calculated, labeled based on position and converted into control points for analysis.

The regularly spaced distribution of markers allows the known geometry to be co-registered (using the iterative closest point algorithm) and compared with the known true locations of the labeled control points, generating deviation vectors at each control point.

The analysis software was implemented in C++ using the ITK and VTK libraries (Kitware Inc., Clifton Park, NY) and runs on a Linux desktop. The user specifies the in-plane geometric configuration of the markers and the number of repetitions along the axial extent, erosion kernel radius, and the threshold value. The resulting deviation vector maps were rendered using Paraview (Kitware Inc., Clifton Park, NY).

2.2.4 Fabrication Accuracy

The dry phantoms were scanned in air using a micro CT scanner (eXplore Ultra, GE Healthcare, Chicago, IL). Marker deviation analysis was done with the automated analysis software using a 1.4 mm erosion kernel and 13 mm marker spacing. Dimensional changes stemming from water absorption were measured by comparing the phantom's surface marker spacing when dry and after soaking the phantoms for 7 days. Marker positions along the surface of 5x5x10 bead (65x65x130 mm) configurations of the wall-based and strut-based phantoms (5x10 plane of markers on 4 sides) were measured with a measuring microscope (STM-6, Olympus, Tokyo, Japan).

2.2.5 Imaging

To ensure that the phantom materials do not introduce susceptibility-related geometric distortion, a field map was acquired to study any adverse effects stemming from the magnetic susceptibility of the PLA and VeroClear. The field map was calculated from the Hermitian inner product of the phase images^{36,37} of coronal scans of the 5x5x10 bead versions of the wall- and strut-based phantom which were acquired on a GE Discovery MR750 3T scanner (GE Healthcare, Waukesha, WI) using the birdcage head coil and a 3D GRE sequence with echo times 0.5 ms apart (256x128x128 matrix; 25.6 cm FOV, 1 mm thickness for 1 mm isotropic voxels; TE = 3, 3.5 ms; TR = 15 ms, 10° flip angle, ±125 kHz BW). The magnitude images were analyzed to identify individual marker centroids using a scheme similar to the automated distortion analysis. The resulting field

maps were analyzed in Matlab (Mathworks, Natick, MA) for frequency shifts generated by the plastic markers by creating two 11.3 mm diagonal line profiles in the axial plane, which avoids crossing the supporting structure, centered on the calculated centroids. Twenty markers from the wall-based and strut-based phantom (40 total) were averaged to reduce noise from the background field.

The images used for automated MR distortion analysis consists of CUBE TSE scans acquired with the following parameters: TR = 2300 ms, TE=90 ms, 0.7 mm resolution, 0.7 mm slice thickness, 62.5 kHz bandwidth and a 320x320x160 matrix acquired in an 8-channel knee coil (Invivo, Gainesville, FL) on a GE 3T Discovery MR750 scanner (GE Healthcare, Waukesha, WI). The effect of a changed B₀ field was evaluated with distortion maps of the phantom scanned with the coil at isocenter and 10 cm off-center, generated using a spherical erosion kernel of 1.7 mm to remove the struts or 1.3 mm to remove the walls. For consistency, a PLA holder positioned the strut-based phantom to maintain similar locations in the magnet and deviation analysis was done on the same number of marker beads for both phantoms by cropping the central 5x5x8 units of the wall-based phantom to match the strut-based phantom.

2.2.6 Custom Insert Phantom

The rigidity of the wall-based phantom provides a unique capability to include test objects (*e.g.* implants, vials of contrast solution, air cavities) within the phantom. We expanded the wall-based grid phantom design to surround a test object with regularly spaced fiducial markers, while firmly holding the object in place. Encapsulation of a test object is achieved by splitting the CAD design of the wall-based phantom into modules and creating a cavity that is generated from an STL model of the test object, without removing any partial markers adjacent to the insert. To retain the regularity of the 3D marker grid, custom press-fit clips (Figure 2.3A) were designed to link the modules together. To demonstrate this capability, we built a phantom where the test object was a hip implant (Smith & Nephew Synergy, titanium stem with cobalt-chrome head). Three modules were required (Figure 2.3B); each module was 3D-printed separately, and the implant was inserted prior to linking (Figure 2.3C).

The custom insert phantom provides the capacity for analysis of 3D susceptibility-induced geometric distortion and is particularly useful in the examination of simultaneous in-plane and through-plane distortion in 2D acquisitions. To demonstrate this capability, axial images were acquired with 3 mm slices separated by 3.5 mm, bisecting the planes of spherical markers and the midpoints between them, with a 2D FSE-STIR sequence with the following parameters: TR = 9000 ms, TE = 50 ms, 0.7 mm in-plane resolution, matrix = 320x192, 3 mm slice thickness, 3.5 mm spacing, NEX=2, BW=41.67. In-plane distortions were quantified by comparing the spacing of the centroids in the image with the known spacing of the markers and through-plane distortions were observed through the presence or absence of markers, depending on the slice location.

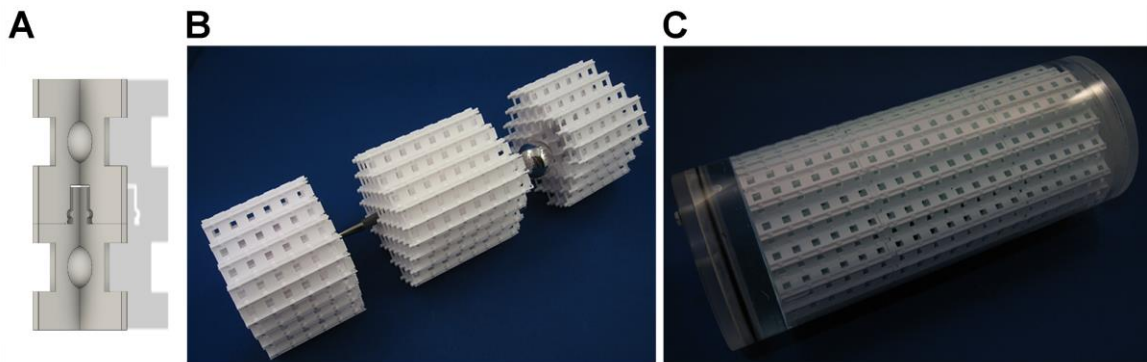


Figure 2.3: Custom insert phantom holding a hip implant. A) Custom press-fit clips that link the three modules together. B) Photo of the modules and hip implant prior to assembly. C) Assembled phantom submerged in CuSO₄ saline solution within 11.4 cm diameter cylinder

Fully automated analysis of susceptibility-induced distortion is made challenging by the presence of unpredictable signal voids surrounding the insert, as the analysis fails to differentiate markers from other low-signal regions. We developed a semi-automated approach to this problem where centroids from all low-signal volumes are calculated, markers are identified based on roundness (if length, width, and height are similar) and size (if length, width, and height are all less than 6 mm), and then manually inspected for any remaining erroneous centroids prior to comparing the identified markers (any markers that could not be centroided were ignored) against known marker locations. This

analysis is demonstrated on a marker plane bisecting a titanium hip stem (without the cobalt-chrome head) cropped from an image acquired with a CUBE 3D TSE with the following parameters: TR = 3000 ms, TE=36 ms, 1 mm isotropic resolution, 62.5 kHz bandwidth and a 15x15x30 cm field of view.

2.2.7 Statistical Analysis

To demonstrate the effectiveness of the phantoms, comparisons between distortion maps scanned at isocenter and shifted 10 cm off-center were done with paired a t-test comparing deviations in x,y and z. In all cases a P value < 0.05 was considered as significant. All statistical analyses were performed using GraphPad Prism 7.0 (GraphPad Software, La Jolla, CA).

2.3 Results

2.3.1 Fabrication Accuracy

The automated distortion analysis relies on having accurate geometry information – most importantly an accurate spacing between adjacent markers. Analysis of micro-CT images of both phantoms, using the automated distortion analysis software, shows that both dry phantoms have inherently small geometric errors relative to MRI voxel sizes (~0.5 mm at best), with a mean deviation magnitude of 0.12 ± 0.08 mm for the strut-based phantom and 0.13 ± 0.06 mm for the wall-based phantom (Figure 2.4). The CT measurements show that the 3D-printing process results in an accurately built phantom, but further measurements were required to determine the phantom's accuracy while submerged in an aqueous solution. The measuring microscope, measuring the outer surface of both phantoms, showed that, when submerged, the strut-based phantom's mean marker spacing increases by 0.09 mm whereas the wall-based phantom's marker spacing only increases by 0.01 mm (Table 2.1). As the microscope measured spacing is more indicative of the true spacing in MR, the “submerged phantom” measurements were used in the automated distortion analysis of the MR images.

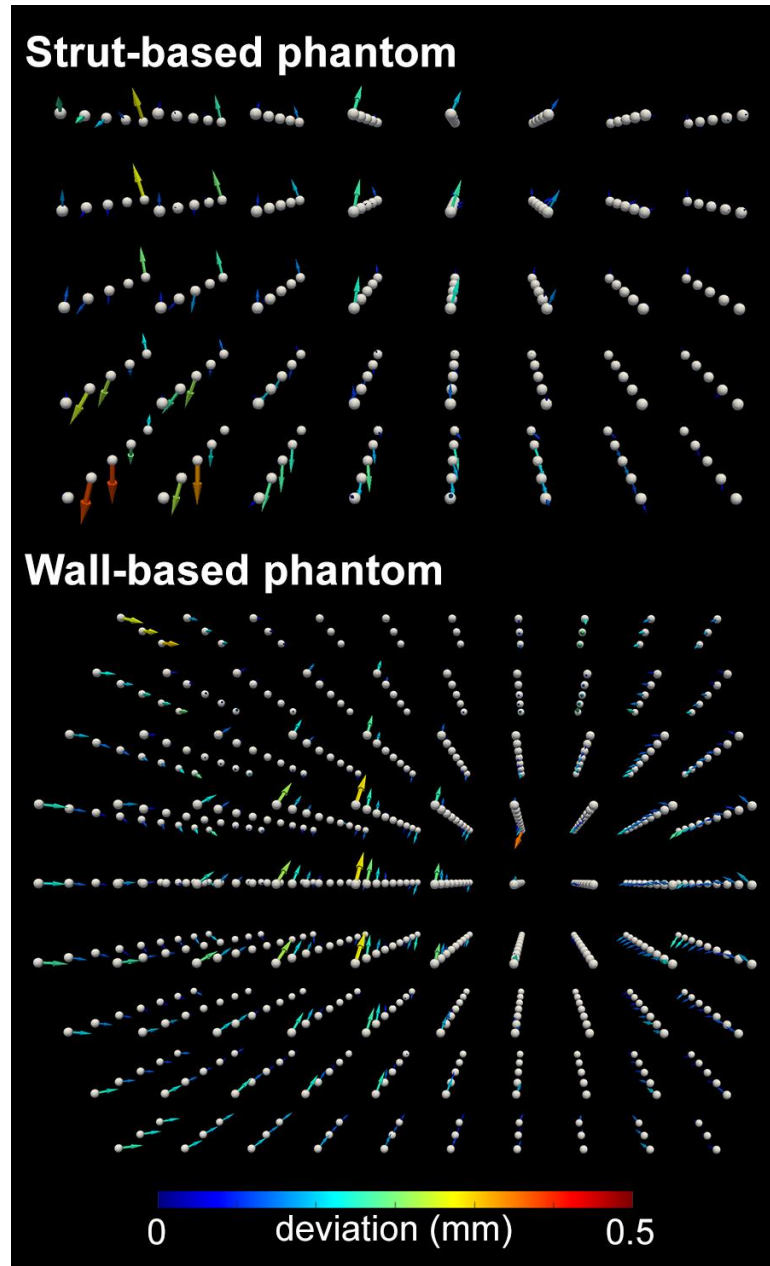


Figure 2.4: Marker deviations in CT. The strut-based phantom markers have a mean deviation magnitude of 0.122 ± 0.08 mm and the wall-based phantom have a mean deviation magnitude of 0.130 ± 0.06 mm.

Table 2.1: Measurements of phantom fabrication accuracy from measuring microscope and automated analysis of CT images

	Strut-based	Wall-based
Mean Dry Spacing (Microscope)	12.98 ± 0.03 mm	12.97 ± 0.05 mm
Mean Wet Spacing (Microscope)	13.07 ± 0.03 mm	12.98 ± 0.05 mm
Water Uptake by Mass	1.74%	10.4%
Mean Centroid Deviation (CT)	0.122 ± 0.08 mm	0.130 ± 0.06 mm

2.3.2 Automated Distortion Analysis

Having established the phantom's dimensional accuracy, both materials were tested to ensure the plastics' susceptibility does not induce distortion in the other beads. Marker centroids were successfully identified and line profiles generated, with the resulting averaged frequency shift shown in Figure 2.5. The large standard deviations in the three central voxels are due to low signal, which generates noisy phase measurements that result in poor field mapping. The mean frequency shift of the voxels adjacent to the plastic bead (2.83 mm from the center) is $+33.9 \pm 18.7$ Hz (range: -39 to +73 Hz) and $+7.0 \pm 11.0$ Hz (range: -21 to +34 Hz) for the strut-based and wall-based phantoms, respectively.

Images of both the strut-based and wall-based phantoms (Figure 2.6) were analyzed with the custom automated distortion analysis software to generate a map of distortion vectors showing the difference in position of the markers in the image relative to their known physical spacing. (Figure 2.7). Between the centered and off-center images, the change in magnitude of the vectors proved insignificant; however, paired t-tests confirm that the individual components (x,y,z) of the distortion vectors do change significantly.

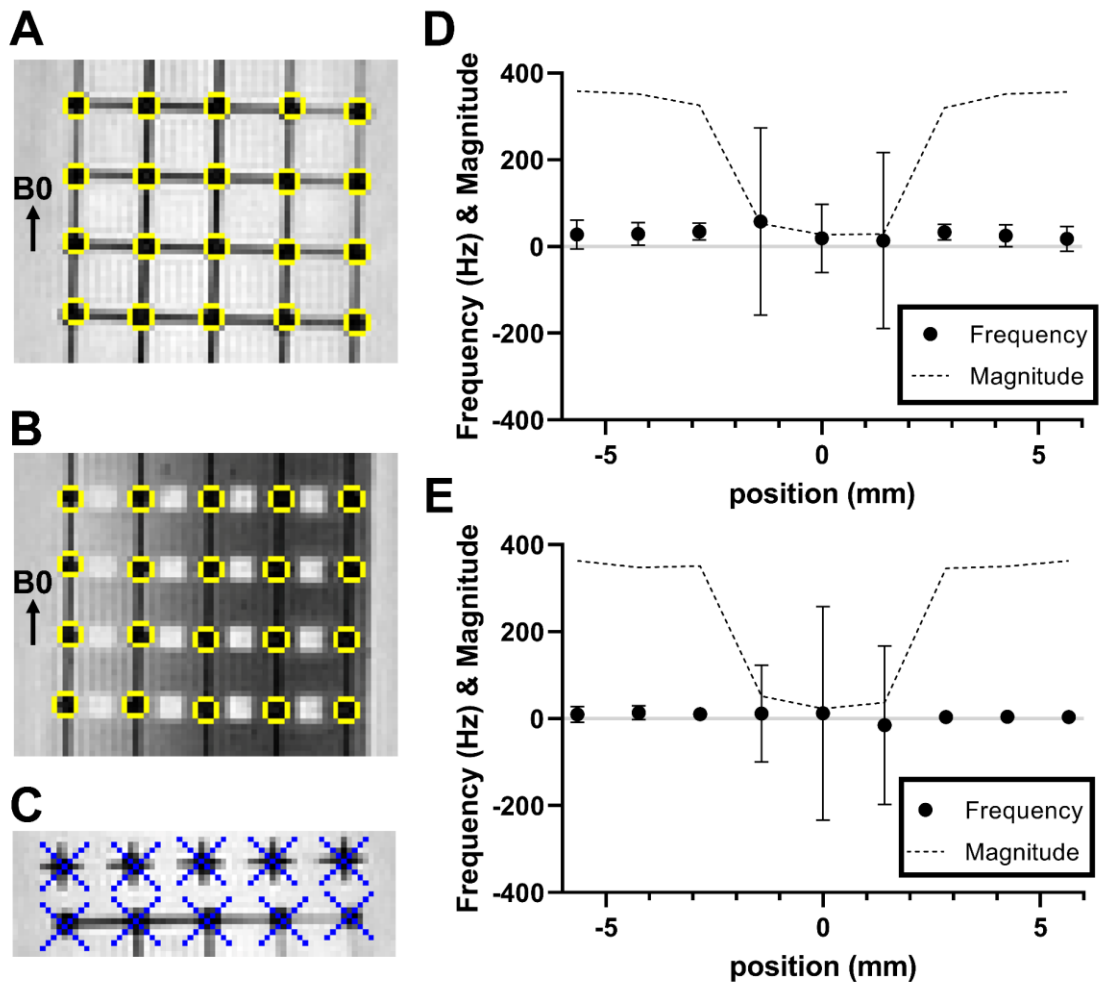


Figure 2.5: MRI compatibility analysis through field shift mapping. A) Marker beads chosen from strut-based phantom. Yellow: detected marker centroids overlaid on slice. B) Marker beads chosen from wall-based phantom. C) Line profiles centered on detected marker centroids; lines are diagonal and in the axial plane to avoid crossing supporting structures. Only 5 of the 20 beads used in averaging from each phantom shown. D) Average frequency shift surrounding marker beads in the strut-based phantom; the three central voxels are within the marker, thus having low signal and noisy phase measurements. E) Average frequency shift surrounding marker beads in the wall-based phantom.

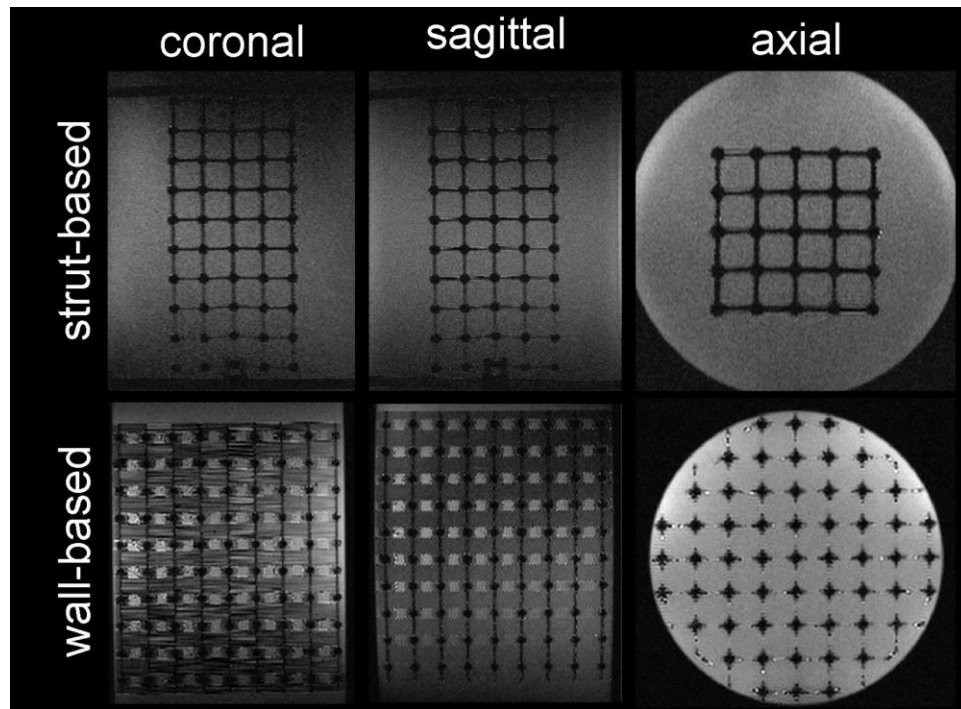


Figure 2.6: 3D magnitude images analyzed for MR image distortion

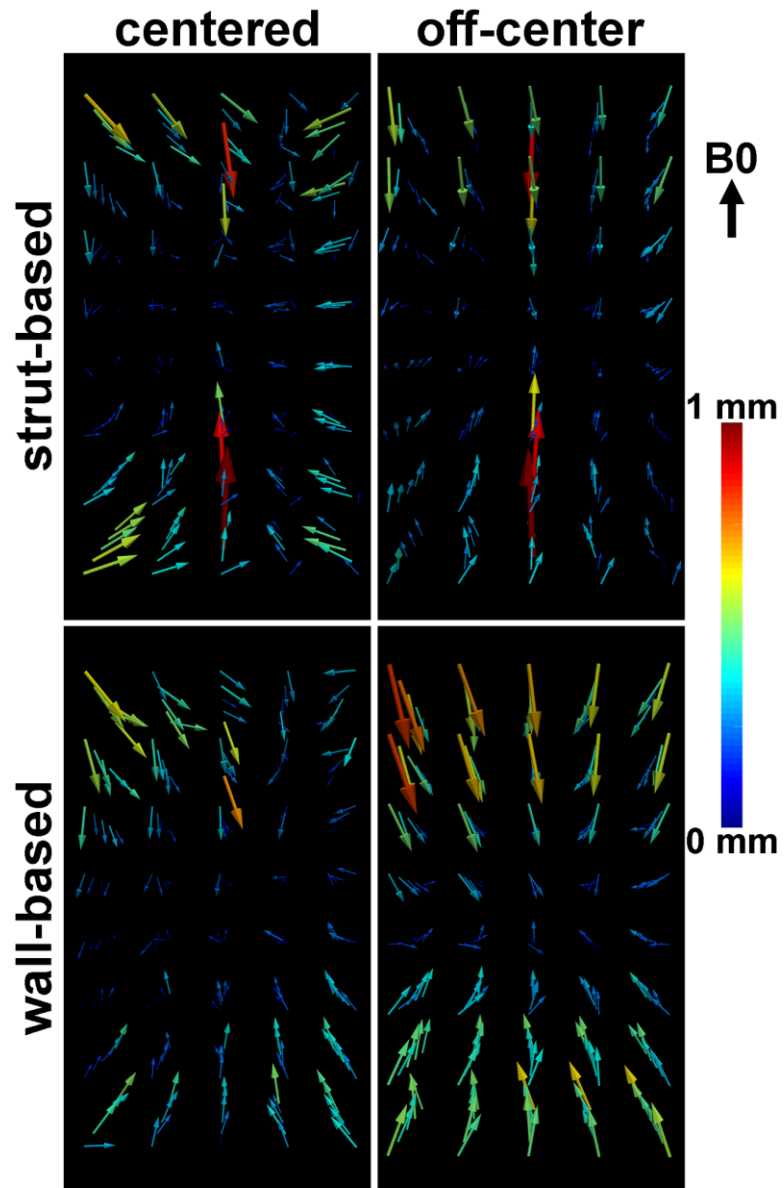


Figure 2.7: Marker deviations in MRI at isocenter and 10 cm off-center. Both phantoms are cropped to a matching set of 5x5x8 marker beads. Warping from the holder contributes to the abnormal deviations in the central column of the strut-based deviation maps.

2.3.3 Susceptibility-Induced Distortion

Encapsulating a hip implant within the wall-based phantom allowed for the observation of both through-plane and in-plane distortion. The axial 2D images (Figure 2.8)

demonstrate the ability to visualize through-plane distortion surrounding the cobalt-chrome femoral head by imaging slices in alternating marker and non-marker planes. The phantom also facilitates evaluation of in-plane distortion surrounding the implant; this distortion is particularly evident in regions of both high off-resonance and high signal, such as in slices 6-9 of Figure 2.8. A 3D acquisition surrounding the titanium stem (with the higher susceptibility femoral head removed) demonstrates the ability to calculate the marker centroids using a similar binary erosion scheme to the automated analysis used on the full phantom (Figure 2.9A). The centroids are then compared to their known nominal location to generate a distortion map (Figure 2.9B) that indicates the displacement of the marker in the image. As expected, the region surrounding the bulkier part of the stem (where it attaches to the head) has substantially more artifact and distortion than the cylindrical portion that inserts into the femur; the mean marker displacement in the top 3 rows is 3.77 ± 0.72 mm while the bottom 3 rows are only displaced 0.24 ± 0.19 mm.

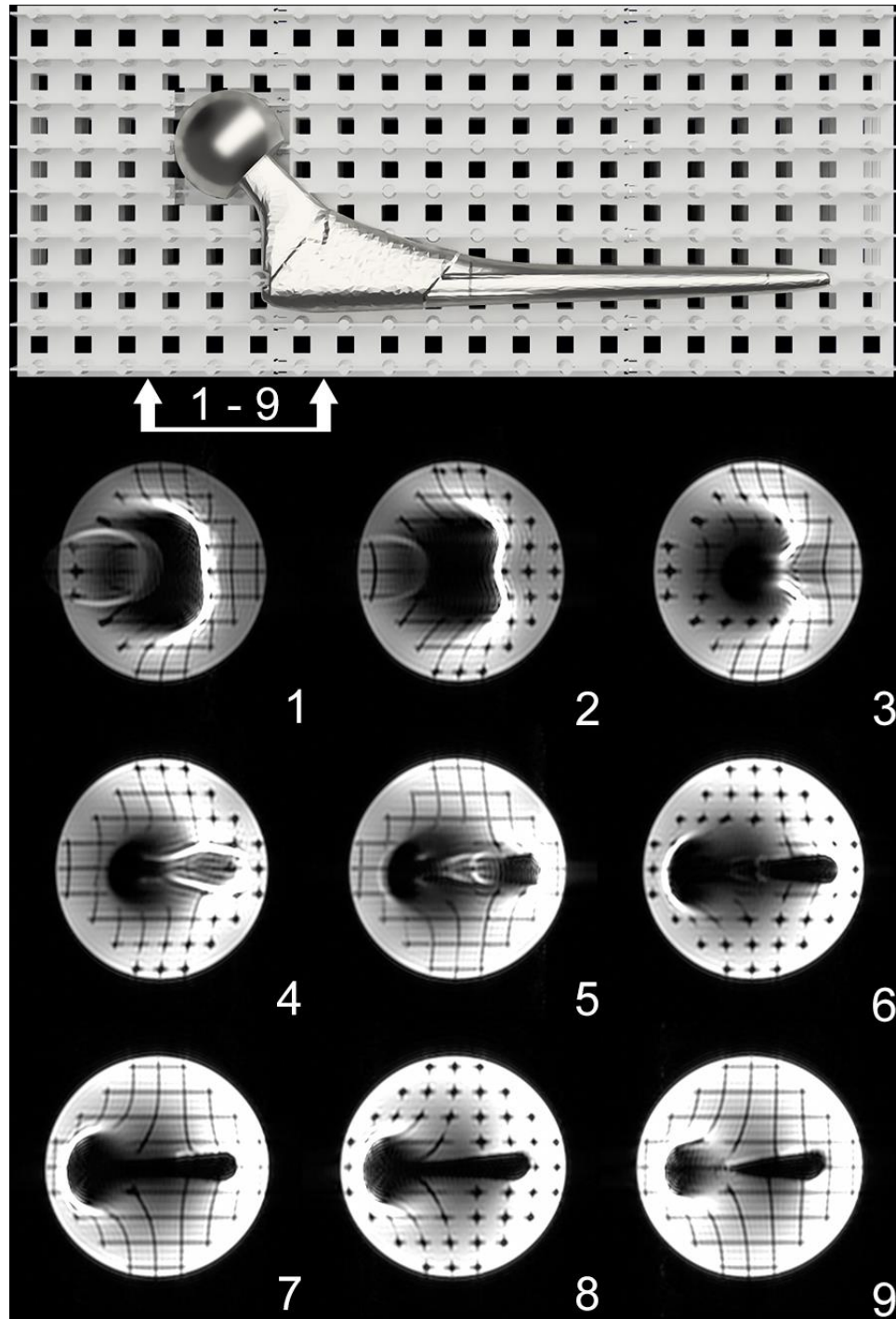


Figure 2.8: Large image distortions in axial 2D fast spin echo images surrounding a hip implant. Slices are 3 mm thick with 3.5 mm spacing; through-plane distortions are observed through the presence or absence of markers and in-plane distortion is evident by irregular spacing of markers.

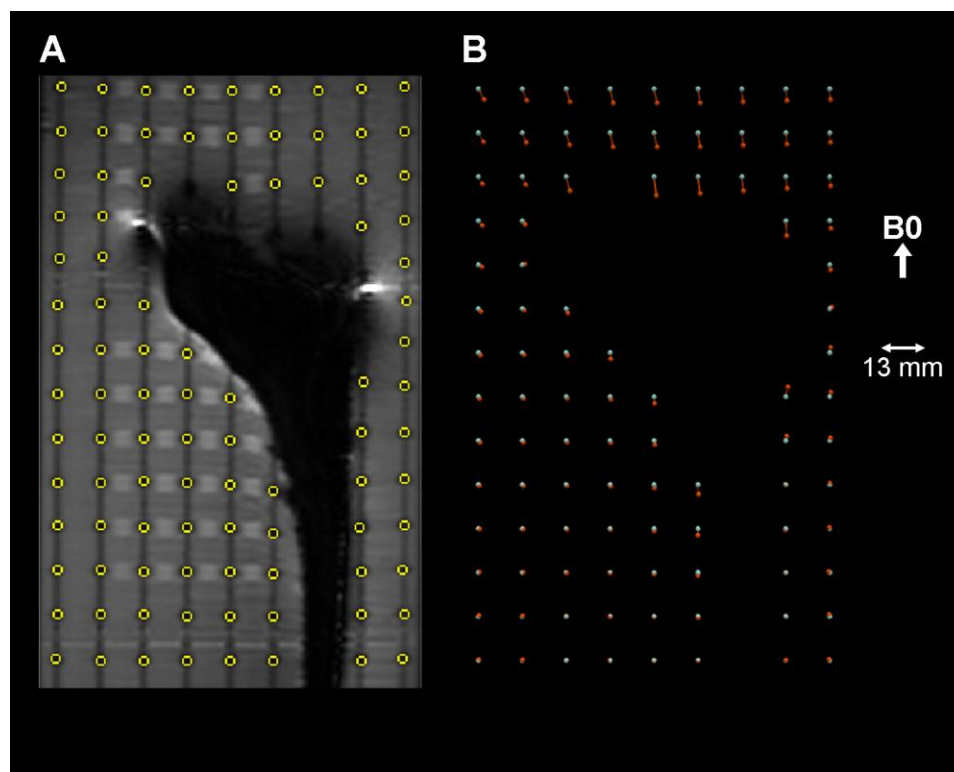


Figure 2.9: Quantitative analysis of susceptibility induced distortion in a 3D acquisition surrounding a titanium hip stem. A) Detected marker beads; spherical markers are differentiated from other signal voids based on size and roundness. B) Deviation map from detected marker beads; white ball shows expected location and red ball indicates location in image.

2.4 Discussion

3D-printing enables customized and repeatable fabrication of an array of spherical markers and an accompanying supporting structure. We explored two support designs tailored to two different 3D-printing techniques; a strut-based support system for fabrication with printers that allow unsupported horizontal constructs, and a wall-based support system for fused-deposition modelling, which is ubiquitous and inexpensive but requires vertical supports to fabricate. The fabricated constructs' dimensional fidelity, considering both fabrication errors and the changes due to water uptake when submerged, were studied. The strut phantom is more accurately fabricated but suffers from a larger dimensional change from submersion than the wall-based phantom, while absorbing less

water. The strut-based phantom is also more susceptible to mechanical deformation, as the holder caused a small but detectable physical displacement of the central markers directly adjacent to the holder connection. The wall-based phantom design is also amenable to customization as it is mechanically stiff, enabling the walls to act as a supporting structure for any embedded insert, and inexpensive to fabricate due to its compatibility with FDM. We also have demonstrated a design for modularization of the wall-based phantom, which may potentially be extended to create larger phantoms as needed.

Another important consideration for a distortion phantom is ensuring that the magnetic susceptibility difference between the phantom and its surrounding solution must be small enough to avoid self-induced distortion in the acquired image. To measure this effect, we calculated the field shift in each voxel based on the differential accrual of phase over two different echo times. The results show that the volume surrounding the marker bead shows minimal change, even in the voxels adjacent to the perimeter of the sphere; a similar process was used by Frohwein et al.²⁸ to verify the susceptibility of their distortion phantom, which was similarly printed on a Stratasys Objet printer using a Vero series photopolymer and found that the photopolymer does not have substantial susceptibility differences with water, corroborating our findings. This indicates that the plastics' susceptibility is not a factor in inducing geometric distortion, thus any control point deviation in MR images is due to field inhomogeneity from other sources. Between the two tested materials, it was found that PLA has a marginally smaller susceptibility effect than the Veroclear resin, likely as a result of the substantial difference in water uptake; as the fluid permeates the wall-based phantom's PLA, the change in susceptibility difference becomes gradual, as opposed to abrupt, which reduces the overall effect on field homogeneity. The biggest susceptibility-related challenge is the removal of air from the phantom; this was achieved by adding surfactant to the saline solution and evacuation in a vacuum chamber. The phantom also needs to have 100% infill, as air trapped within the beads could cause distortion of its surroundings; this was the default setting for the resin printer but needs to be specified for FDM.

Marker deviation analysis was done using a custom software process that automates the analysis of control point deviation throughout the phantom, which opens the possibility of routine use of this phantom design as a part of clinical quality assurance. The information derived from our 3D map of control point deviation has potential for use in image validation and correction, which is a critical part of image-guided procedures. It is expected that geometric distortions increase with distance from the main field isocenter due to field inhomogeneity. Other distortion phantoms have demonstrated this property,²⁰ and both phantoms in this study show a significant linear increase in centroid deviation magnitude in markers further from the central plane. The strut-based phantom also suffered small mechanical deformations from the holder, which can be seen in the central column of the outer edges of the deviation map. By surrounding a test object, like a hip implant, with marker beads, the phantom can also be used for analyzing susceptibility artifacts, particularly geometric distortions arising from high-susceptibility objects such as metals. We have demonstrated the phantom's capacity to aid in visualizing both in-plane and through-plane distortion simultaneously in 2D acquisitions and the ability to quantify field inhomogeneity-induced signal misplacement. As most phantoms for evaluation of metal artifacts have no geometric features or consist of simple, 2D grids, the wall-based phantom provides a novel means to evaluate metal artifacts, which will lead to improved understanding and ultimately aiding the development of artifact reduction around metal.

Several other techniques to characterize MRI geometric distortion have been proposed, primarily consisting of fiducial markers in a grid arrangement with known spacing. These phantoms usually consist of one of two styles: a rectangular grid using row and column intersections as markers,^{15,16} or a solid construct containing a distribution of spherical cavities filled with signal generating fluid.¹⁸⁻²⁰ The more readily observed fiducial control points presented by spherical markers allows for simpler analysis of image distortion, however a structure composed of regular grids is much simpler to manufacture. 3D-printing has previously been explored for fabricating distortion phantoms^{27,28} and is appealing compared to traditional manufacturing because it is inexpensive, quick and does not require a machinist. In this work, we designed and demonstrated a phantom that combines the simplicity of grid intersections with the functionality of signal generating

marker beads found in more complicated designs. This combination is achieved by placing solid beads at the intersection of a thin supporting grid; the beads are differentiable from the supports by size, allowing morphological erosion to remove the supports and leaving a cloud of fiducial markers that are readily analyzed in a manner similar to signal generating marker beads.

Our phantom design has a few limitations, particularly compared to phantom designs with signal generating markers. First is the difficulty in thorough removal of air from the phantom; prolonged evacuation in a vacuum chamber is typically adequate but trapped air bubbles can only be detected through scanning. Submerging the phantom in liquid also necessitates a water-tight container and results in a heavier assembly, which may limit the useful size of the phantom. There are also trade-offs between the strut-based and wall-based designs; mainly, the strut-based phantom has better fabrication accuracy but with a higher cost, worse structural rigidity, and slightly worse susceptibility. Analysis of the implant embedded phantom was difficult to fully automate, due to the unpredictable signal voids; while it is possible to identify markers by shape and size, we needed to specify which markers were removed (to accommodate the implant) or undetected. The design of the cavity for the implant also requires planning in order to be compatible with FDM 3D-printing, the main limitation being the requirement for vertical support.

The customizability of this phantom design leaves considerable room for further applications. As MRI in image guided therapy becomes more popular, a simple means to map or verify image distortion from main field inhomogeneity increases in demand. We have demonstrated a phantom tailored for visualizing and evaluating metal artifacts with the ability to view through-plane distortion along multiple orientations. Future uses of the include correlating distortion with acquisition parameters, particularly readout bandwidth, and to evaluate reduction techniques for a variety of implant shapes. The erosion and centroid-based analysis and resulting knowledge of marker displacement can also be used for image co-registration; this also provides information about phantom orientation within the scanner.

In conclusion, our distortion phantoms have many useful properties: it is simple and inexpensive to fabricate accurately, is amenable to automated distortion map generation from magnitude images and uses materials with similar magnetic susceptibility to water. Furthermore, while we have demonstrated one application of this phantom in evaluating metal artifacts, with the flexibility offered by our design and the utility of 3D-printing we hope to find additional applications for our phantom by inserting cavities in which we can embed objects that would simulate clinical conditions. Quantitative MR distortion data could aid development of distortion correction, leading to improved clinical applications in image guidance.

2.5 References

1. Aubry JF, Cheung J, Morin O, Beaulieu L, Hsu IC, Pouliot J. Investigation of geometric distortions on magnetic resonance and cone beam computed tomography images used for planning and verification of high-dose rate brachytherapy cervical cancer treatment. *Brachytherapy* 2010;9(3):266-273.
2. Crijns SP, Bakker CJ, Seevinck PR, de Leeuw H, Lagendijk JJ, Raaymakers BW. Towards inherently distortion-free MR images for image-guided radiotherapy on an MRI accelerator. *Phys Med Biol* 2012;57(5):1349-1358.
3. Weygand J, Fuller CD, Ibbott GS, Mohamed AS, Ding Y, Yang J, Hwang KP, Wang J. Spatial precision in magnetic resonance imaging-guided radiation therapy: The role of geometric distortion. *Int J Radiat Oncol Biol Phys* 2016;95(4):1304-1316.
4. Maikusa N, Yamashita F, Tanaka K, Abe O, Kawaguchi A, Kabasawa H, Chiba S, Kasahara A, Kobayashi N, Yuasa T, Sato N, Matsuda H, Iwatsubo T. Improved volumetric measurement of brain structure with a distortion correction procedure using an adni phantom. *Med Phys* 2013;40(6):062303.
5. Schneider E, Nassaiver M. The osteoarthritis initiative (oai) magnetic resonance imaging quality assurance update. *Osteoarthritis Cartilage* 2013;21(1):110-116.
6. Eagle S, Potter HG, Koff MF. Morphologic and quantitative magnetic resonance imaging of knee articular cartilage for the assessment of post-traumatic osteoarthritis. *J Orthop Res* 2017;35(3):412-423.
7. Krishnan SP, Dawood A, Richards R, Henckel J, Hart AJ. A review of rapid prototyped surgical guides for patient-specific total knee replacement. *J Bone Joint Surg Br* 2012;94(11):1457-1461.
8. Schotanus MGM, Thijs E, Heijmans M, Vos R, Kort NP. Favourable alignment outcomes with MRI-based patient-specific instruments in total knee arthroplasty. *Knee Surg Sports Traumatol Arthrosc* 2018;26(9):2659-2668.
9. Chen CC, Wan YL, Wai YY, Liu HL. Quality assurance of clinical MRI scanners using acr MRI phantom: Preliminary results. *J Digit Imaging* 2004;17(4):279-284.
10. Ihalainen TM, Lonroth NT, Peltonen JI, Uusi-Simola JK, Timonen MH, Kuusela LJ, Savolainen SE, Sipila OE. MRI quality assurance using the acr phantom in a multi-unit imaging center. *Acta Oncol* 2011;50(6):966-972.
11. Panych LP, Chiou JY, Qin L, Kimbrell VL, Bussolari L, Mulkern RV. On replacing the manual measurement of acr phantom images performed by MRI technologists with an automated measurement approach. *J Magn Reson Imaging* 2016;43(4):843-852.

12. Baldwin LN, Wachowicz K, Thomas SD, Rivest R, Fallone BG. Characterization, prediction, and correction of geometric distortion in 3T MR images. *Med Phys* 2007;34(2):388-399.
13. Smith MR, Artz NS, Wiens C, Hernando D, Reeder SB. Characterizing the limits of MRI near metallic prostheses. *Magn Reson Med* 2015;74(6):1564-1573.
14. Tanner SF, Finnigan DJ, Khoo VS, Mayles P, Dearnaley DP, Leach MO. Radiotherapy planning of the pelvis using distortion corrected MR images: The removal of system distortions. *Phys Med Biol* 2000;45(8):2117-2132.
15. Mizowaki T, Nagata Y, Okajima K, Kokubo M, Negoro Y, Araki N, Hiraoka M. Reproducibility of geometric distortion in magnetic resonance imaging based on phantom studies. *Radiother Oncol* 2000;57(2):237-242.
16. Wang D, Doddrell DM, Cowin G. A novel phantom and method for comprehensive 3-dimensional measurement and correction of geometric distortion in magnetic resonance imaging. *Magn Reson Imaging* 2004;22(4):529-542.
17. Caramanos Z, Fonov VS, Francis SJ, Narayanan S, Pike GB, Collins DL, Arnold DL. Gradient distortions in MRI: Characterizing and correcting for their effects on siena-generated measures of brain volume change. *Neuroimage* 2010;49(2):1601-1611.
18. Pappas EP, Seimenis I, Moutsatsos A, Georgiou E, Nomikos P, Karaiskos P. Characterization of system-related geometric distortions in MR images employed in gamma knife radiosurgery applications. *Phys Med Biol* 2016;61(19):6993-7011.
19. Huang KC, Cao Y, Baharom U, Balter JM. Phantom-based characterization of distortion on a magnetic resonance imaging simulator for radiation oncology. *Phys Med Biol* 2016;61(2):774-790.
20. Torfeh T, Hammoud R, Perkins G, McGarry M, Aouadi S, Celik A, Hwang KP, Stancanello J, Petric P, Al-Hammadi N. Characterization of 3D geometric distortion of magnetic resonance imaging scanners commissioned for radiation therapy planning. *Magn Reson Imaging* 2016;34(5):645-653.
21. Koch KM, Brau AC, Chen W, Gold GE, Hargreaves BA, Koff M, McKinnon GC, Potter HG, King KF. Imaging near metal with a mavric-semac hybrid. *Magn Reson Med* 2011;65(1):71-82.
22. den Harder JC, van Yperen GH, Blume UA, Bos C. Ripple artifact reduction using slice overlap in slice encoding for metal artifact correction. *Magn Reson Med* 2015;73(1):318-324.

23. Fritz J, Ahlawat S, Demehri S, Thawait GK, Raithel E, Gilson WD, Nittka M. Compressed sensing semac: 8-fold accelerated high resolution metal artifact reduction MRI of cobalt-chromium knee arthroplasty implants. *Invest Radiol* 2016;51(10):666-676.
24. van Gorp JS, Nizak R, Bouwman JG, Saris DB, Seevinck PR. Multispectral 3D phase-encoded turbo spin-echo for imaging near metal: Limitations and possibilities demonstrated by simulations and phantom experiments. *Magn Reson Imaging* 2017;39:31-43.
25. Wiens CN, Artz NS, Jang H, McMillan AB, Koch KM, Reeder SB. Fully phase-encoded MRI near metallic implants using ultrashort echo times and broadband excitation. *Magn Reson Med* 2018;79(4):2156-2163.
26. Koff MF, Shah P, Koch KM, Potter HG. Quantifying image distortion of orthopedic materials in magnetic resonance imaging. *J Magn Reson Imaging* 2013;38(3):610-618.
27. Kittle D, Holshouser B, Slater JM, Guenther BD, Pitsianis NP, Pearlstein RD. Technical note: Rapid prototyping of 3D grid arrays for image guided therapy quality assurance. *Med Phys* 2008;35(12):5708-5712.
28. Frohwein LJ, Hoerr V, Faber C, Schafers KP. Correction of MRI-induced geometric distortions in whole-body small animal PET-MRI. *Med Phys* 2015;42(7):3848-3858.
29. Rai R, Wang YF, Manton D, Dong B, Deshpande S, Liney GP. Development of multi-purpose 3D printed phantoms for MRI. *Phys Med Biol* 2019;64(7):075010.
30. Mangione S, Acquaviva R, Garbo G. A fully automated method for accurate measurement of geometrical distortion in magnetic resonance imaging of a 3D-lattice phantom. *Magn Reson Imaging* 2019;57:8-18.
31. Holdsworth DW, Teeter MG, Milner JS, Pollmann SI, Drangova M. 3D-printed geometric distortion correction phantom for MRI. Conference proceedings from the Joint Annual Meeting ISMRM-ESMRMB 2014; Milan.
32. Holdsworth DW, Teeter MG, Milner JS, Pollmann SI, Drangova M; Method and apparatus for measuring 3D geometric distortion in MRI and CT images with a 3D physical phantom US patent 10,557,911. 2020 February 11, 2020.
33. Schenck JF. The role of magnetic susceptibility in magnetic resonance imaging: Mri magnetic compatibility of the first and second kinds. *Med Phys* 1996;23(6):815-850.
34. Och JG, Clarke GD, Sobol WT, Rosen CW, Mun SK. Acceptance testing of magnetic resonance imaging systems: Report of aapm nuclear magnetic resonance task group no. 6. *Med Phys* 1992;19(1):217-229.

35. Styner M, Brechbuhler C, Szekely G, Gerig G. Parametric estimate of intensity inhomogeneities applied to MRI. *IEEE Trans Med Imaging* 2000;19(3):153-165.
36. Bernstein MA, Grgic M, Brosnan TJ, Pelc NJ. Reconstructions of phase contrast, phased array multicoil data. *Magn Reson Med* 1994;32(3):330-334.
37. Hong G, Liu J, Cobos SF, Khazaei T, Drangova M, Holdsworth DW. Effective magnetic susceptibility of 3D-printed porous metal scaffolds. *Magn Reson Med* 2022;87(6):2947-2956.

Chapter 3

3 Effective Magnetic Susceptibility of 3D-Printed Porous Metal Scaffolds

3.1 Introduction

Many common orthopedic procedures, including knee arthroplasty, hip replacement and spinal fusion, involve implantation of metal components.¹⁻³ MRI has been found to be an effective means of detecting complications related to these implants, but suffers from severe artifacts due to the high magnetic susceptibility of metal.⁴⁻⁷ To mitigate the effects of metal implants on local B₀ inhomogeneity, spin-echo sequences as well as specialized multispectral acquisitions^{8,9} – with correspondingly longer scan times – have been used to reduce signal void volume. Simultaneously, high readout bandwidths are required to reduce geometric distortion but result in lower signal-to-noise ratio. Because the artifact severity is directly related to an implant's magnetic susceptibility, image quality will be inherently improved if the susceptibility of the implant is lowered.¹⁰

Recent developments in advanced fabrication with metal 3D printing have allowed the manufacturing of a variety of geometries that would be impossible for traditional metalworking. Metal 3D printing has facilitated the fabrication of porous cellular scaffolds for orthopedic implants, which have been shown to have the potential to reduce stress shielding and thus reduce bone loss.¹¹⁻¹³ Porous metal implants have also been shown to exhibit excellent osseointegration,¹⁴⁻¹⁶ demonstrated *in vivo* by porous 3D-printed titanium interbody fusion cages in animal models¹⁷ and initial patient trials.^{18,19} The feasibility of using MRI to monitor bone apposition and implant fixation into the porous coating of a 3D printed acetabular shell was also recently demonstrated.²⁰

An important feature of 3D-printed porous metal structures is their lower density – and hence lower magnetic susceptibility – compared to that of solid metal implants. Low-susceptibility porous 3D metal scaffolds could lead to exciting implant designs that do

not require the use of dedicated multispectral artifact reduction sequences to produce diagnostically valuable images, simplifying and improving the monitoring of any complications around the implant. Recently, Carter et al.,²¹ reported the linear decrease of signal void volume with decreasing density for octahedral, diamond, and honeycomb structures. However, they did not directly quantify the relationship between the metal-sample density and the effective magnetic susceptibility.

We aim to quantify the relationship between the effective (volume-averaged) susceptibility and the porosity/density of 3D-printed porous scaffolds, which will facilitate the optimization of porous metal scaffold and implant-design strategies. Specifically, we selected to evaluate the sheet-based gyroid²² as the scaffold shape, because of its strong potential to be used in orthopedic implant design, given its bone-mimicking mechanical properties.²³ For the determination of the effective magnetic susceptibility of 3D-printed metal gyroids we describe a modification of the method developed by Perkins et al.,²⁴ which estimated the effective magnetic susceptibility through comparing acquired to simulated field maps surrounding printed magnetic ink patterns. The extension of Perkins' method to 3D, which required the fabrication of precise alignment phantom for the gyroid samples, is described, along with the results of the study evaluating the effective susceptibility of Ti 3D printed gyroids with varying porosity.

3.2 Methods

3.2.1 Gyroid-Based Porous Metal Scaffold Samples

The sheet-based gyroid²² is a triply periodic minimal surface that has been studied as the basis of scaffolds for tissue engineering and bone-mimicking applications and has been shown to have favorable mechanical properties, such as reduced stress concentration and an apparent compressive modulus similar to trabecular bone.²³ Following the geometry described by Schoen,²² gyroid scaffolds were modeled using Blender (Version 2.79, blender.org, Amsterdam, Netherlands), with a specific geometry based on a 6 mm³ unit cell arranged into a 3x3x8 array, subsequently truncated by a cylinder of 17 mm diameter

and 40 mm length, as shown in Figure 3.1A. Five cylindrical gyroid samples of nominal porosity ranging from 60 to 90% were generated by changing the gyroid's wall thickness from 0.2 to 0.8 mm, respectively (Figure 3.1B); a solid cylindrical sample with the same dimensions was also generated. Note that for this study “porosity” is defined as the metal-void volume fraction, i.e.

$$\textit{nominal porosity} = \left(1 - \frac{\textit{gyroid volume}}{\textit{cylinder volume}}\right) * 100\% \quad (3.1)$$

The models were exported from Blender as STL (stereolithography) files and sliced using the QuantAM build preparation software (Renishaw plc, Wotton-under-Edge, UK). The structures were 3D printed in Ti6Al4V medical grade titanium alloy (Ti6Al4V ELI-0406, Renishaw plc; particle size 15-45 μm) using laser powder-bed fusion (AM400, Renishaw plc) at ADEISS (London, Canada). The laser spot diameter was 70 μm and layer thickness was 40 μm . As part of routine quality control, the printed density of the titanium alloy was verified by printing a standard test object simultaneously with the samples; printed density was determined from this test object using hydrostatic weighing and subsequently used to calculate the expected mass of the solid cylindrical sample. The achieved porosity of each porous cylinder, which is often different from the designed porosity due to microscopic pores in the walls and overhanging materials at the edges,²³ was determined by weighing each printed gyroid sample using a high precision scale (BP3100P, Sartorius, Göttingen, Germany, 0.01 g accuracy) and comparing the mass to that of the solid cylinder, i.e.

$$\textit{achieved porosity} = \left(1 - \frac{\textit{scaffold mass}}{\textit{solid mass}}\right) * 100\% \quad (3.2)$$

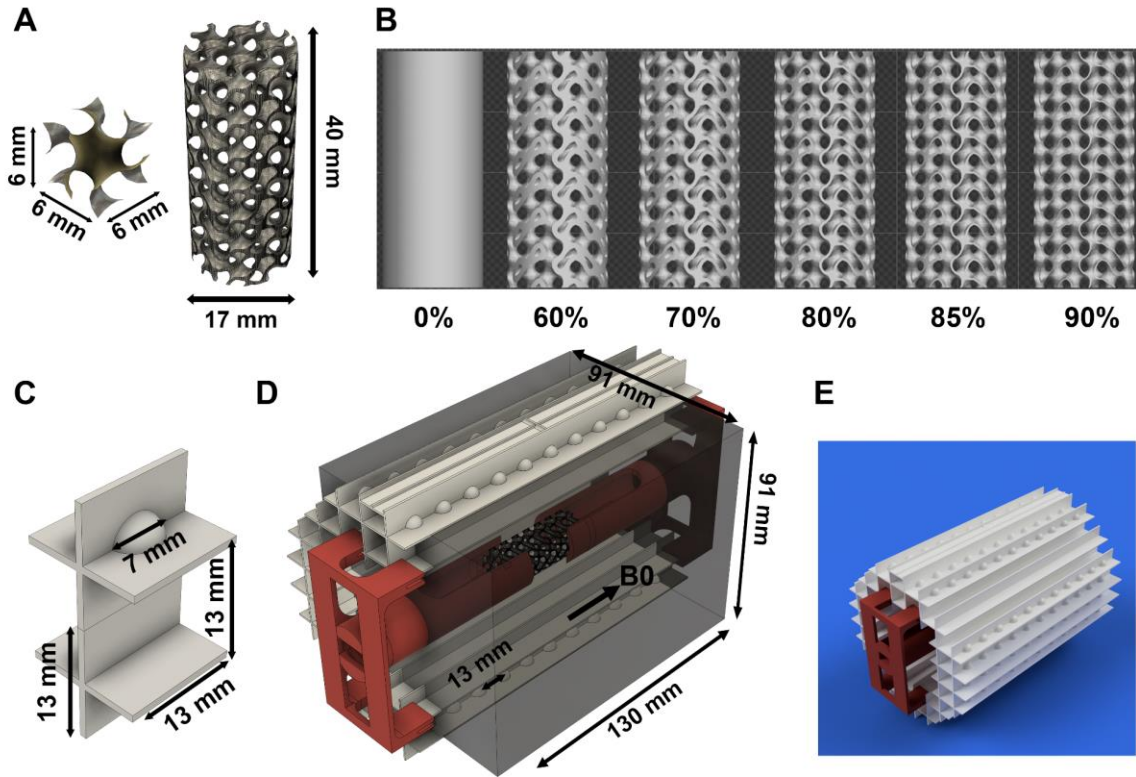


Figure 3.1: Gyroid-based scaffold and alignment phantom design. (A) Example of a gyroid surface unit cell and cylinder model. (B) Renderings of the set of cylindrical samples of varying nominal porosity (%) generated by varying wall thickness (C) Marker bead and supporting wall structure. (D) Rendering of the alignment phantom, cut to demonstrate the position of a 3D-printed cylinder within the custom holder (red). A grid of uniformly spaced marker beads is incorporated to enable reproducible alignment of acquired images to simulated field maps. The transparent grey box identifies the volume of interest used in the study. (E) Rendering of the whole phantom

3.2.2 Alignment Phantom

For accurate B_0 simulations that match scan conditions, precise knowledge of the location and orientation of the printed sample within the scanner is required. Precise alignment of simulated and scanned images was achieved through a custom phantom whose geometry was designed to provide orientation information.²⁵ The phantom was a 3D-printed plastic (polylactic acid) structure surrounding the printed metal sample. Registration beads (7 mm, Figure 3.1C) were embedded, at 13 mm centers, along the

phantom walls, forming a virtual rectangular volume (91x91x130 mm, Figure 3.1D) centered on the metal sample, which was held in place with a custom holder. The assembled alignment phantom was submerged in copper sulfate saline solution²⁶ (0.008 mol/L CuSO₄; used to mimic tissue conductivity without substantial change to susceptibility²⁷) within a sealed acrylic cylinder. The STL files for the alignment phantom and sample holder are available on GrabCAD (<https://grabcad.com/library/alignment-phantom-for-MRI-1>).

3.2.3 Imaging

Two sets of coronal scans²⁴ of the submerged “grid” phantom were acquired on a GE Discovery MR750 3T scanner (GE Healthcare, Waukesha, WI) using the birdcage head coil. Images were acquired using a 3D GRE sequence with echo times 0.5 ms apart, (256x128x128 matrix; 25.6 cm FOV, 1 mm slice thickness; TE = 3, 3.5 ms; TR = 15 ms, 10° flip angle, 125 kHz BW), ultimately yielding field maps with a ± 1 kHz bandwidth. A second scan, without the test object, enabled background field correction.

3.2.4 Bead identification and Volume of Interest (VOI)

The 3D magnitude images from the first-echo scan of the grid phantom were used to generate a binary mask of the marker beads by first blanking the central volume, which contained the image of the metal sample and associated artifacts, and thresholding the image. The marker beads were identified using thresholding and their centroids calculated, enabling the definition of a 91x91x130 mm VOI centered on the gyroid samples. All images used in subsequent analysis were cropped to this VOI, which contains the metal sample at its center.

3.2.5 Estimation of Signal Void Volume

As a measure of metal-induced artifact, the cropped 3D magnitude images were analyzed to quantify the size of the signal-void region surrounding each sample, calculated as the number of voxels with intensity values below a selected threshold value. This threshold

value was determined by generating an intensity histogram and applying Otsu's method, as shown in Figure 3.2.²⁸

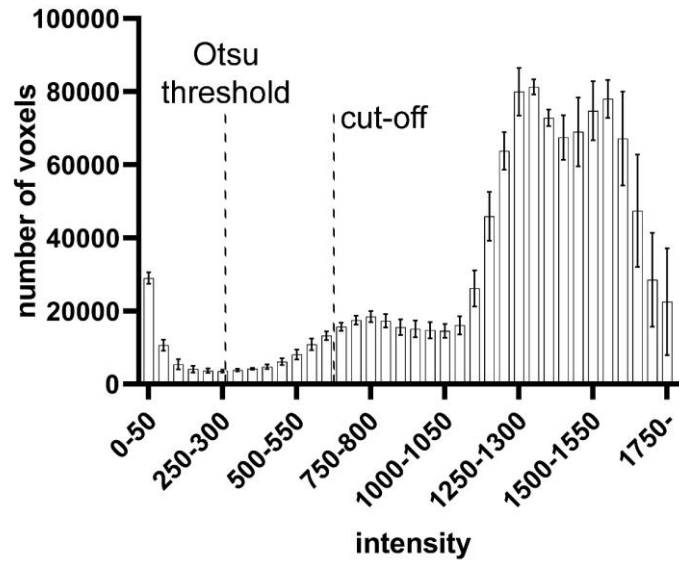


Figure 3.2: Histogram (bin width = 50, range = 0 to 1800) used to determine the binary threshold (271) used for signal void analysis. As the voxel intensities exhibit a multimodal distribution, the full histogram was truncated at 650 (as this cut-off value maximizes the effectiveness metric of the resulting threshold) prior to using Otsu's method.

3.2.6 Estimation of Effective Magnetic Susceptibility

3.2.6.1 B₀ determination

Phase images were corrected for background field inhomogeneity, then used to generate a field map by calculating the Hermitian product to determine the phase accumulation between the two echo times; phase unwrapping was achieved using PUROR, a fast intervention-based phase unwrapping algorithm.²⁹ While B₀ maps were calculated over the entire 3D images, prior to comparison to simulated B₀s, data were cropped to the VOI centered on the metal sample.

3.2.6.2 Field map simulation and susceptibility estimation

To estimate effective susceptibility, simulated field maps of solid cylinders (17 mm diameter; 40 mm length) of uniform magnetic susceptibility were generated using Bouwman and Bakker's Fourier-based calculation of the susceptibility induced perturbation of the magnetic field³⁰ with $(0.5 \text{ mm})^3$ resolution. The cylinder models were assigned susceptibility values ranging from -9 ppm (water with no metal) to 182 ppm (solid titanium alloy)^{31,32} at 1 ppm increments. Matlab (Mathworks, Natick, MA) was used to rotate the analytically generated cylinders to match the scan orientation through co-registration of the alignment-phantom marker beads to their known configuration using the iterative closest point algorithm.

For each metal sample with different porosity, the effective susceptibility was estimated by minimizing the root-mean-squared error (RMSE) between 65-mm long central-line profiles of the scanned volume and registered field maps simulated with different susceptibilities. A central line profile was used for the minimization, as it is the location least vulnerable to errors due to orientation and magnet inhomogeneity (note, values from the middle 22 mm were not used in the minimization due to erroneous phase measurements stemming from lack of signal). A detailed flowchart of this data processing pipeline is available in Figure 3.3.

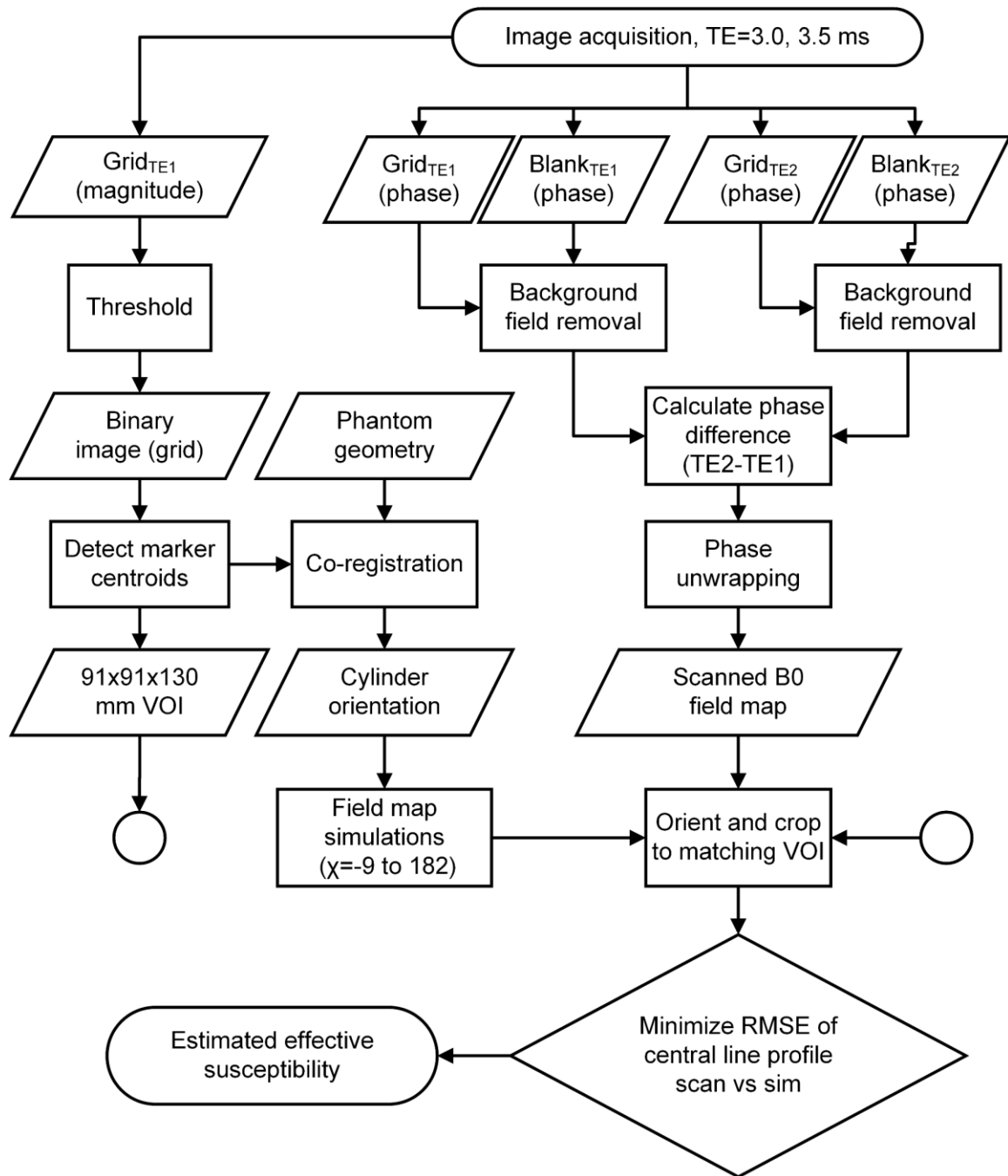


Figure 3.3: Flowchart used to estimate the effective susceptibility of the porous metal samples

3.2.6.3 Porous cylinder simulation

To gain insight into the behavior of the field in the volume adjacent to the implant, where the solid cylinder approximation is expected to fail, field map simulations of the porous cylinders (as opposed to a solid approximation) were computed. Conversion from the STL mesh to a binary image was performed using the “mesh voxelization” function that is publicly available in the Matlab Central File Exchange. To mitigate the partial volume effect, the gyroid geometry was generated at $(0.1 \text{ mm})^3$ resolution (VOI = $910 \times 910 \times 1300$ voxels; aligned with B0). Each voxel was assigned the effective susceptibility of solid alloy calculated from 2.6.2 or the nominal susceptibility of water (-9 ppm) and the resulting simulation was compared against solid approximations assigned their respective effective susceptibilities.

3.2.7 Analysis

The relationships of the signal void volume and the effective susceptibility as a function of porosity were determined using Prism 8 (GraphPad Software, La Jolla, CA). Results are reported as means and standard deviations.

3.3 Results

3.3.1 Gyroid-Based Porous Metal Scaffolds

The set of 6 porous cylinders (nominal porosities: solid, 60%, 70%, 80%, 85%, 90%) took 7.5 hours to fabricate. The standard test object was found to have a density of 4.28 gcm^{-3} . Using this printed-titanium density and nominal porosity, the expected mass and achieved porosities were calculated and are reported along with the measured masses of all samples in Table 3.1. The mass of the solid titanium sample matched the expected mass, confirming the density of the printed titanium. However, an average underestimation of $1.5 \pm 0.2 \text{ g}$ was observed for the gyroid samples, leading to the achieved porosities being $3.7\% \pm 0.8\%$ higher than nominal.

Table 3.1: Calculation of the actual porosities based on measured vs. expected mass

Nominal Porosity (%)	Expected Mass (g)	Measured Mass (g)	Actual Porosity (%)
0	38.86*	38.86	0.00
60	15.53	13.86	64.33
70	11.60	9.89	74.55
80	7.91	6.26	83.89
85	6.02	4.51	88.39
90	4.04	2.89	92.56

*based on measured density of 3D printed

Ti = 4.28 g/cm³ and cylinder volume = 9.08 cm³

3.3.2 Phantom Alignment

The rotations and translations between the scanned and simulated VOIs are shown in Table 3.2. The measured rotations were used to align the simulations to B0, while the translations were used to align the VOIs. Field maps surrounding the plastic holders showed negligible evidence of susceptibility effects.

Table 3.2: Measured rotations (degrees) and translations (mm) based on alignment phantom. Rotations are used to find orientation of cylinder to B0 to generate simulations; translations are used to create matching VOIs between scan and simulation for analysis.

Porosity (%)	X rot. (°)	Y rot. (°)	Z rot. (°)	X trans. (mm)	Y trans. (mm)	Z trans. (mm)
0	-1.02	-0.26	0.34	0.00	2.90	1.79
60	-0.85	-0.15	-0.33	1.57	0.96	1.15
70	-0.86	-0.16	-0.76	1.76	0.05	2.25
80	-0.85	-0.15	-1.15	1.85	0.73	3.12
85	-0.82	-0.13	-1.91	2.73	2.59	2.21
90	-0.84	-0.13	-0.76	1.47	0.16	0.40
mean	-0.87	-0.16	-0.76	1.56	1.23	1.82
std. dev	0.07	0.05	0.69	0.81	1.12	0.87

3.3.3 Signal-void Volume

As expected, the magnitude images show a clear decrease in the extent of metal-related artifact with increasing porosity of the metal gyroid sample (Figure 3.4). The magnitude images also show hyperintensity artifacts at the poles of the cylinders. Compared to the signal void, the hyperintensity artifacts are minor and were not quantified. The relationship between the signal-void volume, calculated based on thresholding (Figure 3.2) and shown in Figure 3.5A, demonstrates a quadratic relationship with increasing cylinder porosity ($R^2 = .998$). The samples with highest porosities (80 and 90%) demonstrated that the signal-void volume is approximately 30% larger than the volume of the cylinder itself, compared to the solid sample where the increase is 200%.

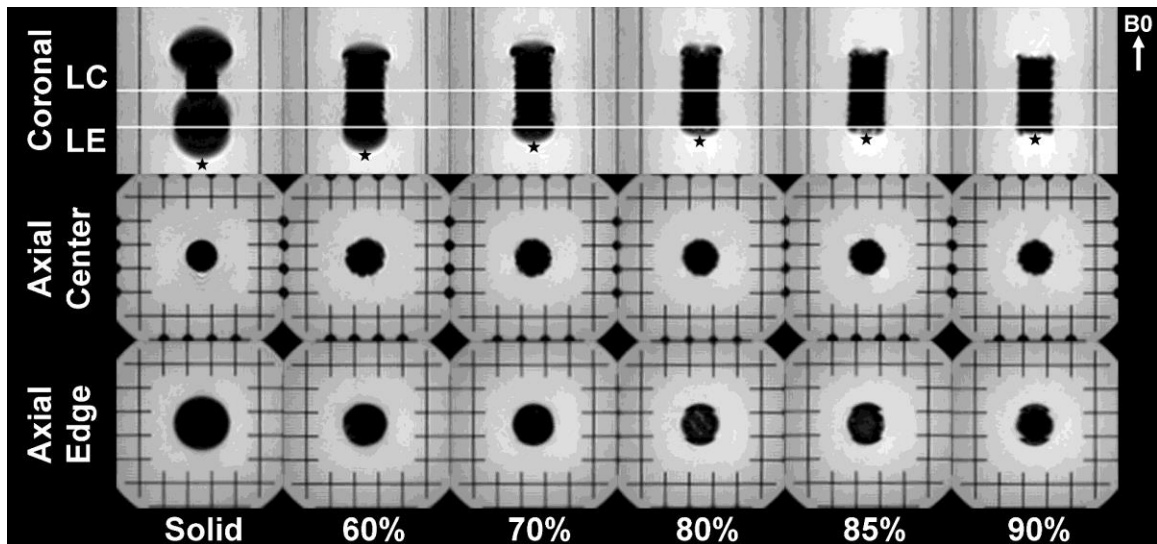


Figure 3.4: Magnitude images of central coronal slices. Axial images (sliced at LC and LE) show artifact size at the center of the cylinder (LC) and through the bottom edge (LE). Observed hyperintensity artifact is shown by ★. Bisected marker beads used for creating the VOI are visible in the axial center slices; grid intersections (spaced 13 mm apart) provide structural support and can be used as geometric landmarks.

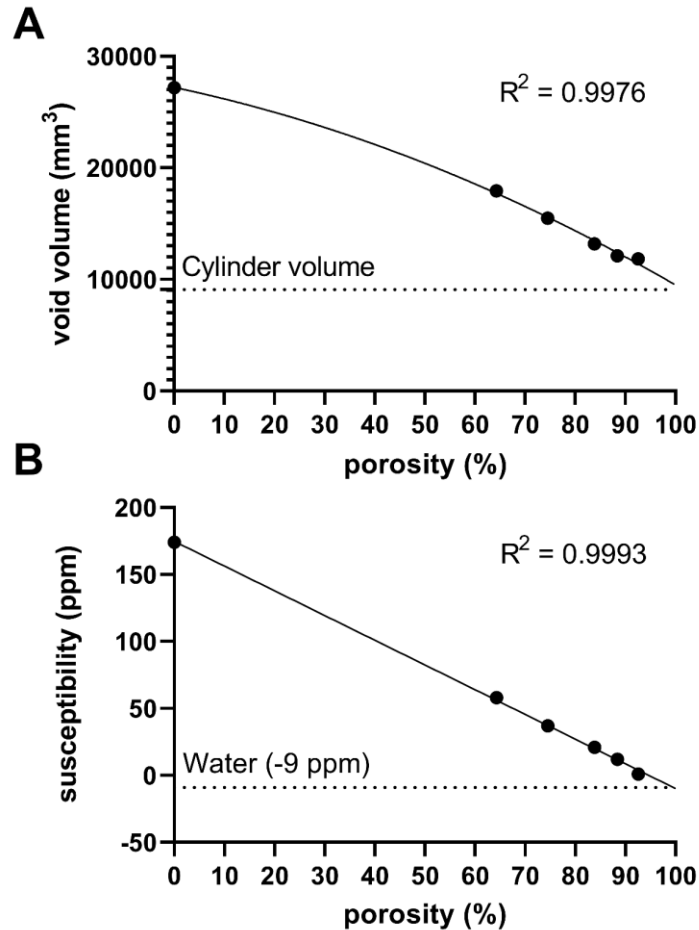


Figure 3.5: (A) Signal void volume, determined from the first echo 3D magnitude images, as a function of measured porosity. Data and quadratic fit are plotted; the extrapolated 100% porosity value is 9511 mm³, which compares well with the physical cylinder volume (9080 mm³). (B) Linear relationship between effective susceptibility estimates and porosity (slope = -1.846 ppm/% porosity, Y-intercept = 174.7 ppm). Extrapolated susceptibility at 100% porosity (no metal) is -9.9 ppm (expected: -9 ppm) and estimated susceptibility of solid cylinder is 174 ppm (expected: 176 ppm)

3.3.4 Effective Susceptibility

The estimates of effective susceptibility, shown in Figure 3.5B, demonstrate a linear relationship with increasing porosity ($R^2 = 0.999$). Extrapolation of the line of best fit to 100% porosity (i.e. no metal) yielded a magnetic susceptibility of -9.9 ppm, closely

approximating the value of pure water (-9 ppm), as expected. The 0% porosity (solid) cylinder was estimated to have a magnetic susceptibility of 174 ppm, which is close to the 176 ppm predicted by the density of the titanium test object (4.28 g/cm^3 printed vs. 4.43 g/cm^3 nominal). Aligned measured field maps are shown in Figure 3.6A; to demonstrate the minimization process, a line profile through the center of the measured B_0 for one sample is shown in Figure 3.6B along with corresponding profiles through multiple simulated field maps. The effective susceptibility values were determined as the values that provided the best match to the experimental B_0 ; profiles are shown in Figure 3.6C.

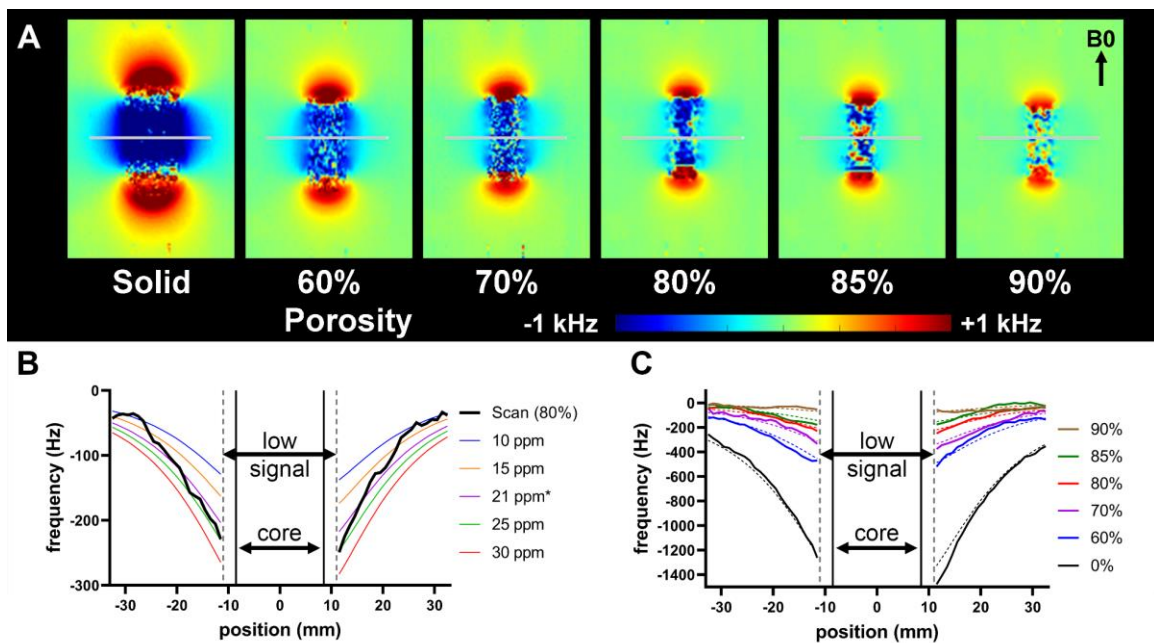


Figure 3.6: (A) Central coronal slice of the measured field maps of each porous cylinder. (B) Derivation of the effective susceptibility estimate from the 80% porosity cylinder using a central 65 mm line profile from the scanned field map compared to matching line profiles from simulations of solid cylinders of varying susceptibility. *: Susceptibility at which simulation and scan best agree. (C) Central line profiles of all measured (scanned) field maps (solid) and their matching simulation (dashed) determined by minimizing root mean square error.

3.3.5 Simulation of Porous Geometry

High resolution simulations of the gyroid-based porous geometry are shown in Figure 3.7. Consistent with the magnitude images of Figure 3.4 and measured field maps of Figure 3.6A, Figure 3.7 reveals a pattern of field perturbations that originate from the scaffold wall's edges. These are most pronounced for the lower porosity values, where the gyroid walls are thicker. Simulations of the constant susceptibility approximation (Figure 3.7A) vs the full geometry (Figure 3.7B) show substantial differences within 2 mm from the cylinder edge (Figure 3.7C; absolute frequency shift of 519 ± 617 Hz to 161 ± 263 Hz for the least and most porous cylinders, respectively) and <100 Hz in the volume outside 2 mm (Table 3.3).

Table 3.3: Average absolute frequency difference (Hz) in Figure 3.5C. The values represent the volume average of a 10 mm long cylindrical shell centered on the simulated cylinder with inner and outer diameter matching the reported distance to cylinder wall.

Distance to Cylinder Wall	Porosity 60 %	Porosity 70 %	Porosity 80 %	Porosity 85 %	Porosity 90 %
0-2 mm	519 ± 617	385 ± 523	270 ± 423	213 ± 351	161 ± 263
2-4 mm	60 ± 45	69 ± 32	58 ± 20	57 ± 16	69 ± 11
4-20 mm	24 ± 9	35 ± 12	30 ± 10	30 ± 10	36 ± 12

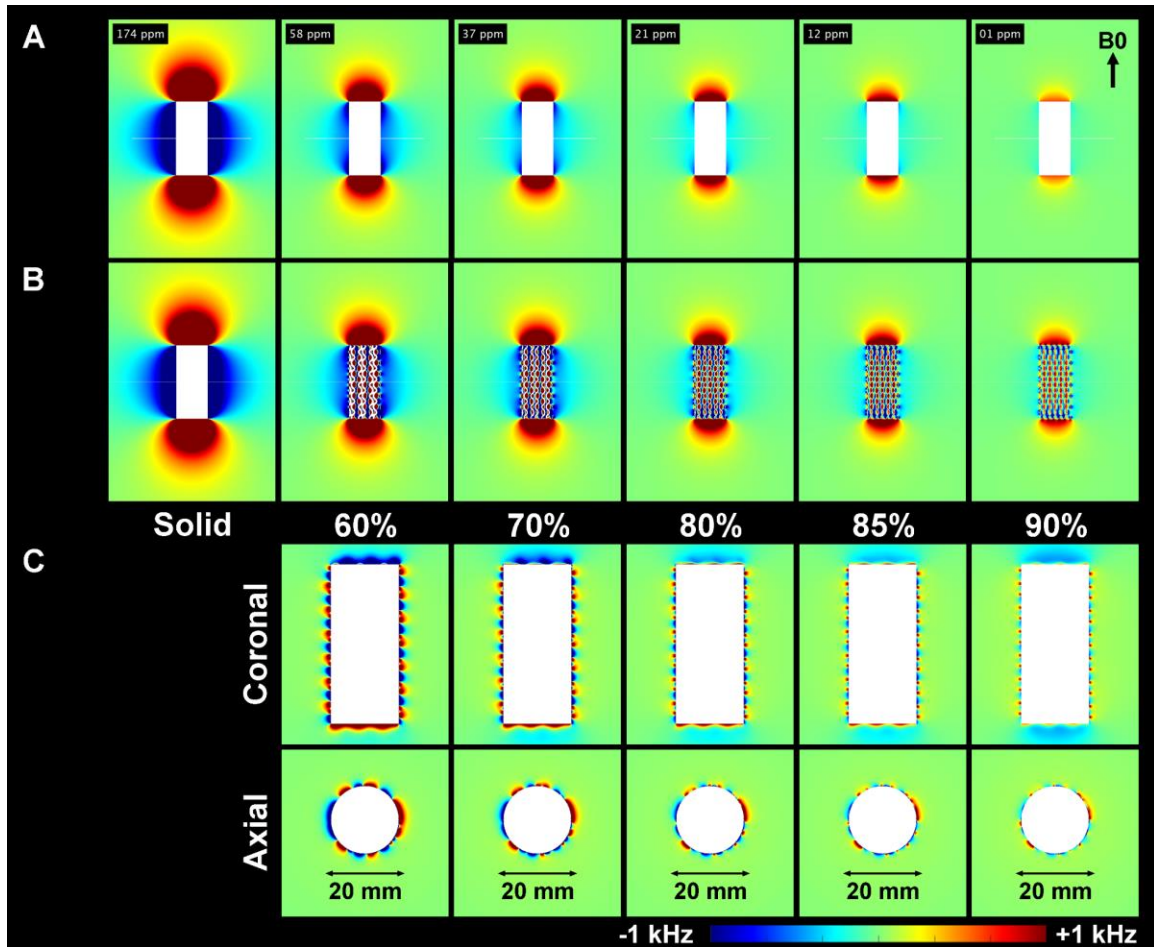


Figure 3.7 : (A) Field map simulations of homogeneous cylinders assigned porosity-dependent effective susceptibility (B) Simulated field maps of the gyroid-based porous cylinders, using the 3D geometry used for 3D-printing (0.1 mm^3 resolution, 174 ppm susceptibility). (C) Difference map comparing (A) and (B); difference maps are magnified to emphasize differences near the cylinder wall. The coronal and axial maps are from the corresponding central planes. Small inhomogeneities adjacent to the walls of the scaffold (mostly contained within 2 mm of the perimeter of the cylinder) are the likely source of signal loss seen in the scanned axial magnitude images.

3.4 Discussion and Conclusion

By observing and quantifying the “far-field” effect, where susceptibility differences between sufficiently close sources are effectively averaged when observed from a distance, we have shown strong quantitative evidence that the effective susceptibility of

porous metal scaffolds is linearly correlated with porosity. Our findings confirm that MRI around highly porous metal implants will have substantially reduced artifacts compared to solid implants. The introduction of a custom phantom that ensures alignment between simulated and scanned images represents a robust method for testing of various porosities and shapes in the future.

3.4.1 Effective Susceptibility

It has been shown that estimating magnetic susceptibility by comparing an acquired field map to simulations is possible in 2D,²⁴ where alignment of simulation and scan is readily achieved through a sheet of paper placed in the coronal plane, we extended this method to analyze a 3D object by introducing a customizable 3D-printed alignment grid and sample holder. The utility of the custom grid and holder was two-fold: first, centering the metal samples within the phantom facilitated gross alignment within the magnet; second, the specific geometry is needed to determine the image transformation that aligns the simulation and scan. In the presented experiments, the rotational and translational misalignment was small, however it is worth noting that even minor misalignments (as small as a 1° or 3 mm) between the scanned and simulated sample can shift the susceptibility estimate by 4-ppm and 8-ppm respectively.

3.4.2 Signal-void Volume

An earlier study, by Carter et al.,²¹ of artifact reduction using 3D-printed octahedral, diamond, and honeycomb lattice structures, confirmed the reduction in signal void volume, signal misplacement and phase wrapping with increasing porosity. They demonstrated a linear relationship between void volume and porosity in strut-based lattice structures (octahedral and diamond) while noting a relatively poor linear fit when examining a non-lattice honeycomb structure and hypothesized that the greater than expected artifact might be due to cell size (6 mm – similar to our scaffold). As the underlying mechanisms for signal loss are difficult to model rigorously, we elected to empirically quantify the relationship between void volume and porosity. We found a quadratic fit to be a better model compared to a linear fit, both in terms of goodness of fit

and how well the model extrapolates to the boundary volume of the cylinder at 100% porosity. The differences between the linear and quadratic fits were small and are likely related to our observation that the central axial cross section of all the porous cylinders exhibited a larger artifact size than the solid cylinder, which is consistent with the explanation proposed by Carter et al.²¹ We investigated this finding by analyzing the difference between simulations of the porous structure and its equivalent homogeneous susceptibility cylinder and found small field perturbations associated with the edges of the scaffold. The volume affected by these inhomogeneities is relatively small (within ~2 mm of the cylinder); however, the simulations show the alternating positive and negative fields adjacent to the cylinder result in substantial local field differences compared to a homogeneous cylinder of similar effective susceptibility. Future investigation may separate the sources of signal loss,³³ particularly the contributions of the susceptibility-induced intravoxel dephasing to T2' and ultimately T2* related signal loss.

3.4.3 Limitations

This study is limited to a single structure design made of a single material and using only a 3D-gradient echo sequence. The choice of sequence was focused on the accurate measurement of phase, with the assumption that spin echo sequences (typically used in orthopedics) would improve signal loss. The choice of unit cell structure (sheet-based gyroid) is primarily related to its favorable mechanical properties for use as an implant, with the expectation that the specific unit cell will only have an effect directly adjacent to the structure. The assumption that a gyroid-based porous cylinder can be approximated by a solid cylinder of lower effective susceptibility holds for the tested configuration, but this study may not predict the behavior of other lattice structures. However, the consistency between our results and those of the only other study of porous structures in MRI²¹ suggests that the effective susceptibility of small celled, strut-based isotropic lattice structures will follow the same trend we have observed with a sheet-based gyroid cell.

3.4.4 Conclusions

Substantial artifact reduction is achieved when using gyroid-based 3D-printed porous metal scaffolds compared to solid material, with a linear relationship between porosity and effective susceptibility; effective susceptibility shift approaches zero with increasing porosity. The porosity-effective susceptibility relationship results in a quadratic reduction in the signal-void volume stemming from porous implants, which will ultimately impact imaging time and image quality. Porous metal implants are an exciting development in orthopedics that is progressing rapidly towards clinical adoption and the ability to monitor the health of the implants non-invasively will only help to accelerate their development.

3.5 References

1. American Academy of Orthopaedic Surgeons. American joint replacement registry annual report 2019. Rosemont, IL: AAoS; 2019.
2. Canadian Institute for Health Information. Hip and knee replacements in Canada, 2017–2018: Canadian joint replacement registry annual report. Ottawa, ON: CIHI; 2019.
3. Martin BI, Mirza SK, Spina N, Spiker WR, Lawrence B, Brodke DS. Trends in lumbar fusion procedure rates and associated hospital costs for degenerative spinal diseases in the United States, 2004 to 2015. *Spine (Phila Pa 1976)* 2019;44(5):369-376.
4. Albano D, Messina C, Zagra L, Andreato M, De Vecchi E, Gitto S, Sconfienza LM. Failed total hip arthroplasty: Diagnostic performance of conventional MRI features and locoregional lymphadenopathy to identify infected implants. *J Magn Reson Imaging* 2020.
5. Rosinsky PJ, Bheem R, Meghpara MB, Haden M, Shapira J, Maldonado DR, Lall AC, Domb BG. Asymptomatic gluteal tendinopathies negatively impact outcomes of total hip arthroplasty: A propensity score-matched study. *J Arthroplasty* 2020.
6. Galley J, Sutter R, Stern C, Filli L, Rahm S, Pfirrmann CWA. Diagnosis of periprosthetic hip joint infection using MRI with metal artifact reduction at 1.5 T. *Radiology* 2020;296(1):98-108.
7. Schröder FF, Post CE, Wagenaar FBM, Verdonchot N, Huis In't Veld R. MRI as diagnostic modality for analyzing the problematic knee arthroplasty: A systematic review. *J Magn Reson Imaging* 2020;51(2):446-458.
8. Koch KM, Brau AC, Chen W, Gold GE, Hargreaves BA, Koff M, McKinnon GC, Potter HG, King KF. Imaging near metal with a MAVRIC-SEMAC hybrid. *Magn Reson Med* 2011;65(1):71-82.
9. Lu W, Pauly KB, Gold GE, Pauly JM, Hargreaves BA. Slice encoding for metal artifact correction with noise reduction. *Magn Reson Med* 2011;65(5):1352-1357.
10. Filli L, Jud L, Luechinger R, Nanz D, Andreisek G, Runge VM, Kozerke S, Farshad-Amacker NA. Material-dependent implant artifact reduction using SEMAC-VAT and MAVRIC: A prospective MRI phantom study. *Invest Radiol* 2017;52(6):381-387.
11. Arabnejad S, Johnston B, Tanzer M, Pasini D. Fully porous 3D printed titanium femoral stem to reduce stress-shielding following total hip arthroplasty. *J Orthop Res* 2017;35(8):1774-1783.

12. Carpenter RD, Klosterhoff BS, Torstrick FB, Foley KT, Burkus JK, Lee CSD, Gall K, Guldborg RE, Safranski DL. Effect of porous orthopaedic implant material and structure on load sharing with simulated bone ingrowth: A finite element analysis comparing titanium and peek. *J Mech Behav Biomed Mater* 2018;80:68-76.
13. Zaharin HA, Abdul Rani AM, Azam FI, Ginta TL, Sallih N, Ahmad A, Yunus NA, Zulkifli TZA. Effect of unit cell type and pore size on porosity and mechanical behavior of additively manufactured ti6al4v scaffolds. *Materials (Basel)* 2018;11(12).
14. Cheong VS, Fromme P, Mumith A, Coathup MJ, Blunn GW. Novel adaptive finite element algorithms to predict bone ingrowth in additive manufactured porous implants. *J Mech Behav Biomed Mater* 2018;87:230-239.
15. Cheong VS, Fromme P, Coathup MJ, Mumith A, Blunn GW. Partial bone formation in additive manufactured porous implants reduces predicted stress and danger of fatigue failure. *Ann Biomed Eng* 2020;48(1):502-514.
16. Mumith A, Cheong VS, Fromme P, Coathup MJ, Blunn GW. The effect of strontium and silicon substituted hydroxyapatite electrochemical coatings on bone ingrowth and osseointegration of selective laser sintered porous metal implants. *PLoS One* 2020;15(1):e0227232.
17. McGilvray KC, Easley J, Seim HB, Regan D, Berven SH, Hsu WK, Mroz TE, Puttlitz CM. Bony ingrowth potential of 3D-printed porous titanium alloy: A direct comparison of interbody cage materials in an in vivo ovine lumbar fusion model. *Spine J* 2018;18(7):1250-1260.
18. Arts M, Torensma B, Wolfs J. Porous titanium cervical interbody fusion device in the treatment of degenerative cervical radiculopathy; 1-year results of a prospective controlled trial. *Spine J* 2020;20(7):1065-1072.
19. Krafft P, Osburn B, Vivas A, Rao G, Alikhani P. Novel titanium cages for minimally invasive lateral lumbar interbody fusion: First assessment of subsidence. *Spine Surg Relat Res* 2020;4(2):171-177.
20. Alamanda VK, Demartino I, Potter HG, Koff MF, Lin B, Muskat A, Westrich GH. Multiacquisition variable-resonance image combination magnetic resonance imaging used to study detailed bone apposition and fixation of an additively manufactured cementless acetabular shell. *Arthroplast Today* 2020;6(4):694-698.
21. Carter LN, Addison O, Naji N, Seres P, Wilman AH, Shepherd DET, Grover L, Cox S. Reducing MRI susceptibility artefacts in implants using additively manufactured porous ti-6al-4v structures. *Acta Biomater* 2020.
22. Schoen AH. Reflections concerning triply-periodic minimal surfaces. *Interface Focus* 2012;2(5):658-668.

23. Kelly CN, Francovich J, Julmi S, Safranski D, Guldberg RE, Maier HJ, Gall K. Fatigue behavior of as-built selective laser melted titanium scaffolds with sheet-based gyroid microarchitecture for bone tissue engineering. *Acta Biomater* 2019;94:610-626.
24. Perkins SL, Daniel BL, Hargreaves BA. Mr imaging of magnetic ink patterns via off-resonance sensitivity. *Magn Reson Med* 2018;80(5):2017-2023.
25. Holdsworth DW, Teeter MG, Milner JS, Pollmann SI, Drangova M; Method and apparatus for measuring 3D geometric distortion in MRI and CT images with a 3D physical phantom US patent 10,557,911. 2020 February 11, 2020.
26. Och JG, Clarke GD, Sobol WT, Rosen CW, Mun SK. Acceptance testing of magnetic resonance imaging systems: Report of aapm nuclear magnetic resonance task group no. 6. *Med Phys* 1992;19(1):217-229.
27. Li L. Magnetic susceptibility quantification for arbitrarily shaped objects in inhomogeneous fields. *Magn Reson Med* 2001;46(5):907-916.
28. Otsu N. A threshold selection method from gray-level histograms. *IEEE Transactions on Systems, Man, and Cybernetics* 1979;9(1):62-66.
29. Liu J, Drangova M. Intervention-based multidimensional phase unwrapping using recursive orthogonal referring. *Magn Reson Med* 2012;68(4):1303-1316.
30. Bouwman JG, Bakker CJ. Alias subtraction more efficient than conventional zero-padding in the fourier-based calculation of the susceptibility induced perturbation of the magnetic field in MR. *Magn Reson Med* 2012;68(2):621-630.
31. Schenck JF. The role of magnetic susceptibility in magnetic resonance imaging: MRI magnetic compatibility of the first and second kinds. *Med Phys* 1996;23(6):815-850.
32. Smith MR, Artz NS, Wiens C, Hernando D, Reeder SB. Characterizing the limits of MRI near metallic prostheses. *Magn Reson Med* 2015;74(6):1564-1573.
33. De Guio F, Benoit-Cattin H, Davenel A. Signal decay due to susceptibility-induced intravoxel dephasing on multiple air-filled cylinders: MRI simulations and experiments. *Magma* 2008;21(4):261-271.

Chapter 4

4 Characterizing Diffusion-Controlled Release of Small-Molecules Using Quantitative MRI: Application to Orthopedic Infection

4.1 Introduction

When developing a localized drug delivery system, the goals are to precisely target the cause of the disease and deliver the correct therapeutic concentration over an optimal time period.¹ To reach these goals, a carrier material, typically in the form of a simple matrix system,² hydrogels,^{3,4} or targeted nanoparticles,^{5,6} are incorporated with drugs and placed at the disease sites.¹ As a matrix-type carrier, calcium sulfate hemihydrate has a long history for the delivery of small molecules in a variety of applications, such as the delivery of antibiotics,^{7,8} cancer-related drugs,⁹ and other bioactive agents.² Being used as a bone filler¹⁰ and bone graft substitute¹¹ in orthopedics, calcium sulfate has earned an excellent reputation for its biocompatibility and osteoconductive properties.¹² Currently, calcium sulfate is commonly used to deliver antibiotics to treat periprosthetic joint infection (PJI),^{13,14} where infection is currently the leading cause of early revision of both hip and knee infections in North America^{15,16} and is likely to grow more prominent,¹⁷ particularly as implant design improves fixation and mechanical stability.

Techniques to improve the characterization of periprosthetic antibiotic release is an active area of research, including numerous *in vitro* studies of drug diffusion from calcium sulfate antibiotic carriers via chemical analysis of eluants.^{7,18} While it is possible to run an *in-vivo* study examining antibiotic elution through surgical drains and serum, they are limited by concerns over prolonged drain placement⁷ and the lack of the information about the dynamical diffusion process. These limitations contribute to a need for a means of non-invasive measurement of antibiotic release from calcium sulfate using imaging techniques, which would improve our understanding of localized antibiotic delivery in

the treatment of PJI, particularly *in vivo*. Micro-CT has previously been proposed as a viable means of characterizing diffusion-controlled release of small-molecules through the use of a contrast agent¹⁹ – contrast agent loaded into a calcium sulfate matrix core releasing into a surrounding volume of agar over multiple time points. This proof of concept – using a contrast agent as a surrogate for a therapeutic small molecule – was demonstrated to be effective with micro-CT, but clinical application may be limited due to the risks associated with ionizing radiation.

There are a few factors that indicate that MRI is a viable alternative modality to CT for imaging the diffusion-controlled release of small-molecules, specifically gadolinium contrast agents. Critically, studies have shown that quantitative MRI is highly correlated to both gadolinium concentration²⁰ and CT-attenuation values.²¹ Molecular weight is known to be a dominant factor in small-molecule diffusion²² and gadolinium-based contrast agents are of similar molecular weight to the antibiotics that are commonly deployed for orthopedic applications. Furthermore, calcium sulfate is unlikely to generate large field inhomogeneities; as a diamagnetic material,²³ calcium sulfate should be a net positive by offsetting some of the magnetic susceptibility increase introduced by the addition of gadolinium.

One prominent concern surrounding localized drug delivery, particularly in orthopedics, is that most carriers, including calcium sulfate, lack load-bearing capability.²⁴ Preliminary attempts to alleviate this concern include a study of the effects of deploying calcium sulfate within a simple reservoir built through resin 3D-printing,²⁵ however a better solution may be found through metal 3D-printing. A recently proposed example of this is the use of 3D-printed porous metal implants, which shows excellent mechanical suitability,^{26,27} promising influence on bone ingrowth,²⁸ and clinical viability.²⁹ These porous metal implants have also found to be suitable for loading drug-laden porous gelatin³⁰ and antibacterial hydrogels³¹ by incorporating the carrier material into the implant's void spaces. Similarly, incorporating calcium sulfate into a porous implant would allow the metal structure to act as a scaffold that alleviates mechanical load from the carrier, which would allow the combined implant to elute antibiotics directly into the periprosthetic space instead of on the periphery of the infected joint. However,

performing quantitative MRI around metals faces challenges associated with the susceptibility-induced field inhomogeneity that leads to artifacts in both magnitude and phase. Fortunately, it has been previously shown that highly porous 3D-printed metal scaffolds³² exhibit decreased effective susceptibility proportional to their porosity, and thus a highly porous scaffold filled with calcium sulfate may still be amenable to MRI-based measurements and eventual clinical monitoring.

The objective of this study is to quantitatively measure the release and diffusion of contrast agents loaded into calcium sulfate, both on its own and contained within a porous metal scaffold. Specifically, we used a clinically available gadolinium-based contrast agent with a molecular weight similar to antibiotic drugs likely to be used in clinic. We acquired multi-echo GRE data at multiple time points over 4 weeks on a 3 T scanner. For each time point, we generated the $R2^*$ and QSM maps based on the multi-echo data. By hypothesizing that both $R2^*$ and QSM are linearly correlated to concentration of the release of contrast agent from the core into the agar, we fitted the multi-time points $R2^*$ and QSM values with the mathematical model for characterizing diffusion-controlled release of small-molecules.³³

4.2 Methods

4.2.1 Experimental Setup

The experimental setup consists of a central cylindrical core made of a carrier material that releases small molecules into a surrounding agar contained in a plastic enclosure, creating a finite-source, finite-sink setup. A silicone-elastomer mold to form the core is created from a two-part negative mold designed in Solidworks (Dassault Systèmes, Vélizy-Villacoublay, France) (Figure 4.1A) that is 3D-printed in polylactic acid (PLA). The mold is designed to form a cylinder of 17 mm radius and 40 mm length which will constitute the central core. The enclosure, which contains both the core and its surrounding agar, has a diameter of 70 mm and either a raised inset to place the core (diffusion experiment) or a 42 mm high wall that prevents the release of the molecules (Figure 4.1B). The “blocked” phantom is needed to separate the effect of the

susceptibility induced field inhomogeneity generated by the core from the effect of the increased concentration of the diffused molecules. The enclosures are 3D-printed on a Dremel 3D45 (Dremel, Mt. Prospect, Illinois) using clear Polyethylene terephthalate glycol for the diffusion experiment or white PLA for the blocked experiment.

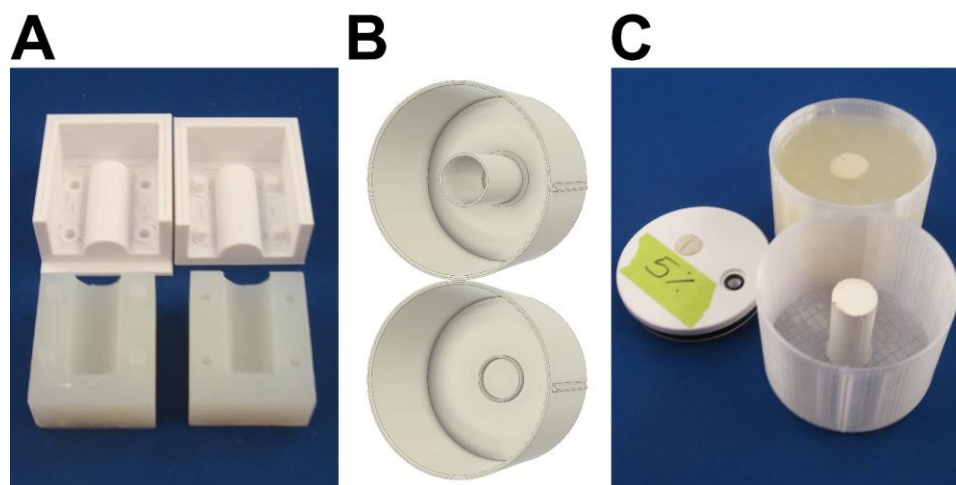


Figure 4.1: A) Silicone mold made from 3D-printed PLA negatives B) Enclosures to hold central core (top: blocked diffusion, bottom: free diffusion) C) Assembled sample (top: core surrounded by agar, bottom: core placed into inset prior to pouring agar)

4.2.2 Sample Preparation

50 mmol/L Gadobutrol solution is prepared by diluting Gadovist (Bayer Inc., Leverkusen, Germany) with distilled water at a 1:20 ratio. Calcium sulfate hemihydrate powder (Stimulan, Biocomposites Ltd., England) is mixed with 6 ml of the dilute Gadovist. The resulting paste is poured into the silicone mold and left to set overnight, forming a cylindrical core. 1 L of distilled water is boiled to remove any dissolved gas, allowed to cool to room temperature in a sealed container and then mixed with 35 g of agar and 80 mL of glycerol. The agar is heated to approximately 90 °C and skimmed to remove impurities and air bubbles. The core is set into the enclosure and the agar is poured at 60 °C. The assembled samples are left to set for 3 hours prior to scanning (Figure 4.1C).

4.2.3 Phantom Design

The phantom used in this study serves two purposes: holding a set of calibration vials and providing a set of 3 fiducial markers needed to ascertain the phantom's precise orientation and center. Eight 2 mL calibration vials (Fisher Scientific, Waltham, Massachusetts) were prepared at 0.125, 0.25, 0.5, 1, 1.5, 2 and 2.5% of the raw (0.5 mmol/mL Gd) contrast agent (Magnevist; Berlex Laboratories; Wayne, NJ) in distilled water along with a vial of only distilled water, matching previous work in our lab.³⁴ Three vials are filled with agar made with 1.0%, 0.5% and without Magnevist to assess the effect of agar on our quantitative images. Two vials of peanut oil are also included to evaluate the effect of fat on our acquisition. The vials are held within a 3D-printed PLA construct; the configuration of these vials is shown in Figure 4.2A. The 3D-printed construct is also built with three 7-mm spherical markers used to determine the phantom's orientation relative to the coronal imaging plane. These markers are placed along a planar circle with a 51.45 mm radius. Lastly, the inner ring is designed to snugly fit the enclosures holding the samples, keeping the core in the center of the ring formed by the markers and their relative orientations the same throughout the experiment. The outer ring is designed to be placed within a 130 mm diameter plastic container. The construct, vials, and sample enclosure are placed in the plastic container and embedded in agar (Figure 4.2B).

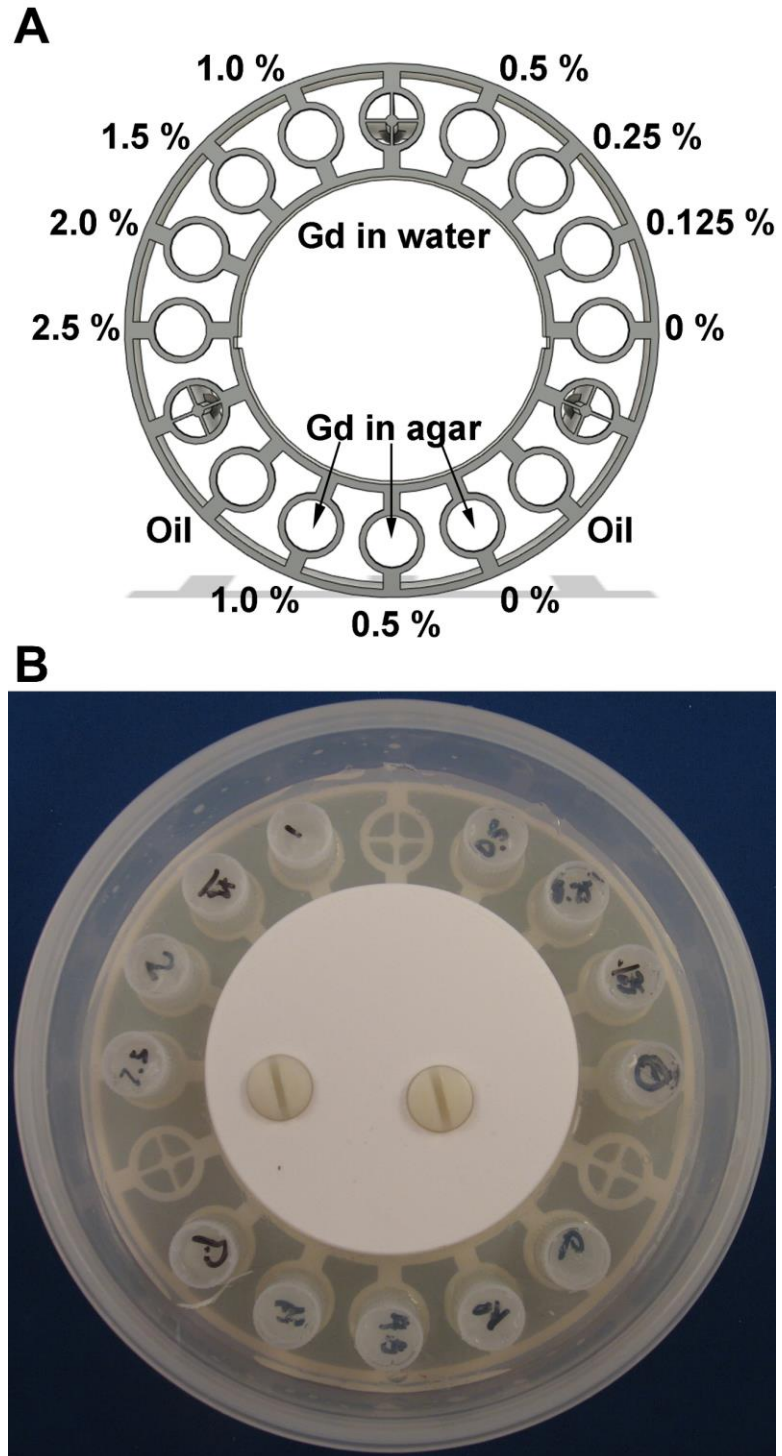


Figure 4.2: A) Configuration of calibration vials and spherical markers used in registration B) Assembled phantom with calibration vials set in agar

4.2.4 Gyroid-Based Porous Metal Core

The metal scaffold was designed based on a sheet based gyroid, a triply periodic minimal surface that has been shown to have favorable mechanical properties for orthopedic applications, such as stiffness similar to bone and an appropriate strength for load-bearing implants.²⁶ The scaffolds, whose effective susceptibility has been previously studied,³² are modelled using Blender (Version 2.79, blender.org, Amsterdam, Netherlands), using a 6 mm³ unit cell (Figure 4.3A) with 0.2 mm wall thickness arranged into a 3x3x8 array, which is then truncated by into a cylinder matching the central core (Figure 4.3B). The resulting model was exported from Blender as STL (stereolithography) files and sliced for fabrication by QuantAM build preparation software (Renishaw plc, Wotton-under-Edge, United Kingdom). The structures were 3D printed in Ti6Al4V medical grade titanium alloy (Ti6Al4V ELI-0406, Renishaw plc, United Kingdom, particle size 15-45 µm) using laser powder-bed fusion (AM400, Renishaw plc, Wotton-under-Edge, United Kingdom) at ADEISS (London, Canada) with a laser spot diameter of 70 µm and layer thickness of 40 µm. The porous metal scaffold is loaded by filling the silicone mold with the gadolinium-loaded calcium sulfate and inserting the metal core prior to setting, which allows the fluid paste to fill the void spaces of the gyroid structure (Figure 4.3C).

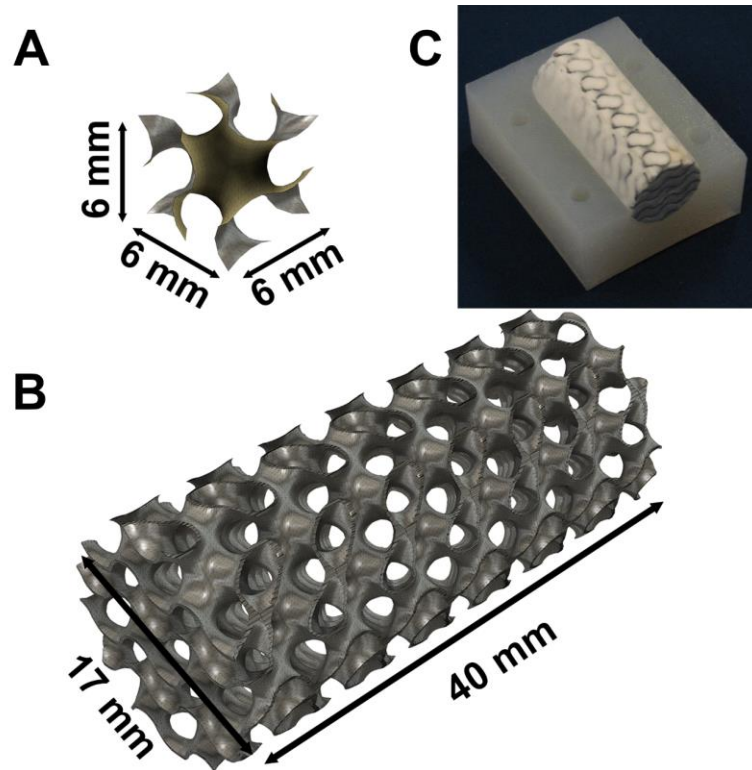


Figure 4.3: A) Sheet-based gyroid unit cell B) Array of unit cells with 0.2 mm wall thickness truncated into cylinder C) Titanium 3D-printed scaffold filled with calcium sulfate

4.2.5 Imaging

Imaging was done on a 3T Prisma scanner (Siemens, Munich, Germany) with a Siemens 32-channel head coil. Scans were acquired using a 3D multi-echo GRE sequence with echo times at 4.16 ms, 5.52 ms, 6.88 ms, 8.26 ms, 9.76 ms, 11.67 ms, 14.00 ms, 16.34 ms, 18.67 ms, and 21.00 ms (echo train length = 10) at 1 mm^3 resolution. The other parameters include TR=24 ms, BW=1010 Hz/pixel, matrix size=160x160x60, 16 cm FOV and a total acquisition time of 3 minutes and 50 seconds. The phantom was scanned in a coronal configuration, with the samples perpendicular to B0. Scans were performed 3 hours and 10 hours after pouring the agar, followed by 3 subsequent days of scans (32 h, 56 h, 80 h) and then scans at 1 week, 2 weeks and 4 weeks. Phase and magnitude images are channel combined and reconstructed on the scanner then exported as DICOM files.

4.2.6 Quantitative Mapping

Multi-echo complex data is assembled and processed in Matlab (Mathworks, Natick, Massachusetts) from the scanner reconstructed magnitude and phase images. Complex images are processed using the B0-NICE algorithm developed in our lab³⁴⁻³⁶ to generate fat fraction, $R2^*$, and B0 maps from the 10 echoes. The $R2^*$ map is calculated based on data-fitting of the magnitude images from the 10 echoes with echo spacing shortened (relative to other published applications) to reduce the effects of field inhomogeneity in the late echoes. QSM maps are generated using the MEDI algorithm³⁷ implemented on the 10-echo complex data and normalized to the distilled water vial. The QSM maps are used to measure the drop in core susceptibility as the contained gadolinium is released into the surrounding agar.

4.2.7 Phantom Co-Registration

4.2.7.1 Marker Locations

The locations of the spherical markers are taken from the first echo magnitude image. An estimate of the center of the phantom is generated by creating a binary image of the signal generating part of the whole phantom (the bright agar) through thresholding, morphologically dilating the binary image to remove all the negative (low signal) parts of the image, including the markers and any other parts of the plastic construct, and finding the resulting centroid. The outer construct (the 3D-printed part containing the markers) is isolated by masking the sample (the core and surrounding agar within the enclosure) by simply creating a zero-mask centered from the centroid of the whole phantom. A binary image of the low-signal parts of the image that remains (containing the markers) is created and morphologically eroded to remove the marker's supporting structure and any other small low signal volumes. The spherical markers are identified by their roundness and size to eliminate extraneous low signal volumes. Thresholds and structuring element sizes (which determine the extent of morphological dilation and erosion) are adjusted as needed to isolate exactly 3 centroids. For this experiment, a magnitude threshold of 50 and a 2-mm spherical structuring element isolates the markers, whose centroids are calculated.

4.2.7.2 Phantom Alignment

The center of the circle formed by the 3 markers indicates the precise coordinates of the center of the sample core. The markers also provide a measurement of both the in-plane rotation and through-plane tilt of the phantom within the magnet. The radial symmetry of the sample (core and agar) indicates that the in-plane alignment of the phantom does not need to be corrected for to generate radially equivalent line profiles. To correct for through-plane tilt, an iterative closest point registration between the X and Y coordinates of the markers projected onto the coronal plane (the “mid-slice” corresponding the average Z-values of the markers) and the actual centroid locations (with the off-plane Z-values) is performed. This provides the rotation matrix governing the through-plane tilt of the sample, which is critical to being able to sample and average radially equidistant points from the central core.

4.2.8 Data Analysis

Magnitude images, $R2^*$ and QSM maps were analyzed at each time point for both sample types (calcium sulfate only and calcium sulfate in metal) in both free diffusion and blocked enclosures. Quantitative analysis is done using radially averaged line profiles centered on the central core. All data analysis is done in Matlab.

4.2.8.1 ROI analysis

Analysis of the calibration vials are done with 8-mm circular regions of interest (ROI) across 3 slices. The ROIs are placed in the slice centered on the markers. The same ROIs are used to analyze the $R2^*$ and magnitude images. QSM images are analyzed by centering the ROI on the central core and the resulting susceptibility is corrected using an ROI centered on the distilled water vial.

4.2.8.2 Radial Averaging

A radial averaging approach is employed to improve signal-to-noise ratio, minimize non-uniformities within the agar (e.g., small air bubbles) and simplify quantification and

analysis while examining the slow diffusion of contrast agent through the agar. Radial averaging takes advantage of the radial symmetry of the sample and the radial nature of the diffusion of gadolinium from the cylindrical core to average sample points that are equidistant to the core. In a case where the phantom is aligned with the coronal plane, this is simply done by creating line profiles radiating from the center of the phantom. However, any tilt in the phantom breaks this symmetry within the coronal imaging plane, thus a correction is necessary. This adjustment is done by applying the rotation matrix governing through-plane tilt calculated from the marker centroids to the line profiles aligned with the coronal plane and center of the phantom. This generates a set of line profiles that crosses multiple slices to sample points that maintain radial symmetry. Each data point (at some distance to the core and elapsed time) consists of 600 total samples, spanning 5 slices of 120 points spaced 3 degrees apart. Standard deviations are calculated for each point as a measure of the data's reliability.

4.2.8.3 Gadolinium Release

The diffusion of small molecules can be modelled generally using Fick's laws of diffusion³³. However, our system (Gadovist in calcium sulfate formed into a cylinder) imitates a cylindrical diffusion-controlled (predominantly controlled by diffusional mass transport) drug delivery system, which has a known model.³³ A calcium sulfate core constitutes a 'monolithic solution', as the molecule of interest is dispersed homogeneously throughout the calcium sulfate matrix, and thus the "drug" (Gadovist) release can be described by the approximation:³³

$$\frac{M_t}{M_\infty} = 1 - \frac{4}{2.405^2} \exp\left(-\frac{2.405^2 Dt}{R^2}\right) \quad (4.1)$$

where $M(t)$ is the cumulative amount of drug released at time t , $M(\infty)$ is the cumulative amount of drug released at infinity, D is the diffusion coefficient of the drug within the system, and R is the radius of the inner core cylinder. If $R2^*$ and concentration are linearly correlated, we can use the mean $R2^*$ value within the agar to measure the release of gadolinium from the core into the enclosed agar through the ratio:

$$\frac{M_t}{M_\infty} = \frac{R2^*_{avg}(t)}{R2^*_{avg}(\infty)} \cong \frac{R2^*_{avg}(t)}{R2^*_{avg}(final)} \quad (4.2)$$

With the approximation that $R2^*_{avg}(\infty)$ is equivalent to $R2^*_{avg}(final)$, taken from the 4-week time point. $R2^*$ values are sampled using a disk-shaped mask with a 9-mm radius hole (to remove the central core) and 35-mm radius outer diameter (the wall the enclosure). The mask is centered on the calculated center of the central core and aligned to the plane made by the spherical markers using the rotation matrix governing the through-plane tilt. A baseline value is calculated from the samples without diffusion (where the core is walled off from the agar) using the same mask. For the calcium sulfate-only core (non-metal), best-fit curves (exponential plateau) are calculated while constraining the constants to find the diffusion coefficient of the system. The addition of metal invalidates this model; thus, that data is fit without constraints. The QSM values from the calcium sulfate core are calculated with an 8-mm circular centered on the core

and compared with the release curve, where the susceptibility should decrease proportional to the increase in $R2^*_{avg}(t)/R2^*_{avg}(final)$.

4.2.8.4 Statistical Analysis

Standard deviations are calculated for each radially averaged point in the line profiles. Relative release curves are fitted to $R2^*$ data using an exponential plateau model and quality of fit evaluated by coefficient of determination (R-squared value). All curve fitting and statistics are done in Prism 9 (version 9.0.0, Graphpad Software, San Diego, California).

4.3 Results

4.3.1 Images of the Calcium Sulfate Core

Figure 4.4 summarizes the magnitude images (Figure 4.4A), $R2^*$ (Figure 4.4B) and QSM (Figure 4.4C) maps at the radially symmetric plane formed by the three markers at various time points over 4 weeks. The magnitude images (Figure 4.4A) show the signal enhancement generated by the released, diffusing gadolinium, where the radius of the high signal circle increases over time. $R2^*$ images (Figure 4.4B) demonstrate a clear increase in $R2^*$ in the agar surrounding the central core, as expected with the increasing quantity of gadolinium being released from the core. The QSM images (Figure 4.4C) show changes within the calcium sulfate core, where the core's magnetic susceptibility decreases as the high susceptibility gadolinium diffuses into the surrounding agar. Radially averaging the magnitude, $R2^*$ and QSM images into line profiles (Figure 4.5) provides further insight into the images. The line profiles show that magnitude images do not change substantially beyond 7 days, suggesting that it takes a week for the initially released contrast agent to diffuse through the agar to the periphery of the sample. The $R2^*$ curves demonstrate a decreasing peak over time (<10 mm from the core) and an increasing concentration distal to the core (>20 mm from the center), which indicates that the total amount of gadolinium leaving the core is decreasing and the total amount of gadolinium in the agar is increasing.

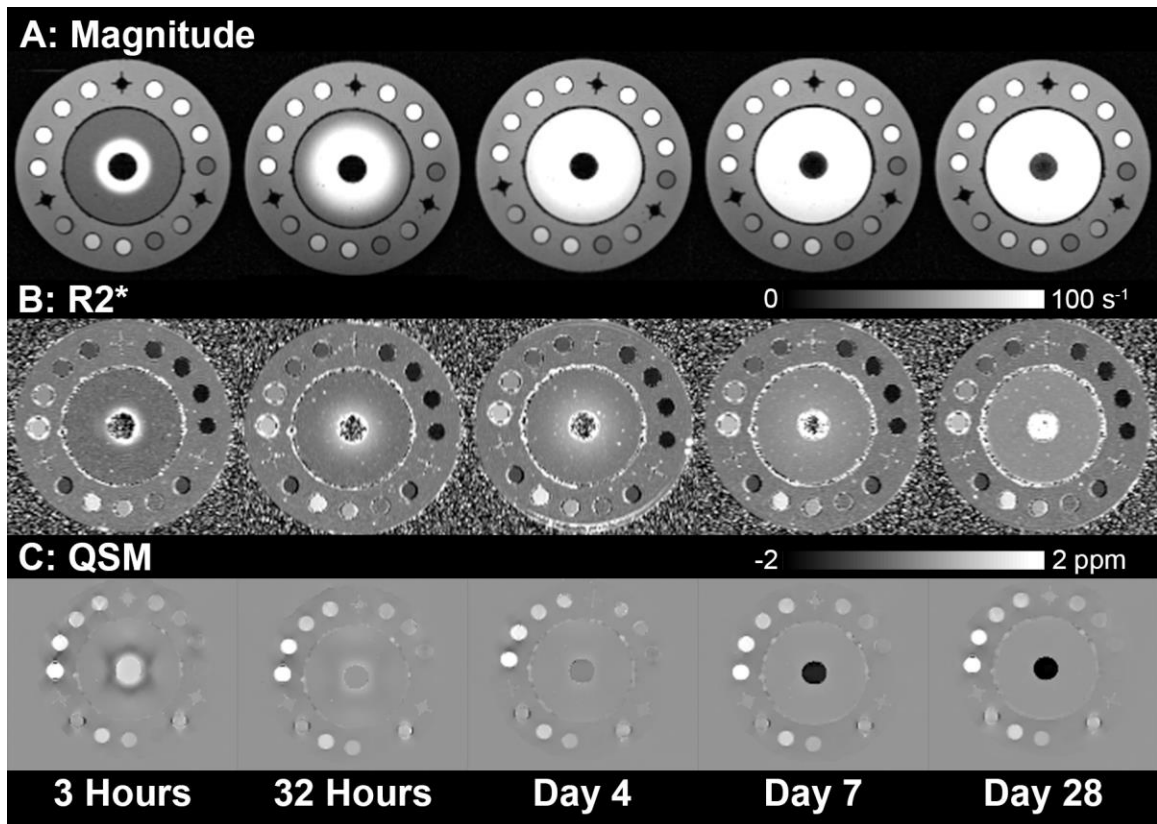


Figure 4.4: Time-series of magnitude, R2* and QSM images at time points ranging from 3 hours to 4 weeks. Slice shown is the plane of radial symmetry that bisects all three spherical markers. A) Magnitude images of calcium sulfate (Stimulan) loaded with gadolinium contrast agent (Gadovist) B) R2* images calculated from signal decay over 10 echoes. C) QSM map showing the core susceptibility decreasing as gadolinium is released

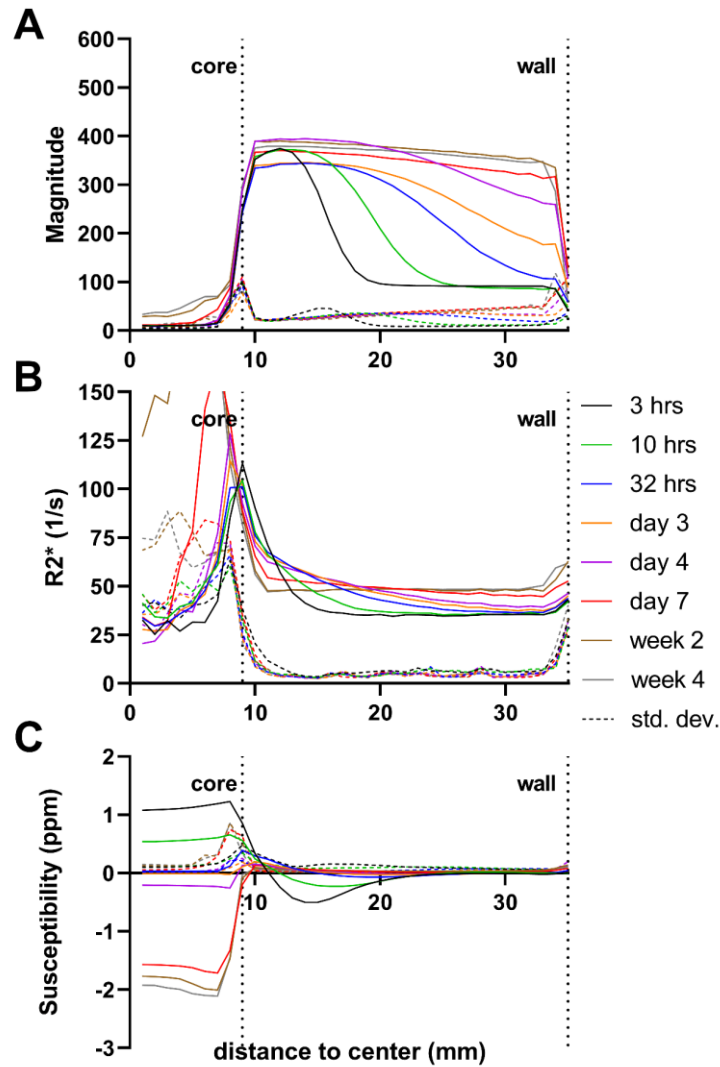


Figure 4.5: Radially averaged line profiles. Each data point averages 600 total samples, spanning 5 slices of 120 points spaced 3 degrees apart. Standard deviations (dotted lines of matching colors) are calculated for each point as a measure of the data's reliability. A) Average intensity of magnitude images (B) $R2^*$ line profiles. The lack of signal within the core resulted in a noisy fitting and was thus discarded. C) QSM line profiles. While the concentration of gadolinium is not detectable within the agar, QSM is sensitive to the change in susceptibility of the core as gadolinium is released.

4.3.2 Images of Calcium Sulfate in a Porous Metal Scaffold

The porous metal scaffold was built with 92.56% porosity (measured by mass). The addition of metal has a clear effect on the first echo magnitude images (Figure 4.6A), particularly at early time points. The strong signal enhancement is still apparent but the signal void surrounding the core has less defined edges, suggesting that the artifact stems from the metal structure. The field inhomogeneity induced by the titanium scaffold is apparent in $R2^*$ (Figure 4.6B), resulting in the volume adjacent to the core exhibiting a fast-decaying signal (high $R2^*$). The higher susceptibility of the core results in poor QSM mapping, although it shows a decrease in core susceptibility over time (Figure 4.6C). The radially averaged line profiles confirm these observations, with a magnitude profile that is very similar to the non-metal experiment (Figure 4.7A), a very high peak $R2^*$ (Figure 4.7B), and core QSM values (Figure 4.7C) that are substantially higher than those without the metal scaffold. It is particularly noteworthy that the week 2 scan resulted in a QSM image of poor quality, leading to very high standard deviations in the averaged line profile.

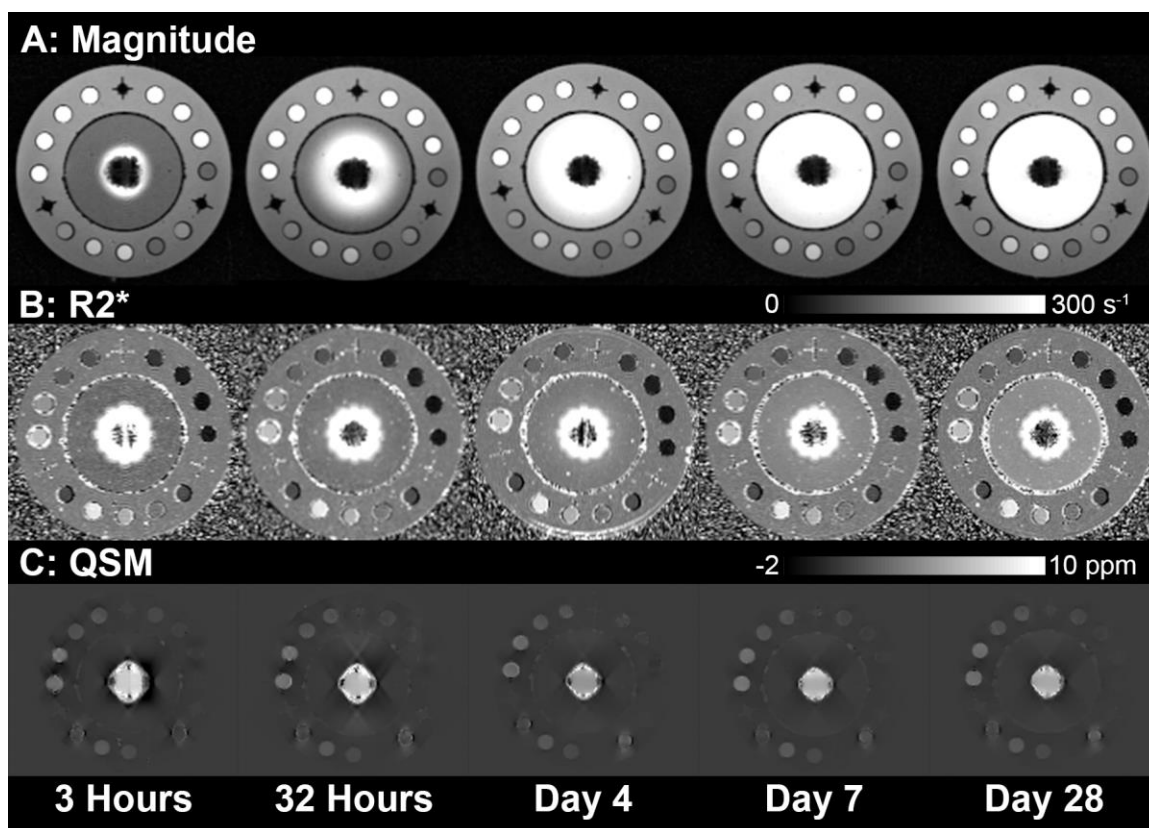


Figure 4.6: Time-series of magnitude, $R2^*$ and QSM images at time points ranging from 3 hours to 4 weeks of gadolinium-loaded calcium sulfate in a porous metal scaffold. Slice shown is the plane of radial symmetry that bisects all three spherical markers. A) Magnitude images of calcium sulfate (Stimulan) loaded with gadolinium contrast agent (Gadovist) in a 3D-printed titanium-alloy porous scaffold B) $R2^*$ images calculated from signal decay over 10 echoes. $R2^*$ values near the core are heavily affected by field inhomogeneity. C) QSM map showing the core susceptibility decreasing as gadolinium is released. The higher susceptibility metal scaffold results in poor susceptibility estimates.

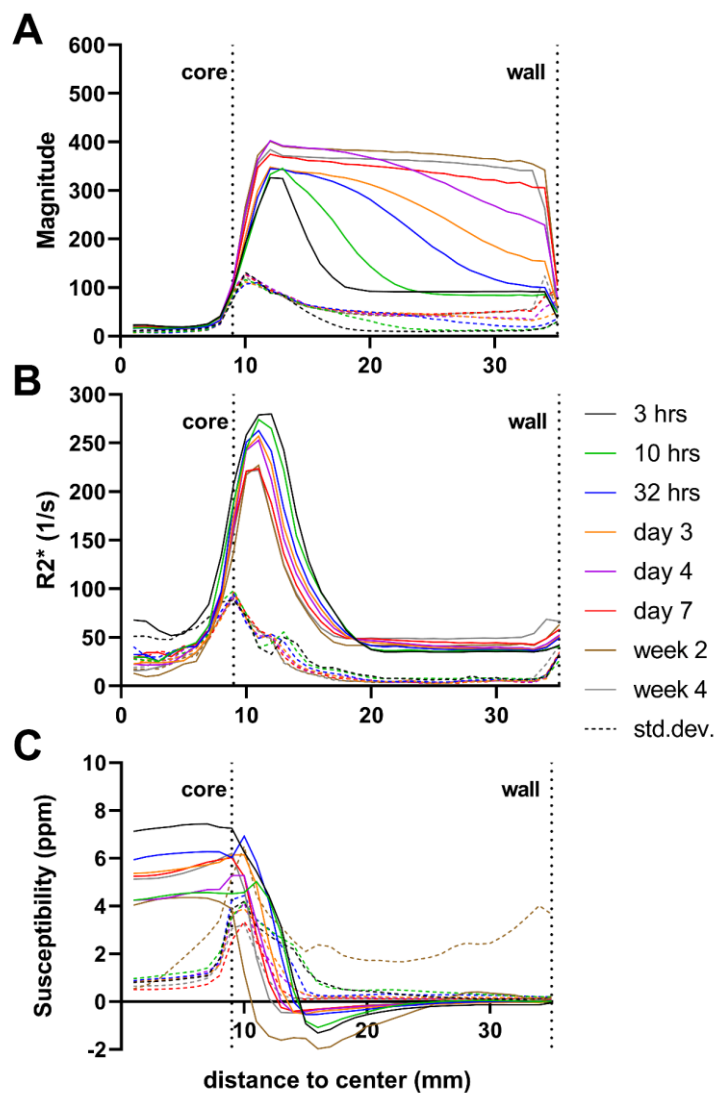


Figure 4.7: Radially averaged line profiles when a metal scaffold is added to the core. Each data point averages 600 total samples, spanning 5 slices of 120 points spaced 3 degrees apart. Standard deviations (dotted lines of matching colors) are calculated for each point as a measure of the data's reliability. A) Average intensity of magnitude images (B) $R2^*$ line profiles. The lack of signal within the core resulted in a noisy fitting and was thus discarded. C) QSM line profiles. The addition of metal to the calcium sulfate core increased susceptibility as expected but resulted in poor overall data quality. Notably, the week 2 QSM image had artifacts that are reflected by a high standard deviation

4.3.3 Relationship Between Concentration, Magnitude, R2* and QSM

The calibration vials show a linear relationship between concentration and R2*, between concentration and QSM, but not between concentration and magnitude (Figure 4.8). This indicates that the use of R2* and QSM as a quantitative measurement of gadolinium concentration is appropriate, particularly for the calculation of total release and diffusion coefficient as the ratio between concentration, R2*, and QSM will be consistent.

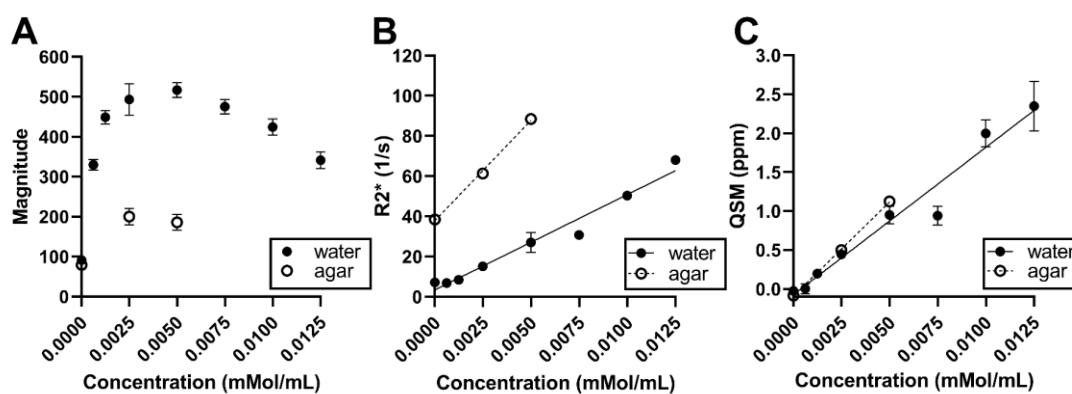


Figure 4.8: Volume average of 3 slices of each calibration vial (8 mm ROI). A) Magnitude; no correlation. B) R2*; linear fit: water vials R2 = 0.956, slope = 125 s-1/M; agar vials R2 = 0.995, slope = 148 s-1/M. C) QSM; linear fit: water vials R2 = 0.938, slope = 6.16 ppm/M; agar vials R2 = 0.993, slope = 4.48 ppm/M.

4.3.4 Total Release and Diffusion Coefficient

The total concentration of gadolinium in the agar yields a set of R2* ratios governing the release of contrast agent out of the calcium sulfate into the agar. A baseline value of 33.74 s^{-1} and 33.56 s^{-1} for non-metal (calcium sulfate-only) and metal cores respectively was averaged from the non-diffusing samples and subtracted from the average R2* values prior to calculating the release curve. For the calcium sulfate-only core, the resulting curve (Figure 4.9A, non-metal) has an R²-value of 0.991, indicating that the data fits the theoretical model³³ well. The curve-fit results in a decay constant of 3.67×10^{-6} , yielding a diffusion constant of $4.59 \times 10^{-11} \text{ m}^2/\text{s}$. Fitting the core susceptibility values

from the QSM images (Figure 4.9B, non-metal) yields an exponential decay with an R^2 -value of 0.969 and a decay constant of 2.4×10^{-6} . The addition of metal results in a release curve that still exhibits a similar exponential plateau (Figure 4.9A, metal) with a decay constant of 2.37×10^{-6} and R^2 -value of 0.999 (the improved fit is due to not constraining the curve to the drug release model). The week 2 scan (metal) produced an erroneous datapoint that we excluded as an outlier in our curve fitting. As expected, when adding titanium to the core, QSM does show an increase in susceptibility (Figure 4.9B, metal); unfortunately, the susceptibility changes over time did not fit the expected exponential decay.

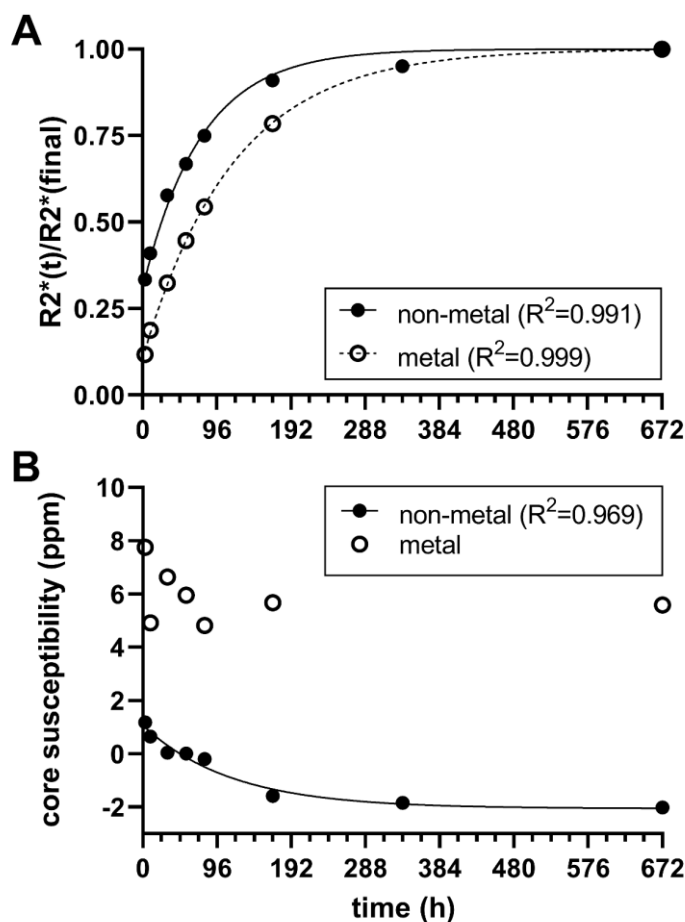


Figure 4.9: Diffusion curves measuring released contrast agent. A) The ratio $R2^*_{avg}(t)/R2^*_{avg}(final)$ is used as a measurement of $concentration(t)/concentration(\infty)$, representing cumulative amounts of contrast agent in the agar. An outlier (metal, 2nd week) was excluded due to poor image quality. The non-metal release curve yields a diffusion constant of $4.59 \times 10^{-11} \text{ m}^2/\text{s}$. B) The susceptibility of the calcium sulfate core measured through QSM. The addition of metal to the calcium sulfate core increased susceptibility as expected, but resulted in poor overall data quality.

4.4 Discussion

In this work we have demonstrated that quantitative MRI is capable of monitoring the diffusion-controlled release of a gadolinium contrast agent. As molecular weight (MW) plays a dominant role in governing small-molecule diffusion, it is ideal if the contrast

agent's MW is similar to the MW of the antibiotics it is intended to simulate. The specific contrast agent employed in this study, Gadovist (MW = 604.7), is reasonably similar to two antibiotics that are often mixed with Stimulan, tobramycin (MW = 467.5) and gentamicin (MW = 477.6), making it an appropriate choice for potential clinical applications.

4.4.1 Calcium Sulfate Core

As expected, the gadolinium that is released from the calcium sulfate core has a signal-enhancing effect, with a high-signal circle increasing in radius over time as the contrast agent slowly diffuses through the agar. The spherical markers were readily identified and exploited to robustly identify the plane of radial symmetry perpendicular to the cylindrical core. A radially symmetric plane is critical to both types of quantitative analysis conducted in this study, radial averaging, and modelling diffusion-controlled release. We have shown that $R2^*$ is sensitive to the small changes in gadolinium concentration and that those changes can be used as a measure of concentration for modelling the system. The released gadolinium also resulted in a decrease in magnetic susceptibility of the central core that is detectable by QSM. The core susceptibility changes from paramagnetic to diamagnetic relative to water, which is consistent with the diamagnetic nature of calcium sulfate. The decay constant found by QSM, while comparable to that found with $R2^*$, was 34% lower; we suspect that in the early time points, the high concentration of gadolinium in the agar directly adjacent to the core decreases the susceptibility difference between the core and agar, resulting in a lower measured core QSM.

Calcium sulfate, in the form of Stimulan, is clinically used as an antibiotic carrier, typically as 6-mm beads implanted in a surgical site. A clinical study that measured drained serum antibiotic concentrations daily for 5 days post-surgery demonstrated a release profile where antibiotic concentration peaked on day 1 and decreased day to day, following a curve with a similar shape to that found in our experiments. A study examining the diffusion of a different small molecule (platinum) using calcium sulfate beads in agar through a series of concentric cubic shells found an overall decrease in

concentration in the innermost shells and an overall increase in concentration in the outermost shells, which is in line with what we see in our $R2^*$ line profiles over time. Using mean $R2^*$ values as a surrogate for the cumulative release of gadolinium in a diffusion-controlled release model demonstrated an excellent fit and provided a diffusion coefficient for the system. Unfortunately, diffusion coefficients are dependent on experimental setup and are thus difficult to compare with published literature; however, a previous study¹⁹ using Iohexol (which has $MW = 821.14$ g/mol compared to Gadovist's $MW = 604.71$ g/mol) in CT using an identical setup (same calcium sulfate carrier, enclosure, and agar recipe) and found a similar diffusion coefficient, reinforcing the reliability of our measurements.

4.4.2 Calcium Sulfate Contained in a Porous Metal Scaffold

Magnetic susceptibility effects become apparent when incorporating the calcium sulfate carrier into a 3D-printed porous metal scaffold. It has been shown that integrating a carrier into a load-bearing scaffold maintains its antibacterial capability and shows promise in early animal experiments,³¹ promising better drug delivery than the current practice of packing the surgery site with antibiotic calcium sulfate beads¹³ by virtue of direct contact with the infection and improved stability over an antibiotic-loaded temporary spacer³⁸ due to the better mechanical properties of the porous metal scaffold. Having found success measuring gadolinium release from a calcium sulfate-only core, we look to explore the possibility of measuring small-molecule release using MRI in the presence of a highly porous metal structure. It is immediately apparent that the signal enhancement effect is still evident surrounding the metal core, even decreasing the volume of signal dropout surrounding the core over time. Unfortunately, the increased magnetic susceptibility makes QSM unreliable, which is likely a product of a core susceptibility outside the range that the algorithm was intended for.³⁷ The increased susceptibility (and resulting field inhomogeneity) also affected $R2^*$ in the volume adjacent to the core; however, there is evidence that $R2^*$ is still sensitive to concentration changes when examining volumes distal to the core. The release curve shows that the addition of a metal scaffold to the core impedes the release of gadolinium, resulting in a slower initial surge and slowed overall release that eventually results in a similar

cumulative concentration. Further work is needed to reliably employ quantitative imaging around calcium sulfate-loaded porous metal scaffolds, but this preliminary work demonstrates both its feasibility and potential value for studying the effects of carrier modifications to drug release using non-invasive measurements.

4.4.3 Limitations

This study is limited to a specific, tightly controlled setup which limits its predictive utility in more realistic applications. While the cylindrical shape of the calcium sulfate core is important for modelling and curve fitting, clinical applications of Stimulan deploy numerous small hemispheric beads; while the smaller beads will decrease susceptibility-related field inhomogeneity, it is difficult to compare our findings using a relatively large cylinder with the various studies experimenting with the hemispheric beads. Furthermore, although we have taken care to choose a contrast agent that is of similar molecular weight to some clinically relevant antibiotics, this study does not attempt to verify that the surrogate molecule acts similarly to antibiotics. Using the quantitative imaging method described in this study, these limitations could be addressed by loading a calcium sulfate bead with both antibiotics and contrast agent, placing the bead in an agar plate as described by Laycock et al.,⁸ and comparing between the zone of inhibition (measuring antibiotic activity) and MRI measurements of gadolinium concentration.

4.4.4 Conclusions

We proposed a method for measuring the release of a gadolinium-based contrast agent loaded into a calcium sulfate carrier using MRI. Results from quantitative imaging show that $R2^*$ and QSM are linearly proportional to gadolinium concentration, agree with previously published studies, and fit a mathematical model of drug release. We also explored the effect of filling a highly porous metal scaffold with the gadolinium-loaded carrier and found that, while further work is needed, quantitative imaging is still viable in spite of the increased core susceptibility. Overall, we have demonstrated the feasibility of MRI as a non-invasive means of characterizing the diffusion-controlled release of small molecules from a clinically relevant carrier through a contrast agent surrogate.

4.5 References

1. Tibbitt MW, Dahlman JE, Langer R. Emerging frontiers in drug delivery. *J Am Chem Soc* 2016;138(3):704-717.
2. Orellana BR, Hilt JZ, Puleo DA. Drug release from calcium sulfate-based composites. *J Biomed Mater Res B Appl Biomater* 2015;103(1):135-142.
3. Narayanaswamy R, Torchilin VP. Hydrogels and their applications in targeted drug delivery. *Molecules* 2019;24(3).
4. Sun Z, Song C, Wang C, Hu Y, Wu J. Hydrogel-based controlled drug delivery for cancer treatment: A review. *Mol Pharm* 2020;17(2):373-391.
5. Mitchell MJ, Billingsley MM, Haley RM, Wechsler ME, Peppas NA, Langer R. Engineering precision nanoparticles for drug delivery. *Nat Rev Drug Discov* 2021;20(2):101-124.
6. Nikezić AVV, Bondžić AM, Vasić VM. Drug delivery systems based on nanoparticles and related nanostructures. *Eur J Pharm Sci* 2020;151:105412.
7. Maale GE, Eager JJ, Mohammadi DK, Calderon FA, 2nd. Elution profiles of synthetic caso(4) hemihydrate beads loaded with vancomycin and tobramycin. *Eur J Drug Metab Pharmacokinet* 2020;45(4):547-555.
8. Laycock PA, Cooper JJ, Howlin RP, Delury C, Aiken S, Stoodley P. In vitro efficacy of antibiotics released from calcium sulfate bone void filler beads. *Materials (Basel)* 2018;11(11).
9. Phillips H, Maxwell EA, Schaeffer DJ, Fan TM. Simulation of spatial diffusion of platinum from carboplatin-impregnated calcium sulfate hemihydrate beads by use of an agarose gelatin tissue phantom. *Am J Vet Res* 2018;79(6):592-599.
10. Thomas MV, Puleo DA. Calcium sulfate: Properties and clinical applications. *J Biomed Mater Res B Appl Biomater* 2009;88(2):597-610.
11. Moore WR, Graves SE, Bain GI. Synthetic bone graft substitutes. *ANZ J Surg* 2001;71(6):354-361.
12. Ene R, Nica M, Ene D, Cursaru A, Cirstoiu C. Review of calcium-sulphate-based ceramics and synthetic bone substitutes used for antibiotic delivery in pji and osteomyelitis treatment. *EFORT Open Rev* 2021;6(5):297-304.
13. Abosala A, Ali M. The use of calcium sulphate beads in periprosthetic joint infection, a systematic review. *J Bone Jt Infect* 2020;5(1):43-49.
14. Lum ZC, Pereira GC. Local bio-absorbable antibiotic delivery in calcium sulfate beads in hip and knee arthroplasty. *J Orthop* 2018;15(2):676-678.

15. Canadian Institute for Health Information. Hip and knee replacements in Canada, 2017–2018: Canadian joint replacement registry annual report. Ottawa, ON: CIHI; 2019.
16. American Academy of Orthopaedic Surgeons. American joint replacement registry annual report 2019. Rosemont, IL: AAOS; 2019.
17. Schwartz AM, Farley KX, Guild GN, Bradbury Jr TL. Projections and epidemiology of revision hip and knee arthroplasty in the United States to 2030. *The Journal of Arthroplasty* 2020.
18. Moore K, Os RW, Dusane DH, Brooks JR, Delury C, Aiken SS, Laycock PA, Sullivan AC, Granger JF, Dipane MV, McPherson EJ, Stoodley P. Elution kinetics from antibiotic-loaded calcium sulfate beads, antibiotic-loaded polymethacrylate spacers, and a powdered antibiotic bolus for surgical site infections in a novel in vitro draining knee model. *Antibiotics (Basel)* 2021;10(3).
19. Khazaei T, Norley CJ, Nikolov H, Pollmann S, Holdsworth D. Micro-CT imaging technique to characterize diffusion of small-molecules: SPIE; 2020.
20. Olsson E, Wirestam R, Lind E. MRI-based quantification of magnetic susceptibility in gel phantoms: Assessment of measurement and calculation accuracy. *Radiol Res Pract* 2018;2018:6709525.
21. Oshima S, Fushimi Y, Okada T, Takakura K, Liu C, Yokota Y, Arakawa Y, Sawamoto N, Miyamoto S, Togashi K. Brain MRI with quantitative susceptibility mapping: Relationship to CT attenuation values. *Radiology* 2020;294(3):600-609.
22. Valencia D, González F. Understanding the linear correlation between diffusion coefficient and molecular weight. A model to estimate diffusion coefficients in acetonitrile solutions. *Electrochemistry Communications - ELECTROCHEM COMMUN* 2011;13:129-132.
23. Prasad M, Dharmatti S, Gokhale S. Magnetic susceptibilities of calcium and strontium ions. *Proceedings of the Indian Academy of Sciences - Section A* 1945;20(5):224-244.
24. Cavelier S, Tanzer M, Barthelat F. Maximizing the strength of calcium sulfate for structural bone grafts. *J Biomed Mater Res A* 2020;108(4):963-971.
25. Allen B, Moore C, Seyler T, Gall K. Modulating antibiotic release from reservoirs in 3D-printed orthopedic devices to treat periprosthetic joint infection. *J Orthop Res* 2020;38(10):2239-2249.
26. Kelly CN, Francovich J, Julmi S, Safranski D, Guldberg RE, Maier HJ, Gall K. Fatigue behavior of as-built selective laser melted titanium scaffolds with sheet-based gyroid microarchitecture for bone tissue engineering. *Acta Biomater* 2019;94:610-626.

27. Zaharin HA, Abdul Rani AM, Azam FI, Ginta TL, Sallih N, Ahmad A, Yunus NA, Zulkifli TZA. Effect of unit cell type and pore size on porosity and mechanical behavior of additively manufactured ti6al4v scaffolds. *Materials (Basel)* 2018;11(12).
28. Cheong VS, Fromme P, Coathup MJ, Mumith A, Blunn GW. Partial bone formation in additive manufactured porous implants reduces predicted stress and danger of fatigue failure. *Ann Biomed Eng* 2020;48(1):502-514.
29. Burastero G, Cavagnaro L, Chiarlone F, Zanirato A, Mosconi L, Felli L, de Lorenzo FDR. Clinical study of outcomes after revision surgery using porous titanium custom-made implants for severe acetabular septic bone defects. *Int Orthop* 2020;44(10):1957-1964.
30. Cai B, Huang L, Wang J, Sun D, Zhu C, Huang Y, Li S, Guo Z, Liu L, Feng G, Li Y, Zhang L. 3D printed multifunctional ti(6)al(4)v-based hybrid scaffold for the management of osteosarcoma. *Bioconjug Chem* 2021;32(10):2184-2194.
31. Qiao S, Wu D, Li Z, Zhu Y, Zhan F, Lai H, Gu Y. The combination of multi-functional ingredients-loaded hydrogels and three-dimensional printed porous titanium alloys for infective bone defect treatment. *J Tissue Eng* 2020;11:2041731420965797.
32. Hong G, Liu J, Cobos SF, Khazaei T, Drangova M, Holdsworth DW. Effective magnetic susceptibility of 3D-printed porous metal scaffolds. *Magnetic Resonance in Medicine*;n/a(n/a).
33. Siepmann J, Siepmann F. Modeling of diffusion controlled drug delivery. *J Control Release* 2012;161(2):351-362.
34. Liu J, Christiansen SD, Drangova M. Single multi-echo gre acquisition with short and long echo spacing for simultaneous quantitative mapping of fat fraction, b0 inhomogeneity, and susceptibility. *Neuroimage* 2018;172:703-717.
35. Christiansen SD, Liu J, Boffa MB, Drangova M. Simultaneous r(2(*)) and quantitative susceptibility mapping measurement enables differentiation of thrombus hematocrit and age: An in vitro study at 3 T. *J Neurointerv Surg* 2019;11(11):1155-1161.
36. Liu J, Drangova M. Method for b0 off-resonance mapping by non-iterative correction of phase-errors (b0-nice). *Magn Reson Med* 2015;74(4):1177-1188.
37. Liu J, Liu T, de Rochefort L, Ledoux J, Khalidov I, Chen W, Tsiouris AJ, Wisnieff C, Spincemaille P, Prince MR, Wang Y. Morphology enabled dipole inversion for quantitative susceptibility mapping using structural consistency between the magnitude image and the susceptibility map. *Neuroimage* 2012;59(3):2560-2568.

38. Charette RS, Melnic CM. Two-stage revision arthroplasty for the treatment of prosthetic joint infection. *Curr Rev Musculoskelet Med* 2018;11(3):332-340.

Chapter 5

5 Conclusions and Future Directions

In the three preceding chapters, I have described the development and demonstration of three separate projects. Each project develops and validates a novel tool and methodology related to orthopedic MRI; the contributions of each project are summarized in 5.1. The summary and conclusions are followed in 5.2 by an outline of the limitations of this work. Potential avenues for future application of these projects concludes this section in 5.3.

5.1 Summary and Conclusions

Chapter 2 pertains to the development of a 3D-printed phantom to visualize and quantitatively analyze geometric distortion in MRI. This is accomplished through the detection and localization of an array of spherical marker beads, through a combination of erosion-based image processing and appropriately customized marker design. The tool demonstrated the ability to characterize inherent image distortion, which could have important applications for routine quality control. The project also evolved to include the ability to encapsulate and embed an object using a modular design, enabling the phantom to characterize susceptibility-induced distortion; this capacity is valuable for understanding and testing artifacts. In particular, the 3D encapsulation of a metal implant in marker beads provides the ability to visualize through-plane distortion and quantify the distortions generated by frequency encoding errors in a 3D acquisition in any plane, an ability that should prove to be a valuable improvement over existing methods. The design of the 3D-printed spherical marker beads – and the scheme to identify and locate them by erosion and centroiding, developed in chapter 2 – also makes important contributions to both chapters 3 and 4; primarily to alleviate the need for ensuring precise physical alignment of phantoms within the scanner.

The main objective of chapter 3 is to demonstrate and quantify the MRI benefits of 3D-printed porous metal implants by determining the impact of porosity on effective

magnetic susceptibility and subsequently artifact size. Although a linear relationship between effective susceptibility and porosity is intuitive, due to the fact that changes to effective magnetic susceptibility (based on internal structure) are not feasible to measure physically, the relationship is difficult to quantify. To prove this relationship, an existing estimation method¹ (relying on comparing scanned and simulated field maps) was implemented in 3D, based on a phantom that provides an array of marker beads to determine 3D phantom orientation relative to B₀. Determination of this orientation is a critical component of generating accurate field map simulations,² and ensures accurate voxel-by-voxel comparisons between simulated and scanned field maps. This capability provided the robustness needed to make accurate estimations of effective susceptibility, based on simulated field maps. This study is highly relevant to orthopedics, as the field is already progressing towards 3D-printed patient-specific porous implants³⁻⁶ and MRI is known to be useful in many musculoskeletal applications, including periprosthetic joint infection.^{7,8}

Chapter 4 describes the development of a potential method for using MRI to non-invasively monitor drug release through the use of a gadolinium contrast agent that acts as a trackable surrogate, small-molecule representative. Quantitative imaging enabled an *in-vitro* demonstration of the ability to measure gadolinium concentrations both inside a carrier (calcium sulfate) and in a surrounding agar sink over the course of 28 days, the results of which were found to fit to an appropriate mathematical model of drug release.⁹ This study relied on findings from both preceding chapters; from chapter 2, the set of three appropriately placed marker beads in the 3D-printed phantom provided a means to consistently identify the plane of radial symmetry of each sample, which was a critical part of the radial averaging process that was used to analyze the gadolinium-enhanced magnitude images and quantitative maps. The mathematical model of diffusion-controlled drug release that was employed for fitting R₂* data to generate a release curve, which also required data from a radially symmetric plane; this would have been much more difficult to achieve robustly with physical alignment of the sample within the scanner. The experiments with porous metal scaffolds filled with gadolinium-loaded calcium sulfate described in chapter 4 were informed and motivated by the findings of chapter 3. Specifically, we found that the highest porosity titanium structure studied in

chapter 3 had a small artifact size and an effective susceptibility that is low enough (similar to the susceptibility shift of an air cavity) to be encountered in routine MRI, suggesting suitability for quantitative imaging. Overall, this work acts as an important proof-of-concept and validation towards the use of gadolinium contrast agents as a means to non-invasively monitor diffusion-controlled drug release, with a particular interest for orthopedics given the common use of the studied carrier material in infection-related revision arthroplasty and the overall potential of 3D-printed porous implants.

5.2 Limitations

5.2.1 Centroid-Based Analysis of Geometric Distortion

A number of limitations were outlined in Chapter 2 pertaining to the distortion phantom, such as tradeoffs between material choices and issues pertaining to the phantom assembly, such as trapped air and high weight. The addition of an embedded hip implant also introduced problems to the analysis, related to unpredictable signal voids. The study design is also relatively limited in scope; only one sequence using one coil was analyzed for distortion. The phantom assembly was also slightly flawed, in that the holder that centered the strut-based phantom caused a small mechanical deformation that, although it confirms that physical relocation of the beads does show up in the analysis, was not intended. The beads were also likely unnecessarily small; applications of the centroid-based analysis in the following chapters found that a larger (7 mm vs 4.5 mm diameter) marker bead is easier to analyze, and the very small field distortion found in the study suggests that self-induced distortion would not be a problem, even with the increased bead size.

The custom insert phantom also has its own limitations, particularly with scope, primarily due to its intent as a proof-of-concept addition to the main study. A more thorough study design would explore multiple 2D scan planes (this study only looked at axial 2D scans) for distortion dependent on slice-select and frequency-encode directions. In general, artifacts' dependence on sequence parameters was not explored in this study; this could be remedied in future work.

5.2.2 Effective Susceptibility of Porous Metal Scaffolds

The methodology outlined in Chapter 3 is highly rigorous, however the study is limited in scope. In particular, the choice of porous structure (the sheet-based gyroid) was motivated by its suitability for future use as an implant, rather than what is typically found in 3D-printing – namely simple, strut-based lattice structures, the inclusion of which would have made for a more general study. However, given that the results of this study are aligned with intuition, concerns over specific internal structures may be alleviated by the literature, in the form of a simpler study looking strictly at artifact volumes of multiple common 3D-printed porous structures.¹⁰

5.2.3 Characterizing Diffusion-Controlled Release with MRI

The limitations of the study described in Chapter 4 are mainly related to clinical applicability of the tightly controlled setup. The samples created for this study (cylindrical carrier core in agar inside a cylindrical container) are highly homogenous and not representative of *in-vivo* environments. In clinical applications, calcium sulfate beads are commonly formed into ~6 mm diameter beads and packed together into a surgical site – it is thus difficult to foresee a means of conducting radial averaging or fitting to a mathematical model. This concern may not be relevant, however, if the beads are amenable to analysis by QSM as the concentration of antibiotic remaining in the carrier is likely to be similarly valuable for monitoring antibiotic release. This study also does not attempt to verify that the selected contrast agent (Gadovist) is an appropriate surrogate molecule; this will need to be addressed in future work.

5.3 Future Work

In this thesis, I have presented tools intended to improve our understanding of MRI around orthopedic implants in the form of direct evaluation of artifacts, ability to image around porous implants, and the use of quantitative imaging in understanding antibiotic delivery in the treatment of periprosthetic joint infection. Future work related to these projects will consist of further exploration of MRI around porous implants and expanding the use of quantitative MRI for monitoring drug release towards clinical relevance.

5.3.1 Quantitative MRI of Antibiotic-Loaded Calcium Sulfate Beads

As discussed briefly in the limitations section of Chapter 4 and in the previous subsection, one major limitation of the study is that there was no attempt to verify the equivalence of drug and contrast-agent release. Having established and validated the necessary quantitative imaging techniques, the next step is to examine its utility using a study design that is more appropriate for measuring antibiotic activity. One candidate design, adapted from Laycock et al.,¹¹ is to load calcium sulfate with both antibiotics and an appropriate contrast agent, form them into beads (as done clinically), and measure the zone of inhibition (Figure 5.1) both visually and with quantitative MRI. This study design is particularly attractive as it would use agar plates, a material which we have already established is suitable for quantitative MRI. The circular geometry also provides a plane of radial symmetry, which will enable the continued use of radial averaging for quantitative assessment of $R2^*$. The bead geometry is also likely to be well-suited to QSM as it is almost spherical, which is compatible with the testing setup used in the development of the morphology enabled dipole inversion algorithm.¹² The comparison between MR images and the clear zone of inhibition may also prove useful for evaluating whether routine magnitude images show signal enhancement proportional to antibiotic activity, despite the non-linear relationship between signal enhancement and concentration. If successful, this study would establish the ability for contrast agents to act as a proxy for antibiotic molecules, addressing a major weakness of Chapter 4 and bringing this technique closer to clinical use.

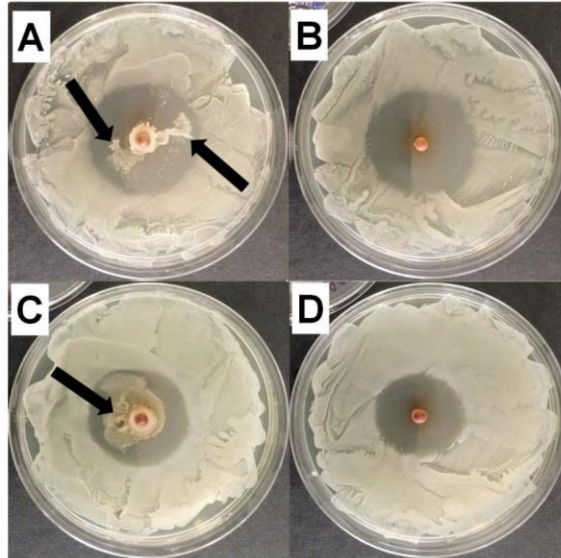


Figure 5.1: Representative image of the Zones of Inhibition (ZOI) observed with (A,B) *S. epidermidis* ATCC 35984 and (C,D) *S. aureus* NCTC 13143 EMRSA-16 at day 20 of rifampicin and vancomycin in combination, showing no evidence of resistant colonies (B,D) and rifampicin alone (A,C) showing potential resistant mutant colonies growing within the ZOI (black arrows). Figure reproduced from Laycock et al.¹¹ under the terms of the Creative Commons Attribution License CC-BY 4.0.

5.3.2 Geometric Distortion Surrounding Porous Titanium Implants

A natural progression for the work of Chapters 2 and 3 is to form the cavity of the custom insert phantom for a porous implant that can be directly compared to a solid implant for susceptibility-induced distortion. This would allow for a more clinically relevant comparison of artifacts surrounding solid and porous implants, by evaluating their differences in routine musculoskeletal MRI sequences, rather than the sequences optimized for field mapping shown in Chapter 3. This comparison study could also address many of the limitations of the demonstration of the custom insert phantom by imaging in multiple planes and varying parameters relevant to metal artifacts, such as readout bandwidth and echo time. The custom insert phantom can also be further customized to include inserts holding fat or other fluids representative of infection near the implant to assess diagnostic ability; these inserts would also be valuable in a number of other applications, such as targeted therapy. If successful, the results of this study

would further promote the ability for porous implants to be imaged with routine MRI, as opposed to dedicated artifact-reduction sequences, adding more impact to the results of Chapter 3 and to the push for porous implants in general.

5.3.3 MR Thermometry of Gyroid-Based Porous Metal Scaffolds

One exciting means of non-invasive eradication of implant biofilms is non-contact inductive heating, both on its own and alongside antibiotics.¹³ The primary concern with inductive heating are detrimental effects to tissue,¹⁴ which is made more problematic due to the difficulty in measuring tissue temperature surrounding an implant. MR thermometry, which has recently been shown to be feasible surrounding a metal implant,¹⁵ may offer a solution to the problem of monitoring implant heating. A number of MR tissue properties (T1, T2, resonance frequency, proton density signal) are linked to thermometry, however only resonance frequency is both linearly proportional and sufficiently sensitive to temperature. Weber et al.¹⁵ showed it is still possible to accurately measure temperature near a solid titanium hip implant through T1 mapping acquired using a dedicated metal artifact reduction sequence, however traditional proton-resonance frequency-shift mapping failed in regions of large off-resonance. The findings of Chapter 3 suggests that the problems preventing the use of proton-resonance frequency-shift thermometry surrounding metal implants may be alleviated sufficiently in the case of porous implants, as the lower effective susceptibility results in substantially less off-resonance volume. Although challenging, it is likely possible to create a MR-compatible induction heater for implants as well, given their similarity to the coils used in image acquisition. Successfully demonstrating the ability to monitor tissue temperature would make implant heating much more feasible, which in turn helps address any long-term infections upon completion of antibiotic delivery.

5.4 References

1. Perkins SL, Daniel BL, Hargreaves BA. Mr imaging of magnetic ink patterns via off-resonance sensitivity. *Magn Reson Med* 2018;80(5):2017-2023.
2. Bouwman JG, Bakker CJ. Alias subtraction more efficient than conventional zero-padding in the fourier-based calculation of the susceptibility induced perturbation of the magnetic field in MR. *Magn Reson Med* 2012;68(2):621-630.
3. Arabnejad S, Johnston B, Tanzer M, Pasini D. Fully porous 3D printed titanium femoral stem to reduce stress-shielding following total hip arthroplasty. *J Orthop Res* 2017;35(8):1774-1783.
4. Burastero G, Cavagnaro L, Chiarlone F, Zanirato A, Mosconi L, Felli L, de Lorenzo FDR. Clinical study of outcomes after revision surgery using porous titanium custom-made implants for severe acetabular septic bone defects. *Int Orthop* 2020;44(10):1957-1964.
5. Castagnini F, Caternicchia F, Biondi F, Masetti C, Faldini C, Traina F. Off-the-shelf 3D printed titanium cups in primary total hip arthroplasty. *World J Orthop* 2021;12(6):376-385.
6. Krafft P, Osburn B, Vivas A, Rao G, Alikhani P. Novel titanium cages for minimally invasive lateral lumbar interbody fusion: First assessment of subsidence. *Spine Surg Relat Res* 2020;4(2):171-177.
7. Alaia EF, Chhabra A, Simpfendorfer CS, Cohen M, Mintz DN, Vossen JA, Zoga AC, Fritz J, Spritzer CE, Armstrong DG, Morrison WB. MRI nomenclature for musculoskeletal infection. *Skeletal Radiol* 2021;50(12):2319-2347.
8. Galley J, Sutter R, Stern C, Filli L, Rahm S, Pfirrmann CWA. Diagnosis of periprosthetic hip joint infection using MRI with metal artifact reduction at 1.5 T. *Radiology* 2020;296(1):98-108.
9. Siepmann J, Siepmann F. Modeling of diffusion controlled drug delivery. *J Control Release* 2012;161(2):351-362.
10. Carter LN, Addison O, Naji N, Seres P, Wilman AH, Shepherd DET, Grover L, Cox S. Reducing MRI susceptibility artefacts in implants using additively manufactured porous ti-6al-4v structures. *Acta Biomater* 2020.
11. Laycock PA, Cooper JJ, Howlin RP, Delury C, Aiken S, Stoodley P. In vitro efficacy of antibiotics released from calcium sulfate bone void filler beads. *Materials (Basel)* 2018;11(11).
12. Liu J, Liu T, de Rochefort L, Ledoux J, Khalidov I, Chen W, Tsiouris AJ, Wisnieff C, Spincemaille P, Prince MR, Wang Y. Morphology enabled dipole inversion for quantitative susceptibility mapping using structural consistency

between the magnitude image and the susceptibility map. *Neuroimage* 2012;59(3):2560-2568.

13. Pijls BG, Sanders I, Kujiper EJ, Nelissen R. Induction heating for eradicating staphylococcus epidermidis from biofilm. *Bone Joint Res* 2020;9(4):192-199.
14. Verheul M, Drijfhout JW, Pijls BG, Nibbering PH. Non-contact induction heating and saap-148 eliminate persisters within mrsa biofilms mimicking a metal implant infection. *Eur Cell Mater* 2021;43:34-42.
15. Weber H, Taviani V, Yoon D, Ghanouni P, Pauly KB, Hargreaves BA. Mr thermometry near metallic devices using multispectral imaging. *Magn Reson Med* 2017;77(3):1162-1169.

Appendices: Permissions and Policies Regarding Copyrighted Content

Appendix A: Creative Commons license CC BY 4.0

(<https://creativecommons.org/licenses/by/4.0/>)



Attribution 4.0 International (CC BY 4.0)

This is a human-readable summary of (and not a substitute for) the [license](#). [Disclaimer](#).

You are free to:

Share — copy and redistribute the material in any medium or format

Adapt — remix, transform, and build upon the material for any purpose, even commercially.

The licensor cannot revoke these freedoms as long as you follow the license terms.



Under the following terms:



Attribution — You must give [appropriate credit](#), provide a link to the license, and [indicate if changes were made](#). You may do so in any reasonable manner, but not in any way that suggests the licensor endorses you or your use.

No additional restrictions — You may not apply legal terms or [technological measures](#) that legally restrict others from doing anything the license permits.

Appendix B: Creative Commons licensing statements



[Cureus](#). 2022 Jan; 14(1): e20968.

PMCID: PMC8815820

Published online 2022 Jan 5. doi: [10.7759/cureus.20968](https://doi.org/10.7759/cureus.20968)

PMID: [35154947](https://pubmed.ncbi.nlm.nih.gov/35154947/)

Current Concepts on the Application, Pharmacokinetics and Complications of Antibiotic-Loaded Cement Spacers in the Treatment of Prosthetic Joint Infections

Monitoring Editor: Alexander Muacevic and John R Adler

[Panagiotis V Samelis](#),^{✉1} [Eftychios Papagrigrakis](#),² [Eleni Sameli](#),³ [Andreas Mavrogenis](#),⁴ [Olga Savvidou](#),⁵ and [Panagiotis Koulouvaris](#)⁶

[▶ Author information](#) [▶ Article notes](#) [▼ Copyright and License information](#) [Disclaimer](#)

[Copyright](#) © 2022, Samelis et al.

This is an open access article distributed under the terms of the Creative Commons Attribution License, which permits unrestricted use, distribution, and reproduction in any medium, provided the original author and source are credited.



[Molecules](#). 2021 Jul; 26(13): 4066.

PMCID: PMC8272161

Published online 2021 Jul 2. doi: [10.3390/molecules26134066](https://doi.org/10.3390/molecules26134066)

PMID: [34279405](https://pubmed.ncbi.nlm.nih.gov/34279405/)

3D-Printing of Drug-Eluting Implants: An Overview of the Current Developments Described in the Literature

[Vanessa Domsta](#) and [Anne Seidlitz](#)*

Markus Thommes, Academic Editor and Julian Quodbach, Academic Editor

▶ [Author information](#) ▶ [Article notes](#) ▶ [Copyright and License information](#) ▶ [Disclaimer](#)

[Copyright](#) © 2021 by the authors.

Licensee MDPI, Basel, Switzerland. This article is an open access article distributed under the terms and conditions of the Creative Commons Attribution (CC BY) license (<https://creativecommons.org/licenses/by/4.0/>).



[Materials \(Basel\)](#). 2018 Nov; 11(11): 2265.

PMCID: PMC6266743

Published online 2018 Nov 13. doi: [10.3390/ma11112265](https://doi.org/10.3390/ma11112265)

PMID: [30428581](https://pubmed.ncbi.nlm.nih.gov/30428581/)

In Vitro Efficacy of Antibiotics Released from Calcium Sulfate Bone Void Filler Beads

[Phillip A. Laycock](#),¹ [John J. Cooper](#),¹ [Robert P. Howlin](#),² [Craig Delury](#),¹ [Sean Aiken](#),¹ and [Paul Stoodley](#)^{3,4,*}

▶ [Author information](#) ▶ [Article notes](#) ▶ [Copyright and License information](#) ▶ [Disclaimer](#)

[Copyright](#) © 2018 by the authors.

Licensee MDPI, Basel, Switzerland. This article is an open access article distributed under the terms and conditions of the Creative Commons Attribution (CC BY) license (<http://creativecommons.org/licenses/by/4.0/>).

Appendix C: Wiley policy regarding permission to use own work as part of dissertation

WILEY

THE WILEY NETWORK | INSTRUCTORS & STUDENTS | JOURNAL EDITORS | LIBRARIANS | PROFESSIONALS | **RESEARCHERS** | SOCIETY LEADERS

TOPICS ▾ CONTENT TYPE ▾

Search Researchers



Reusing Wiley content

If you're reusing Wiley content in your thesis or dissertation, rights will be granted at no cost to you if the content meets these requirements:

- **Your thesis or dissertation is not being used for commercial purposes.** This means that you're submitting it only for graduation requirements. You don't currently have a deal with a commercial publisher, and you won't otherwise be benefitting financially from the publication of your thesis.
- **Wiley is the rights holder of the content you are seeking to reuse.** Usually, Wiley holds the rights to our content, but occasionally the rights holder will be an author or sponsoring organization. In those cases, Wiley cannot guarantee free reuse.

While Wiley does grant free reuse of content in thesis and dissertation projects, we do still require a record of use so that we can issue you a license agreement.

If you publish your thesis or dissertation through a commercial publisher in the future, you will need to reapply for commercial reuse licenses. The legal rights granted for content reuse in non-commercial publications, such as a thesis or dissertation, are different from the rights required by commercial publishers to legally republish third-party content.

Do I need to request permission to use my own work as my dissertation?

If you are the author of a published Wiley article, you have the right to reuse the full text of your published article as part of your thesis or dissertation. In this situation, you do not need to request permission from Wiley for this use.

If your institution still requires a reuse license in this case, follow the steps below to request your license via RightsLink.

Curriculum Vitae

Greg Hong

UNIVERSITY EDUCATION:

- PhD 2015-2022
 Department of Medical Biophysics
 University of Western Ontario
 Thesis: “Quantitative MRI and 3D-Printing for Monitoring
 Periprosthetic Joint Infection”
 Supervisors: Dr. David W. Holdsworth & Dr. Maria Drangova
 (Medical Biophysics)
- B. Eng 2009-2015
 Department of Electrical & Computer Engineering
 McMaster University
 Concentration: Electrical & Biomedical Engineering

PROFESSIONAL EXPERIENCE:

- 09/2012 - Strategic Corporate Services Intern,
 08/2013 Ontario Financing Authority

SCHOLARSHIPS AND AWARDS:

- 2022 ISMRM Educational Stipend
- 2017 ISMRM Educational Stipend
- 09/2015 - CMHR Transdisciplinary Bone and Joint Training Award
 08/2020
- 09/2015 - Western Graduate Research Scholarship
 08/2020

PUBLICATIONS:

1. **G. Hong**, J. Liu, S.F. Cobos, T. Khazaei, M. Drangova, and D.W. Holdsworth. “Effective Magnetic Susceptibility of 3D-Printed Porous Metal Scaffolds” *Magnetic Resonance in Medicine*, 2022 Jun;87(6):2947-2956. DOI: 10.1002/mrm.29136

In Preparation

2. **G. Hong**, M.G. Teeter, J.S. Milner, S.I. Pollmann, M. Drangova, and D.W. Holdsworth. “Design, Fabrication, Validation and Automated Analysis of a Novel 3D-Printed MRI Distortion Phantom.” In preparation for submission to *Physics in Medicine and Biology*

3. **G. Hong**, T. Khazaei, J. Liu, S.D. Christiansen, S.F. Cobos, M. Drangova, and D.W. Holdsworth. “Characterizing Diffusion-Controlled Release of Small-Molecules Using Quantitative MRI: Application to Orthopedic Infection” In preparation for submission to *Scientific Reports*

Abstracts

1. **G. Hong**, T. Khazaei, S.F. Cobos, S.D. Christiansen, J. Liu, M. Drangova, and D.W. Holdsworth. “Quantitative MRI to characterize diffusion-controlled release of gadolinium from a calcium sulphate matrix” International Society for Magnetic Resonance in Medicine, London, UK (May 2022) Digital Poster Presentation
2. **G. Hong**, S. Cobos, T. Khazaei, J. Liu, M. Drangova, and D.W. Holdsworth. “MRI Artifact Reduction Near 3D-Printed Porous Metal Scaffolds” Canadian Bone and Joint Conference, London, Ontario (Held virtually June 2020); Oral Presentation
3. **G. Hong**, S. Cobos, T. Khazaei, J. Liu, M. Drangova, and D.W. Holdsworth. “MRI characterization of a novel porous 3D printed metal scaffold” Imaging Network of Ontario, Toronto, Ontario (Held virtually March 2020); Oral Presentation
4. **G. Hong**, J. Liu, D.W. Holdsworth, and M. Drangova. “Validation of simulated vs. experimentally acquired B0 field maps surrounding metal” Imaging Network of Ontario, London, Ontario (March 2019); Oral Presentation
5. **G. Hong**, J. Liu, D.W. Holdsworth, and M. Drangova. “Experimental Validation of Field Map Simulations Near Metal” Canadian Bone and Joint Conference, London, Ontario (May 2018); Poster Presentation
6. **G. Hong**, M.G. Teeter, J.S. Milner, S.I. Pollmann, M. Drangova, and D.W. Holdsworth. “Characterization of Through-Plane and In-Plane Artifacts using a 3D-Printed Grid Phantom with an Embedded Metal Hip Implant”, International Society for Magnetic Resonance in Medicine, Honolulu, HI. USA, Apr 2017 (One of 9 invited posters for the Musculoskeletal MR study group session)
7. **G. Hong**, M.G. Teeter, J.S. Milner, S.I. Pollmann, M. Drangova, and D.W. Holdsworth. “Characterization of Metal Artifacts using a 3D-Printed Grid Phantom with an Embedded Hip Implant”, Imaging Network of Ontario, London, Ontario (March 2017); Poster Presentation
8. **G. Hong**, M.G. Teeter, J.S. Milner, S.I. Pollmann, M. Drangova, and D.W. Holdsworth. “Geometric Distortion Phantom for MRI”, Canadian Bone and Joint Conference, London, Ontario (Apr 2016); Poster Presentation
9. **G. Hong**, M.G. Teeter, J.S. Milner, S.I. Pollmann, M. Drangova, and D.W. Holdsworth. “Geometric Calibration Phantom for MRI and CT”, Imaging Network of Ontario, Toronto, Ontario (March 2016); Poster Presentation